SYNTHESIS OF COLLOIDAL INORGANIC NANOMATERIALS AND THEIR INTERACTIONS WITH SOFT MATTER

BY

JACOB TURNER

DISSERTATION

Submitted in partial fulfillment of the requirements
for the degree of Doctor of Philosophy in Chemistry
in the Graduate College of the
University of Illinois Urbana-Champaign, 2021

Urbana, Illinois

Doctoral Committee:

Professor Catherine J. Murphy, Chair
Associate Professor Cecilia Leal
Professor Yi Lu
Associate Professor Joshua Vura-Weis

ABSTRACT

Nanomaterials have garnered a lot of attention the last several decades due to the unique material properties observed on the nanoscale (1-100 nm). In particular, colloidal nanoparticles have been a main focus of the research community due to their large surface areas and resulting high surface energies. This leads to nanoparticles having very different optical properties, electrical properties, and reactivities compared to their bulk counterparts. These properties are largely influenced by the chemical composition, shape, and size of the colloidal nanoparticles.

Nanoparticles are often combined with other materials for specific applications to make use of their unique nanoscale properties. Therefore, furthering the understanding of how these nanoparticles interact with other forms of matter is necessary for the continued development of nanotechnology. This dissertation focuses on a few types of colloidal inorganic nanoparticles and how they interact with soft materials. The inorganic nanoparticles of focus are gold nanorods (AuNRs), metal-organic framework (MOF) nanoparticles (nanoMOF), and the core-shell combination of the two (AuNR@MOF). This work demonstrates how these inorganic nanoparticles interact with two important forms of soft matter, polymer composites and biomolecules.

In Chapter 1, colloidal inorganic nanoparticles are explained in detail with a focus on AuNRs and nanoMOFs. The plasmonic properties and applications of AuNRs are outlined, along with the synthesis and surface engineering of AuNRs. The unique properties of MOFs and their applications is discussed with an emphasis on what makes them advantageous over other porous nanomaterials. Chapter 1 will also introduce the basic concepts regarding these nanoparticle interactions with soft matter. This portion will highlight the nano-bio interface and explain the

importance of the protein corona. In addition to biological soft matter, polymer nanocomposites will be explained with attention on hydrogel-nanoparticle composites.

A layer-by-layer method developed for growing a MOF around a AuNR is discussed in Chapter 2. MOFs lend themselves to a layer-by-layer growth method due to their distinctive building block nature. Using the layer-by-layer method, a HKUST-1 shell was grown on the AuNR surface with a sub-nanometer level control over the shell thickness. Interestingly, the surface charge is also easily controlled by the terminal layer either being the metal nodes (positive charge) or the organic linker (negative charge). It was also found that with the proper surface modification of the AuNRs, a very conformal MOF shell could be grown. These materials with highly porous shells around AuNRs have promise in areas such as sensing and catalysis.

Chapter 3 examines the synthesis of MOF shells around AuNRs using reported one-pot methods as opposed to the developed layer-by-layer method. These one-pot synthetic methods produce much larger shells and they are not as conformal. However, these methods allow for a larger quantity of material to be produced in a much timelier manner. The MOF shell produced was made of ZIF-8, which is one of the more aqueous stable MOFs, a necessity to probe the interactions with biomolecules. The synthesis of nanoMOFs is also discussed in Chapter 3. The characterization of AuNR@ZIF-8 and nanoZIF-8 particles is shown and the properties of these two materials are compared.

Chapter 4 advances on the work in Chapter 3 and discusses how the synthesized porous nanoparticles interact with different proteins. Three proteins with very different sizes and isoelectric points were studied. It was determined that the AuNR@ZIF-8 particles had a higher amount of protein adsorption per unit surface area compared to nanoZIF-8. The thermodynamics of this adsorption process was also determined using isothermal titration calorimetry. Furthermore,

the orientation of the proteins at the surface was evaluated and it was determined that certain proteins had a preferred orientation. This work shows the potential for porous nanoparticles to be used to create engineered protein coronas.

In Chapter 5 the focus shifts away from nanoparticle interactions with biological soft matter and towards polymer composites. AuNRs of varying surface chemistries were successfully dispersed into the pre-gel mixture of a tough and stretchable hydrogel. The hydrogel formed with the AuNRs present and maintained its phenomenal mechanical properties. The ability of the stretchable hydrogel to control AuNR orientation by reversibly aligning the AuNRs was also demonstrated. This work outlines the fundamentals of nanoparticles dispersed into multi-polymer systems, and the capability of using a biocompatible hydrogel to control AuNR alignment.

ACKNOWLEDGMENTS

First and foremost, I would like to thank my family and friends that have supported me throughout graduate school. To my Mom and Dad, thank you for being the best parents imaginable. You instilled the importance of education at a young age, and have supported me throughout my entire education journey. Whether it was driving down on short notice to help me move apartments or the regular phone calls, your support and encouragement has been immensely appreciated. Thank you to my siblings, Zach and Isabella, for making weekend trips down to Champaign to spend time with me, it meant a great deal to me each time you came to visit. Thank you again to Mom, Dad, Zach, and Isabella, I love all of you and I would not have been able achieve my education goals without you. To my fiancée, Audrey, I love you very much and I cannot thank you enough for sticking by my side throughout our time pursuing graduate studies in different states. I know it wasn't always easy and the long road trips were pain, but I am grateful to have someone as special as you to share these experiences with. I can't wait to start our lives together and get married next year!

To all my friends and family back home in Michigan, I appreciate your support of my studies and understanding for when I would miss important events. Everyone still sent me invites and kept in touch with me which has meant a lot throughout my time in graduate school. I look forward to moving back to Michigan to start my career and seeing everyone on a regular basis again.

I also owe a special thank you to my advisor, Professor Catherine Murphy. Working with you and learning from you has been a privilege of mine. Your work ethic, leadership, and passion for science in admirable; you are inspiration to all young scientists, myself included. The care,

support, and encouragement you show for your students is outstanding. It has been an honor to be in group and get to see first-hand your well-deserved recognition. During your ACS Inorganic Award address, you mentioned that you always appreciated Professor Barton for making you feel better about your research after speaking with her. I think I can speak on behalf of all your students and say, you have emulated this trait very well. You really know how to encourage students, knowing I had your support and confidence made coming into lab each day an enjoyable experience.

Thank you to my thesis committee, Professor Cecilia Leal, Professor Josh Vura-Weis, and Professor Yi Lu. You all made my prelim an excellent learning experience, and I have a great deal of respect for each one of you. Much of the feedback I received during my prelim was to always remember the big picture and work towards it. This has been valuable advice throughout my senior graduate student years that has really helped me find my niche within the scientific community.

To all of the great people I have encountered in the Murphy Group and within the department, thank you, it has been a pleasure getting to know each one of you. Thank you to Josh Hinman, who was an instrumental mentor during the beginning portion of my graduate career. Thank you also to the undergraduate students Jun Og and Namya Sarvaiya that worked alongside me and helped advance our research. To everyone I have worked with in the Murphy Group, past and present, thank you for the scientific discussions and the friendship we have created. To the other students in the department that I got to see regularly throughout my time on JST and SWC, thank you all and I hope you all continue to strive to make our department better for everyone.

I am very appreciative of everything the people in the Department and Area offices do for us students. Thank you to the IMP office staff, Chemistry department staff, SCS safety, SCS storeroom, and the SCS Career Services staff. You all do/have done so much for our department

and students, it is greatly appreciated. The Department and Area offices do a phenomenal job of keeping everything running smoothly, and allowing us students to really focus on our research.

There have been many people from many different facilities that have helped me throughout my research. Thank you to MRL and their staff members, with a special thank you to Wacek Sweich and Lou Ann Miller. Thank you also to the SCS Microanalysis staff and Protein Sciences staff. Whether it was training me on instruments, running samples, or helping analyze results, your patience and willingness to help was appreciated.

Lastly, I would like to acknowledge all of the scientists that encouraged me through my days at Saginaw Valley State University and Dow Chemical. Thank you to my undergraduate research advisor, Professor Adam Warhausen. At a smaller university without graduate students, you were the one that taught me many basic laboratory techniques. To my Dow Chemical colleagues, thank you, my time working with all of you really pushed me to pursue graduate school. I owe a special thanks to my former colleague Kevin Howard, who has become a great mentor of mine. Your continued advice and support have been very helpful throughout my educational and career development.

I have created many memories in Champaign-Urbana and graduate school has truly been an excellent experience. There are a number of restaurants and bars around town that I know my fiancée and I will really miss. Whenever family and/or friends came to visit, we always had fun, found new places to go to, and new things to try. I'll say one last thank you to everyone that helped make graduate school such a great experience!

TABLE OF CONTENTS

CHAPTER 1: AN INTRODUCTION TO INORGANIC NANOPARTICLES

1.1 Abstract

Inorganic nanoparticles have been used for centuries due to their unique optical properties. This is evidenced by the Lycurgus Cup, a Roman artifact containing small amount of gold nanoparticles. Today, there are synthetic methods that provide precise shape and size control of many different types of inorganic nanoparticles. Plasmonic nanoparticles, such as gold, are of great interest to the scientific community due to their useful optical properties and versatile surface chemistries. One of the interesting surfaces of gold nanoparticles are porous shells, which can be used to sequester other molecules. While colloidal inorganic nanoparticles display brilliant properties, for more applied technologies it is necessary to incorporate them with other types of materials. Understanding how nanoparticles interact with other forms of matter will help further the applications of inorganic nanoparticles.

Having control and predictability over the interactions at nanoparticle surfaces will allow for the better design of nanomaterials. For example, nanoparticles used as therapeutics or imaging agents are exposed to biomolecules that coat the surface of the nanoparticles. This changes the identity of the nanoparticle and impacts their targeting efficiency, cellular uptake, and toxicity of the nanoparticles. It also common for nanoparticles to be used in the creation of nanocomposites, where they are incorporated into polymer films, gels, or other matrices. As the matrix becomes more complex it can be difficult to avoid nanoparticle aggregation. With proper surface engineering it may possible to control and predict the interactions of nanoparticles with other forms of soft matter, such as biomolecules and polymers.

1.2 Colloidal Inorganic Nanoparticles

Inorganic nanoparticles are composed of metals or in the form of chalcogenides, oxides, hydroxides, or phosphates.[1–4] These nanocrystals, referred to at the time as "finely divided metals", have been used for centuries in decorative arts because of their optical properties.[5,6] It wasn't until the 20th century with advance characterization techniques, like electron microscopy, and colloidal syntheses like the Turkevich method, that scientists really began to understand and explore the area of nanoscience.[3,7,8] Today, inorganic nanoparticles represent a diverse set of materials. They can be porous such as silica nanoparticles, have exceptional optical and electronic properties such as gold nanoparticles and quantum dots, or exhibit superparamagnetism like iron oxide nanoparticles, among a variety of other interesting nanoparticle types and properties.[3,9–14] With this diverse set of materials, inorganic nanoparticles have become prevalent in applications such as electronics, sensors, catalysis and photonics.[3,15–19]

Part of what makes inorganic nanoparticles so fascinating is that they can be treated similar to that of molecules, despite having very different properties. Nanoparticles can be synthesized in solution by chemical reactions much like molecules.[4,9,20] They have a propensity to interact with other molecules, and can even be assembled into larger structures.[21,22] So, while they can behave like molecules in certain ways, they have many distinct differences in terms of their properties. One distinct difference is that nanoparticles can have much more intense optical properties than molecular absorbers.[3,5,6,17] Nanoparticles have a very high concentration of surface atoms compared to their volume, which leads to them having high surface energies. This is part of what gives them different properties from that of their bulk material. Also, nanoparticle surfaces can be functionalized with different molecules such as polymers, or small organic molecules.[18,23,24] Being able to modify the nanoparticle surface, while keeping the optical/electronic properties of the core

largely unchanged is a major part in what has allowed nanoparticles to advance technology forward.[3,18,24]

A large part of what has led to the increase of inorganic nanoparticles in modern technology has been the development of quality synthetic methods. There are now libraries of both bottom-up and top-down synthetic methods that provide exceptional shape and size control.[20,21,25] Inorganic nanoparticles can be synthesized as spheres, rods, prisms, cubes, and more extravagant shapes like stars and diamonds, with each of these shapes serving purposes as they can possess very different properties.[9] Interestingly, while there are many synthetic methods, the actual growth mechanism for many nanoparticles is still not completely understood. The thermodynamics and kinetics for many of these growth processes are still an ongoing debate within the scientific community.[3,26–28]

While inorganic nanoparticles and nanotechnology has rapidly advanced the last few decades, there are still some challenges that face the field today. One large issue is that the commercialization of nanoparticles is difficult because typically nanoparticles are only produced in milligram quantities.[10] Many of the syntheses also generate a lot of waste. Another one of the significant challenges facing nanoparticles is there is still a lot to learn regarding the biological fate of these materials.[29–32] More *in vivo* research is needed to determine the potential hazards associated with inorganic nanoparticles.[33,34] Also, developing a better understanding of the biodistribution of nanoparticles within environments is necessary for the safe and practical use of nanoparticles.[35]

1.3 Gold Nanoparticles

Of the category of colloidal inorganic nanoparticles, perhaps the type that has been studied the most is gold nanoparticles. In fact, gold nanoparticles can be dated as far back as the ancient

Roman artifact known as the Lycurgus Cup.[8] Throughout history very small amounts of gold nanoparticles were used for stained glass windows and other forms of art, due to their intense ruby red color.[8] The origin of those intense colors was first explored by Michael Faraday, who determined it was due to finely divided particles of gold.[3,8] Today, the fundamental properties of those intense colors are understood and gold nanoparticles can be synthesized in a variety of shapes and sizes.[6,20]

1.3.1 Optical Properties and Applications

Gold and silver nanoparticles exhibit fascinating size and shape dependent optical properties.[5,6] This phenomenon observed for these nanoscale inorganic solids is known as a plasmon. As inorganic nanoparticles become similar in size to the mean free path of electrons in that metal, they begin to support a localized surface plasmon resonance (LSPR).[6,36] Where upon illumination, this plasmon is the oscillation of the conduction band electrons at the metal surface. Interestingly, these plasmonic properties are shape dependent. Typical gold nanoparticles that are spherical in shape (AuNS) will exhibit one plasmon band around 520 nm. However, when the nanoparticle is elongated into a rod-shaped particle there are two plasmon bands that are observed. The two plasmon bands that are observed correspond to the transverse axis and the longitudinal axis of the gold nanorod (AuNR), illustrated in Figure 1.1. The longitudinal plasmon resonance is dependent upon the aspect ratio of the AuNR, and by varying this aspect ratio the AuNR longitudinal plasmon can be tuned from the visible to near-infrared (NIR) portions of the electromagnetic spectrum.[36–38] This tunability of the longitudinal plasmon is shown in Figure 1.2, as the aspect ratio increases the longitudinal plasmon red shifts. The extinction spectra that is

shown in Figure 1.2 is the sum of the absorption and elastic light scattering of the AuNRs. Also shown in Figure 1.2, are the vibrant colors exhibited by AuNRs of different aspect ratios.

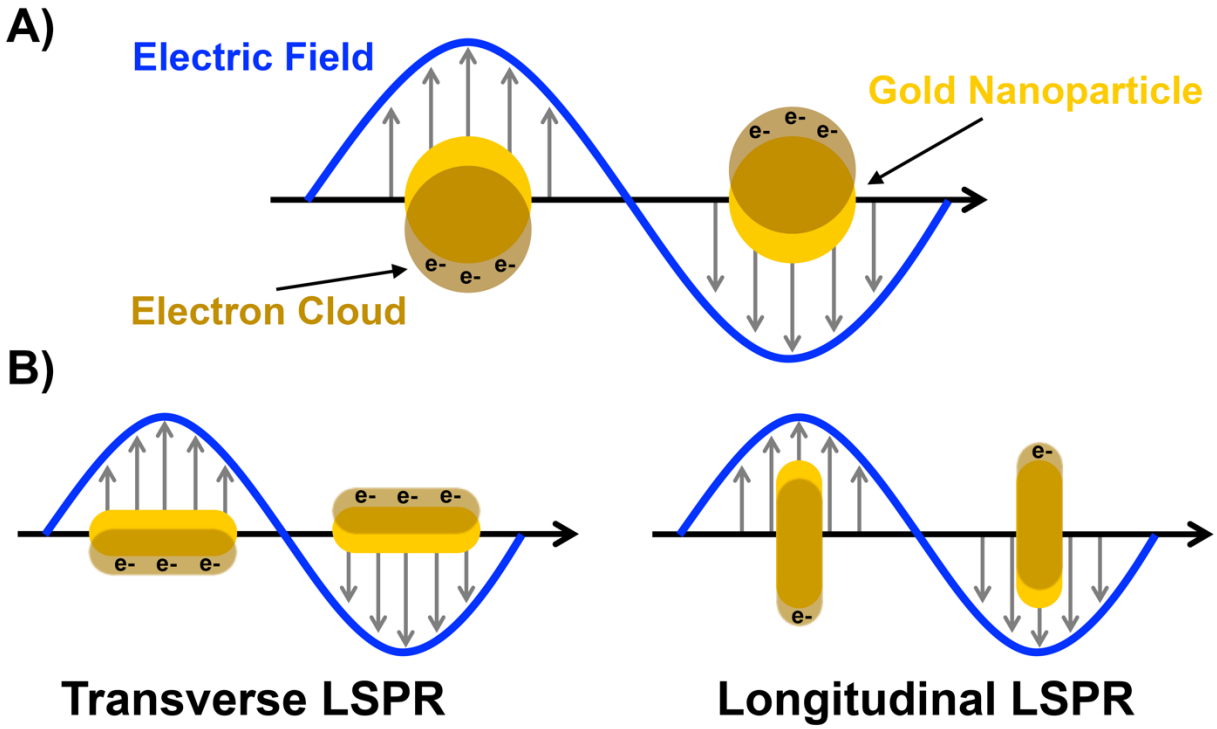

Figure 1.1: Representation of the localized surface plasmon resonance(s) that are observed for a (A) gold nanosphere and (B) gold nanorod. For an anisotropic nanoparticle shape, such as a rod, two plasmons are observed corresponding to each axis of the nanorod.

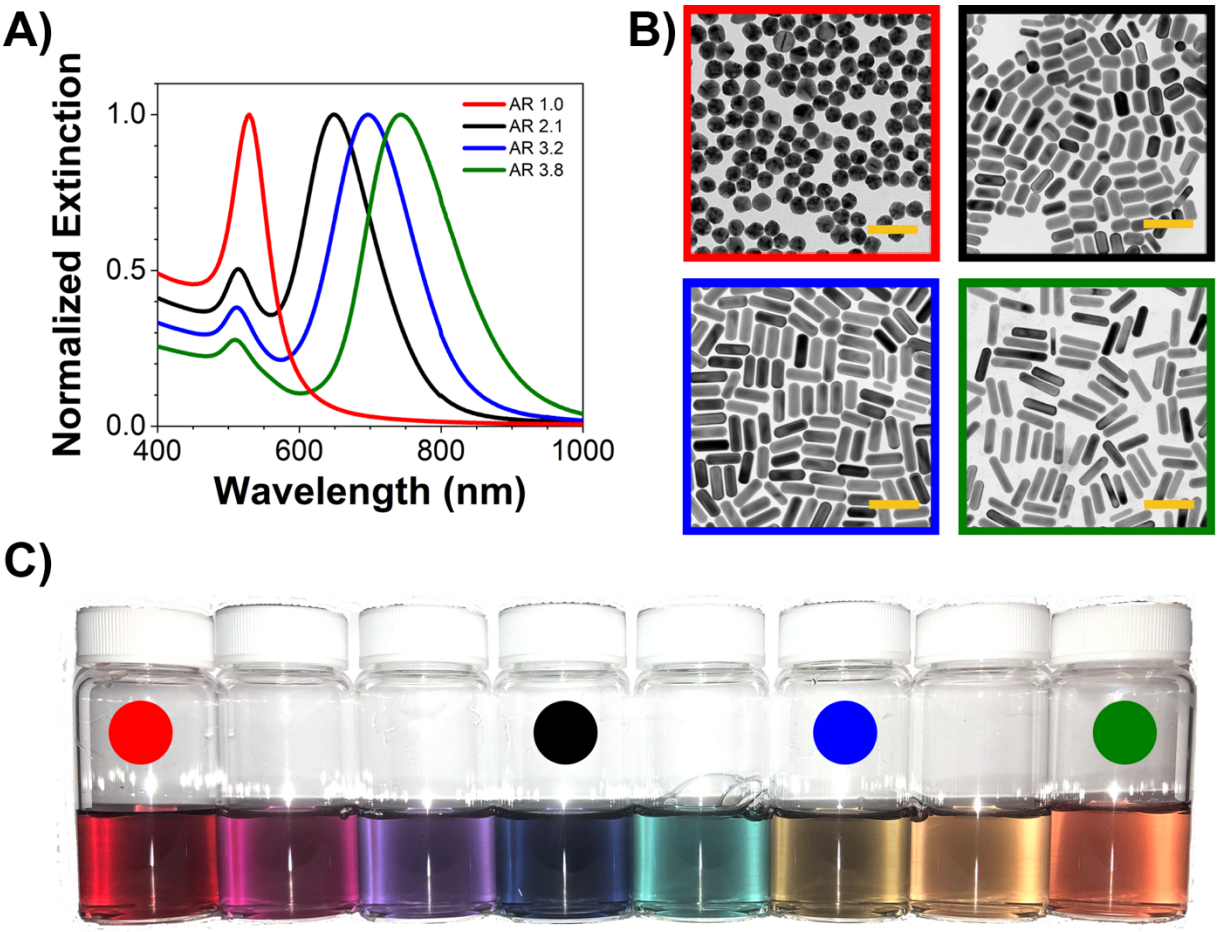

Figure 1.2: (A) UV-vis extinction spectra with corresponding (B) TEM images for different aspect ratios of gold nanorods. (Red = AR 1.0, Black = AR 2.1, Blue = AR 3.2, Green = AR 3.8). The scale bars on the TEM images are all 100 nm. (C) Photograph of colloidal AuNP and AuNRs with varying aspect ratios.

Plasmons actually provide more capabilities than just the vibrant colors. Upon resonant illumination of the plasmon, the AuNRs also produces local electric fields as well as heat.[3,6] The local electric fields that are produced give rise to surface enhanced spectroscopies. The most well-known of the surface enhanced spectroscopies is surface enhanced Raman scattering (SERS). Molecules in close contact with the AuNR can have their Raman signal increased as much as 10^{10},

leading to better diagnostics.[39] As mentioned, the plasmon can also produce heat when illuminated. The heat is dissipated to the AuNR surroundings from the gold lattice through phonon-phonon interactions.[29] This plasmonic heating produces enough local heat to kill cells, thus much research has gone into photothermal therapies where light can be converted to heat to kill cancer cells.[40,41]

These properties of AuNRs have led to a number of interesting applications including therapeutics, imaging agents, sensing, and catalysis. Xu *et al.* demonstrated the use of functionalized AuNRs for the synergetic photothermal and chemotherapy of breast cancer.[42] Chen *et al.* determined that miniature AuNRs could be used for the photoacoustic imaging of the second near-infrared window; an area that prior contrast agents gave unreliable results.[43] Fu *et al*. used AuNRs and SERS to detect a pesticide commonly found in fruits.[44] Su *et al*. demonstrated the catalytic applications using AuNRs functionalized with palladium dendrites on the ends of the AuNRs.[45] These are a few recent highlights of the many applications of AuNRs, illustrating the wide ranging capabilities of these plasmonic nanoparticles.

1.3.2 Synthesis and Surface Engineering

In general, the synthesis of AuNPs involves the reduction of a gold salt and the incorporation of a surface stabilizing agent. One of the more widely used methods still used today is the Turkevich method, originally reported in 1951.[7] In this approach, $HAuCl_4$ is boiled, and then sodium citrate is added, which acts as both the reducing and stabilizing agent. The Turkevich method produces AuNSs that are about 20 nm in size. More recently, the Turkevich method was expanded on by Chan *et al.* to synthesize larger AuNPs.[46] With this method, they use the AuNSs produced by the Turkevich method as seeds to grow larger AuNSs, and are able to produce quality AuNSs from 50-200 nm in size. The other common method used for AuNS synthesis, is the Brust-

Schiffrin method, which is a two-phase synthesis that leads to small (2-5 nm) thiolate-stabilized AuNSs.[47]

The most common method for the synthesis of AuNRs is using a seed-mediated approach. Murphy *et al.* and Liz-Marzan *et al.* pioneered AuNR synthesis in the early 2000s. The Murphy method, still widely used today, uses 3-4 nm AuNPs as seeds. The seeds are then added into a growth solution containing $HAuCl_4$, cetyltrimethylammonium bromide (CTAB) as the stabilizing agent, ascorbic acid as the reducing agent, and silver nitrate to control the nanorod aspect ratio.[48] Similar syntheses have been reported that produce AuNRs of differing aspect ratios and/or different absolute dimensions. Zubarev *et al.* reported a seed-mediated synthesis using hydroquinone as the reducing agent which led to higher aspect ratio AuNRs.[49] Murray *et al.* used binary surfactant mixtures to produce AuNRs of all different sizes and aspect ratios, including much larger AuNRs that were 175 nm long and 50 nm wide.[50] More recently, Murphy *et al.* reported the synthesis of miniature AuNRs, where a variety of different aspect ratios could be synthesized, but the width of the AuNR never exceeded 10 nm.[51]

While the aforementioned AuNS and AuNR syntheses are not all encompassing of the current synthetic library, they are some of the most widely used methods in nanoparticle synthesis today.[20,52] Despite all of the reported synthesis of AuNRs that give excellent shape and size control, there is still an ongoing debate on the actual growth mechanisms of AuNRs.[26,27,53–56] In particular, the role that silver plays in directing the aspect ratio has been of great interest to the scientific community. There are three main proposed mechanisms that have garnered support in the literature.[26] One of the proposed mechanisms is that the addition of Ag(I) changes the shape of the CTAB micelle and the micelle then acts as a soft template for the growth of AuNRs.[26] The two other mechanisms, which have garnered more support, are very difficult to distinguish from one

another. The first of which is that a monolayer of Ag(0) preferentially deposits on the longitudinal facets, stopping the growth on those facets and thus favoring anisotropic growth; this is referred to as the silver under-potential deposition mechanism.[26] A similar mechanism is that a silver(I) bromide complex acts as a face-specific capping agent, and thus favors anisotropic growth.[26] While the exact mechanisms of AuNR growth are not known, the research that has went into understanding the mechanisms has led to much more reproducible and reliable syntheses of AuNRs.

AuNPs are often synthesized with standard surface stabilizing agents, such as CTAB or citrate. However, there are a lot of different surface modifications that can be applied to AuNPs post-synthetically. Nearly all applications of AuNPs require some surface modification, especially in the case of CTAB-capped nanoparticles as the CTAB is toxic.[23,57] One common surface medication made to AuNPs is functionalizing the surface with polymers. This is often done either through a polymer wrapping process, or using thiolated polymers to covalently bond the polymers to the AuNP surface.[23,58,59] Another common post-synthetic surface modification is the replacement of the stabilizing agent, such as CTAB, with alkanethiols.[57,60–62] More advanced surface modifications include the creation of heterostructures through the deposition of other metals, or metal oxides on the surface of AuNPs.[23] It is also possible to selectively modify the surface of ends or the sides of AuNRs.[63,64] One major challenge in the surface modification of AuNPs is that it can be very difficult to accurately characterize what ligand is on the surface on the AuNP. Recently, a number of NMR, TEM, and X-ray based techniques have made great improvements in the ability to characterize AuNP surfaces, but it still remains a challenge.[65–69]

1.4 Metal-Organic Frameworks

Metal-organic frameworks (MOFs) are highly porous materials that were pioneered in the 1990s.[70] Yaghi *et al.* spearheaded the growth of this field in and presently there are over 90,000 MOF structures reported.[70,71] MOFs are composed of a series of metal nodes, referred to as secondary building units (SBUs), connected by organic linkers. Due to their building block nature, there is a near endless amount of possible structures. There is also great flexibility in the geometry, size, and functionality for both the SBUs and organic linkers.[70,72–75] The development of MOFs is often referred to as reticular chemistry. A target structure can be chosen, which can then be broken down into its fundamental geometric units allowing for the identification of the appropriate SBUs and organic linkers to achieve the desired target material.[73]

1.4.1 Properties and Applications

MOFs most advantageous properties are their crystallinity, porosity, and tunability.[70,73,76,77] The crystallinity of these materials allows for the much easier characterization of the structure, and significantly helps with the predictability of the synthesized structures from the individual building blocks.[70,73] MOFs are among the most porous materials known, having surface areas that exceed that of zeolites and carbons. Typical MOF surface areas can range anywhere from 1,000 to 10,000 m^2/g, and most MOFs have a porosity that is greater than 50% of their volume.[70] Most MOFs have micropores, while mesoporous MOFs can be synthesized, it often comes at a stability cost.[72,78] Lastly, the tunability of MOFs makes them very attractive materials. There is now a huge library of SBUs and organic linkers that can be combined to make MOFs, but their tunability extends beyond individual building blocks.[73] MOFs have been created that have mixed metals or mixed ligands.[79–81] There has also been the development of isoreticular MOFs, where linkers are extended

to expand the MOF pore size but maintain the same overall structure, illustrated in Figure 1.3. The pores of MOFs are very tunable as well. Linkers can be modified to generate specific functional groups that will be present within the MOF pores.[82] This can also be done post-synthetically, where it is possible to exchange certain MOF building block or just introduce new moieties at reactive sites within the MOF.[82] The crystallinity and porosity of MOFs coupled with their tunability bot pre- and post-synthetically has led to their interest and exponential development. With the reticular nature of MOF synthesis, researchers are now able to rationally synthesis desired structures for specific applications.[75]

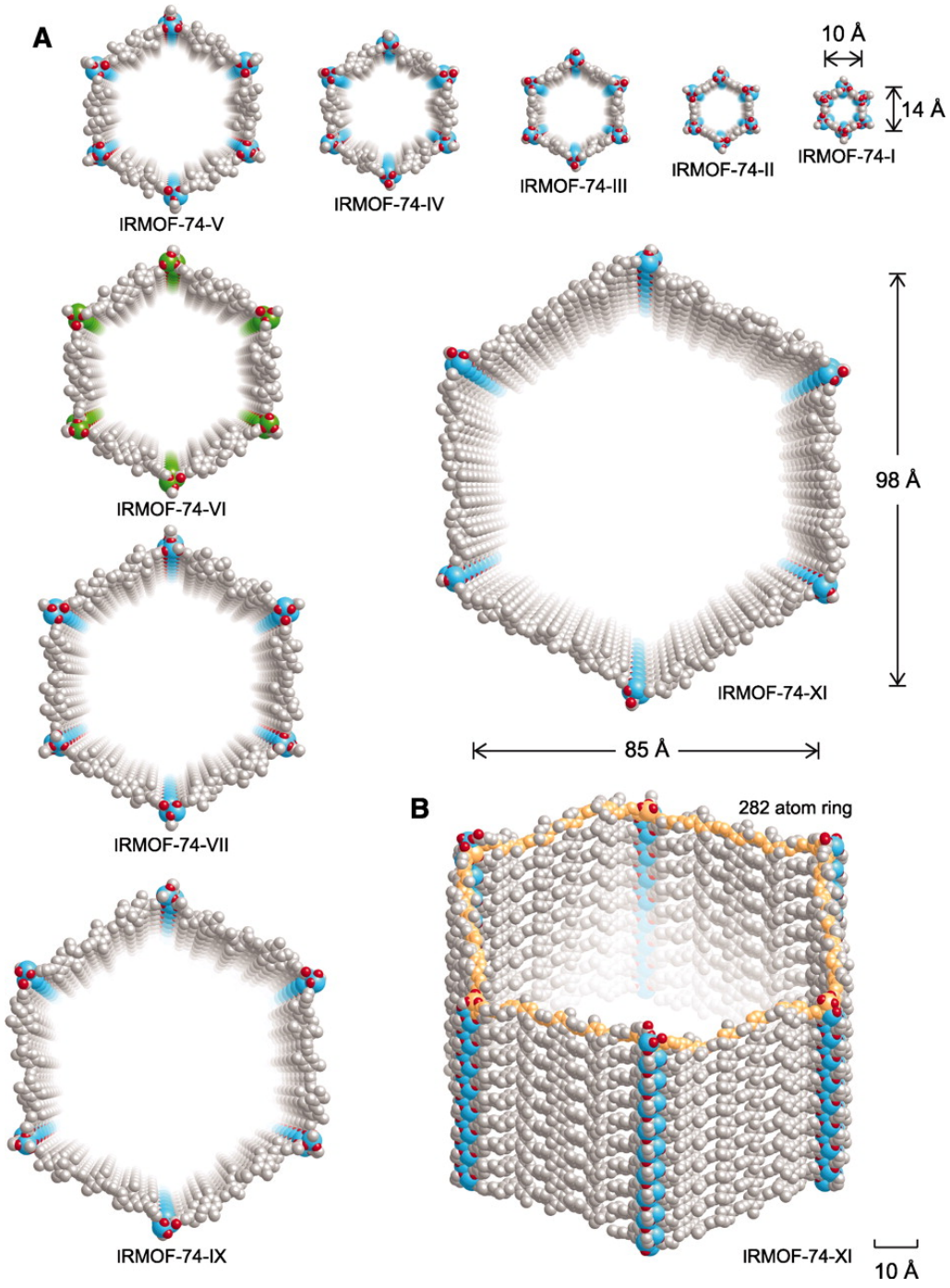

Figure 1.3: Example of an isoreticular MOF series where the organic linker is continually extended, which generates MOFs of the same core structure but expanded pore size. From Deng, H.; et al. Large-Pore Apertures in a Series of Metal-Organic Frameworks. *Science* **2012**, *336*, 1018-1023. Reprinted with permission from AAAS.

Due to their very high surface areas, MOFs are most widely studied for applications surrounding gas storage and separations.[70,83] To make alternative fuels more viable options, storing fuel gases such as methane and hydrogen under less extreme conditions is necessary. A vessel filled with MOFs can capture and store more than twice the amount of methane at room temperature compared to an empty vessel.[70] The gas adsorption ability of MOFs can also be used as a gas separations technique to improve air quality. The carbon dioxide uptake at capacity at room temperature of MOFs is higher than any other porous material. MOFs can also be tuned to have some level of selectivity for the adsorption of other gases such as hydrocarbons, ammonia, and water.[70] While gas storage and separations have drawn the most interest, MOFs have also been shown to have promise in other applications such as drug delivery, batteries, catalysis, and sensing.[70,73,83]

1.4.2 Metal-Organic Framework Nanoparticles

While MOFs were introduced in the 1990s, it wasn't until around 2010 that MOF nanoparticles (nanoMOFs) with reproducible size and morphology were produced.[74,84–88] NanoMOFs maintain the same level of porosity observed as the more traditional micron-sized MOF crystallites, but they have the advantage of being colloidal stable.[84,86,88] This colloidal stability is of particular importance for the biomedical applications of MOFs. In addition to the colloidal stability, nanoMOFs have more morphological control than their bulk counterparts and nanoMOFs can be assembled into larger superlattices.[85,89]

In the last decade a number of different synthetic approaches have been used to create nanoMOFs. In general, three main strategies are used: nanoreactor confinement, rapid nucleation, or coordination modulation.[74,84,85] Perhaps the simplest synthetic method, nanoreactor

confinement, uses immiscible solvents such as an oil and water. The rapid nucleation approach will produce nanoMOFs through the addition of an initiation step such as the addition of a solvent or change in the pH. Rapid nucleation can also be promoted using accelerated heating methods such as microwaves or ultrasound. For the last general approach, coordination modulation, molecules are added into the reaction mixture to bind to certain crystals facets to stop growth, or limit the number of nucleation sites. The molecules, referred to as modulators, often are singular functionalized, unlike the MOF bridging ligands which have multiple functional groups. This approach will synthesize nanoMOFs with different surface chemistries. Using these methods, nanoMOFs have been produced that are spherical, cubic, hexagonal, and rod shaped.[84,87,88]

While the surface functionalization of nanoMOFs is not as extensive as other types of nanoparticles, such as gold, it is still possible to modify the surface of nanoMOFs. Granick *et al.* demonstrated the surface functionalization of a dye onto nanoMOF.[84,89] It has also been shown that phosphate-terminated lipids can be attached to the nanoMOF surface, and DNA can also be conjugated to the surface.[84,85,88] One common approach to modifying nanoMOF surfaces is to modify the original organic linker with a reactive functional group that can be accessed post-synthetically. This method helps to maintain the MOF structure, but allows for the introduction of functional groups such as azides, where click chemistry can be used to covalently attach other ligands to the surface.[84]

1.4.3 Metal-Organic Framework Shells on Nanoparticles

For the work presented in this dissertation, the most interesting surface modification of AuNPs is the synthesis of porous shells around the AuNPs. Synthesizing porous shells around AuNPs is very attractive because it can lead to enhanced stability, and significantly improve

AuNPs for sensing and drug delivery.[90,91] The most common type of porous of shells on AuNPs is mesoporous silica.[63,90,92,93] An alternative type of porous shell around NPs is one composed of a MOF. A MOF shell possesses some advantages over a silica shell in that the MOF is crystalline and has defined pore structures. This means the surface of AuNP coated with a MOF (AuNR@MOF) will have a uniform pore structure, unlike silica coated AuNPs.

Synthesizing MOF shells onto metal nanoparticles requires the proper surface functionalization of the metal NPs. There is a large lattice mismatch between metal NPs and MOFs, so the NP surface must be modified to promote the nucleation of the MOF on the NP surface as opposed to self-nucleating.[94] The desired core shell structure for this work, Figure 1.4, of singularly NPs encapsulated with a MOF can be difficult to achieve. If the MOF self-nucleates it will often lead to the decoration of NPs on the surface of the MOF rather than the encapsulation of the NPs. It is also easy for the MOF shell to encapsulate multiple NPs. Certain NP surface functionalizations, such as polyvinylpyrrolidone and 11-mercaptoundecanoic acid have shown a tendency to promote the growth of a variety of MOF shells on NPs, while some MOFs require more unique NP surfaces to promote their growth.[94]

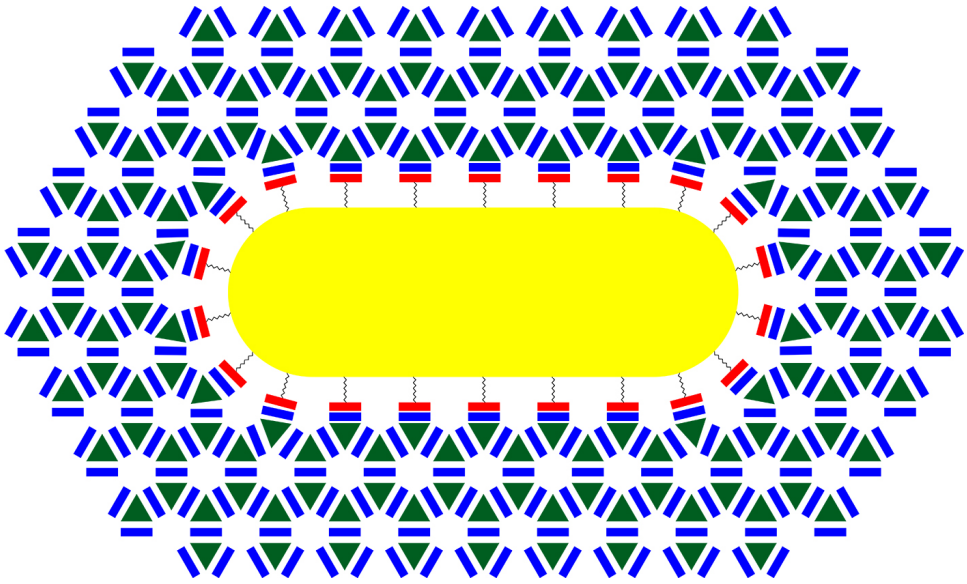

Figure 1.4: Illustration of the desired core-shell nanoparticle composed of a AuNR core and a MOF shell. Reprinted with permission from Hinman, J. G.; Turner, J. G.; Hofmann, D. M.; Murphy, C. J. Layer-by-Layer Synthesis of Conformal Metal-Organic Framework Shells on Gold Nanorods. *Chem. Mater.* **2018**, *30* (20), 7255-7261. Copyright 2018 American Chemical Society.

There have been a number of reported syntheses of AuNPs encapsulated by MOF shells, all with varying degrees over shell uniformity and shell thickness control. Layer-by-layer techniques have been used to provide exceptional control over the thickness of the MOF shell, but these methods are often time consuming and less reproducible.[95,96] Other one-pot methods have been shown for the synthesis of MOFs on both AuNRs and AuNSs. These methods have a significant advantage in their ease of synthesis, but they often produce shells that are not conformal and there is not much thickness control.[97–104] The synthesized AuNP@MOF nanoparticles have been demonstrated as great therapeutics through their synergistic chemo-photothermal therapy abilities.[102,103] They have also been shown to help in the areas of catalysis and sensing.[96,98,101,105,106]

For the purpose of the work in this thesis, AuNR@MOF provide a great platform to study the ability to control molecules orientation at the surface of nanoparticles.

1.5 Nanoparticle Interactions with Soft Matter

The properties and applications of inorganic nanoparticles has been discussed, with an emphasis on gold nanoparticles and metal-organic framework nanoparticles. While these nanomaterials have extraordinary properties, they are only so useful as colloidal solutions. For applied research purposes, these nanomaterials come in contact with many other forms of matter. The focus of the work presented in this thesis will be the interaction of these inorganic nanomaterials with different forms of soft matter. The term soft matter refers to materials that can be altered by thermal or mechanical stress such as liquids, polymers, gels, and biological materials.[107] The interactions of NPs with these forms of soft matter can be done intentionally, or they may be unavoidable interactions. For example, NPs may be purposely dispersed into a polymer for the fabrication of an electronic device.[108] In contrast, nanoparticles used in biological applications will unavoidably interact with different biomolecules.[109] Furthering the understanding of the interactions of polymers, biomolecules, and other forms of matter at these nanoscale surfaces will help improve the applied technology these nanoparticles can be used for.

1.5.1 The Nano-Bio Interface and the Protein Corona

Nanoparticles have many biological applications including drug delivery, imaging, diagnostics, and therapeutics.[35] When NPs are used for biological applications that encounter many different conditions throughout the lifetime of their biological fate. These conditions can include binding to biomolecules, cellular uptake, stress due to rapid blood flow, and enzymatic

degradation.[109] With all of these different conditions encountered, it remains a challenge to produce quality nanoparticles that can handle each type of potential encounter. One of the largest challenges facing the field today is understanding and controlling the protein corona.[34,109,110] When nanoparticles are dispersed in biological fluid, biomolecules adsorb to the surface, an illustration is shown in Figure 1.5. This corona of biomolecules is largely made up of proteins, hence the term protein corona. This protein corona has biomolecules that are adsorbed tightly to the nanoparticle, known as the hard corona, and biomolecules that are more dynamically exchanged, known as the soft corona. The protein corona then serves as the nanoparticles biological identity and largely influences the nanoparticle's targeting efficiency, cellular uptake, and toxicity.[34,109,110] The protein corona is also the most fundamental interaction at the nano-bio interface. Being able to control or predict the chemical makeup of the protein corona would vastly help improve the design of NPs for their biological applications. Presently, this is difficult to understand and control due to the complex nature of the protein corona. The NP shape, size, surface, and charge all heavily influence what biomolecules adsorb to the surface.[109] There are also numerous environmental parameters including temperature, pH, incubation time, and concentration of biomolecules that further complicate the chemical makeup of the protein corona.[109]

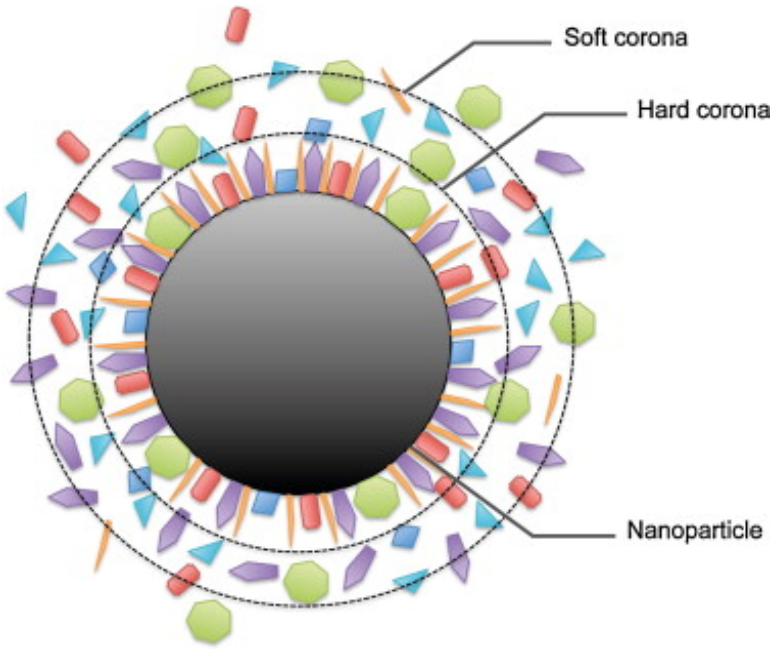

Figure 1.5: Illustration of the protein corona that is formed when nanoparticles are exposed to biological media. A hard corona of biomolecules adsorbs to the surface of the nanoparticle making them less dynamic than the proteins more loosely adsorbed, referred to as the soft corona. Reprinted from Wolfram, J.; Yang, Y.; Shen, J.; Moten, A.; Chen, C.; Shen, H.; Ferrari, M.; Zhao, Y. The nano-plasma interface: Implications of the protein corona. *Colloids Surf. B* **2014**, *124*, 17-24. Copyright 2014, with permission from Elsevier.

Much effort has been put forth to try and understanding the protein corona, and achieve a level of control and predictability of the protein corona. Achieving control and predicting of the protein corona, would allow for the exploitation of the protein corona and make NPs biological applications much more prevalent. To date, most of the research centered around the protein corona has been done *in vitro* and centered around two main concepts. The first way people have begun to understand the protein corona, is by incubating nanoparticles with serum and subsequently identifying the proteins that are adsorbed to the surface.[111–113] Chan *et al*. recently reported a study

where AuNPs were incubated in human serum, afterwards the bound proteins were digested and identified.[111] They were able to find the relative abundance of each protein in the protein corona, and concluded that the protein corona likely has multiple complex layers. Another approach that has been used to study the protein corona is to look at the nanoparticle adsorption behavior of individual proteins of interest. Using these methods, researchers have found how proteins adsorb to the surface as a function of surface curvature, surface charge, protein deformability, and many other properties.[114–120] While there has been significant improvement in the understanding of the protein corona, more work is needed *in vivo* and more research is needed in terms of controlling the protein corona.

1.5.2 Hydrogels and Nanoparticle Composites

Nanoparticles are frequently dispersed in polymer matrices in the form of films, gels, and elastomers. NPs are used as filler materials for polymer matrices because they can impart unique properties on the polymer matrix such as making them optically active, improving mechanical properties, and improving conductivity.[121–125] For the purpose of the research presented in this thesis, AuNP composites and hydrogels will be the materials of focus. Hydrogels are polymer networks that are crosslinked in an aqueous medium forming a flexible yet fixed material. Hydrogels are mostly made of water, frequently containing upwards of 99% water by weight, making them relatively accessible and biocompatible materials.[126]

Suo *et al*. really advanced the field of hydrogels forward in 2012 with their report on tough and stretchable double-network hydrogels composed of alginate and polyacrylamide.[127] Previously, hydrogels were not very resilient or elastic materials with applications limited to cell culturing and contact lenses. The advent of double-network hydrogels, enhanced their mechanical

properties to the point where hydrogels can behave very similar to that of human tissues with toughness values around 10,000 J/m^2.[128,129] For this reason, double-network hydrogels have become heavily studied for the applications in tissue engineering and flexible electronics.[130–134] The current working principle behind the improved mechanical properties of double-network hydrogels is the incorporation of two different types of crosslinking bonding within one hydrogel system.[128,130] The improved mechanical properties arise when one of polymer network consists of weak reversible bonds, and the other polymer network contains strong irreversible bonds. In addition to the improved mechanical properties of hydrogels, other properties include self-healing, thermoresponsiveness, and increased conductivities.[126] Because many of these properties are stimuli-responsive, new age hydrogels have been explored as 'smart materials' that have different properties based upon whether an external stimulus is applied or not.

AuNPs have been added to polymer matrices like polyvinylalcohol and poly(N-isopropylacrylamide) for optical displays and microfluidics.[135–140] AuNPs have been incorporated into alginate hydrogels for image-guided drug delivery, and into chitosan hydrogels for cardiac tissue engineering.[141,142] However, there are far fewer reports of AuNPs incorporated into double network hydrogels, as the spatial control and NP stability in multi-component polymer networks is more difficult. More research is needed regarding the spatial and orientation control of AuNP in polymer networks such as double-network hydrogels to better design plasmonic polymer composites.

1.6 Conclusions

AuNPs and MOFs have unique properties that make them very attractive materials. The plasmonic properties of AuNPs make them ideal for sensing, biomedical imaging, and as

therapeutics. MOFs have incredibly high surface areas that make them great for gas storage and separations. One major challenge the field faces today is the lack of control of how other materials interact at these nanoscale surfaces. This is important because nanomaterials like AuNPs and nanoMOFs are often interfaced with other materials for their applications. This interfacing with other materials can be intentional, as is the case of dispersing nanoparticles into a polymer composite, or it may be something that is unavoidable such as the protein corona that forms around nanoparticles in biological fluid. The goal of this thesis work is to explore possible routes to control the orientation of different forms of soft matter at the nanoscale surface. This includes using the physical properties of MOFs porosity to control the orientation of biomolecules at the surface, in an effort to engineer protein coronas. It also includes controlling the orientation of AuNRs with varying surface chemistries in a stretchable hydrogel.

1.7 References

(1) Khan, I.; Saeed, K.; Khan, I. Nanoparticles: Properties, Applications and Toxicities. *Arab. J. Chem.* **2019**, *12* (7), 908–931.

(2) Mody, V. V.; Siwale, R.; Singh, A.; Mody, H. R. Introduction to Metallic Nanoparticles. *J. Pharm. Bioallied Sci.* **2010**, *2* (4), 282–289.

(3) Lohse, S. E.; Murphy, C. J. Applications of Colloidal Inorganic Nanoparticles: From Medicine to Energy. *J. Am. Chem. Soc.* **2012**, *134* (38), 15607–15620.

(4) Ealias, A. M.; Saravanakumar, M. P. A Review on the Classification, Characterization, Synthesis of Nanoparticles and Their Application. *IOP Conf. Ser.: Mater. Sci. Eng.* **2017**, *263* (3), 032019.

(5) Kelly, K. L.; Coronado, E.; Zhao, L. L.; Schatz, G. C. The Optical Properties of Metal Nanoparticles: The Influence of Size, Shape, and Dielectric Environment. *J. Phys. Chem. B* **2003**, *107* (3), 668–677.

(6) Chen, H.; Shao, L.; Li, Q.; Wang, J. Gold Nanorods and Their Plasmonic Properties. *Chem. Soc. Rev.* **2013**, *42* (7), 2679–2724.

(7) Enuston, B. V.; Turkevich, J. Coagulation of Colloidal Gold. *J. Am. Chem. Soc.* **1963**, *85* (21), 3317–3328.

(8) Jeevanandam, J.; Barhoum, A.; Chan, Y. S.; Dufresne, A.; Danquah, M. K. Review on Nanoparticles and Nanostructured Materials: History, Sources, Toxicity and Regulations. *Beilstein J. Nanotechnol.* **2018**, *9*, 1050–1074.

(9) Wu, Z.; Yang, S.; Wu, W. Shape Control of Inorganic Nanoparticles from Solution. *Nanoscale* **2016**, *8* (3), 1237–1259.

(10) Tsuzuki, T. Commercial Scale Production of Inorganic Nanoparticles. *Int. J. Nanotechnol.* **2009**, *6* (5/6), 567–578.

(11) Daniel, M.-C.; Astruc, D. Gold Nanoparticles: Assembly, Supramolecular Chemistry, Quantum-Size-Related Properties, and Applications toward Biology, Catalysis, and Nanotechnology. *Chem. Rev.* **2004**, *104*, 293–346.

(12) Mohammed, L.; Gomaa, H. G.; Ragab, D.; Zhu, J. Magnetic Nanoparticles for Environmental and Biomedical Applications: A Review. *Particuology* **2017**, *30*, 1–14.

(13) Jeelani, P. G.; Mulay, P.; Venkat, R.; Ramalingam, C. Multifaceted Application of Silica Nanoparticles. A Review. *Silicon* **2020**, *12* (6), 1337–1354.

(14) Sirelkhatim, A.; Mahmud, S.; Seeni, A.; Kaus, N. H. M.; Ann, L. C.; Bakhori, S. K. M.; Hasan, H.; Mohamad, D. Review on Zinc Oxide Nanoparticles: Antibacterial Activity and Toxicity Mechanism. *Nano-Micro Lett.* **2015**, *7* (3), 219–242.

(15) Tonga, G. Y.; Moyano, D. F.; Kim, C. S.; Rotello, V. M. Inorganic Nanoparticles for Therapeutic Delivery: Trials, Tribulations and Promise. *Curr. Opin. Colloid Interface Sci.* **2014**, *19* (2), 49–55.

(16) Giner-Casares, J. J.; Henriksen-Lacey, M.; Coronado-Puchau, M.; Liz-Marzán, L. M. Inorganic Nanoparticles for Biomedicine: Where Materials Scientists Meet Medical Research. *Mater. Today* **2016**, *19* (1), 19–28.

(17) Kim, D.; Kim, J.; Park, Y. I.; Lee, N.; Hyeon, T. Recent Development of Inorganic Nanoparticles for Biomedical Imaging. *ACS Central Sci.* **2018**, *4* (3), 324–336.

(18) Kango, S.; Kalia, S.; Celli, A.; Njuguna, J.; Habibi, Y.; Kumar, R. Surface Modification of Inorganic Nanoparticles for Development of Organic–Inorganic Nanocomposites—A Review. *Prog. Polym. Sci.* **2013**, *38* (8), 1232–1261.

(19) Zhan, C.; Chen, X.-J.; Yi, J.; Li, J.-F.; Wu, D.-Y.; Tian, Z.-Q. From Plasmon-Enhanced Molecular Spectroscopy to Plasmon-Mediated Chemical Reactions. *Nat. Rev. Chem.* **2018**, *2*, 216–230.

(20) Zhao, P.; Li, N.; Astruc, D. State of the Art in Gold Nanoparticle Synthesis. *Coord. Chem. Rev.* **2013**, *257*, 638–665.

(21) Murphy, C. J.; Sau, T. K.; Gole, A. M.; Orendorff, C. J.; Gao, J.; Gou, L.; Hunyadi, S. E.; Li, T. Anisotropic Metal Nanoparticles: Synthesis, Assembly, and Optical Applications. *J. Phys. Chem. B* **2005**, *109* (29), 13857–13870.

(22) Brinker, C. J.; Lu, Y.; Sellinger, A.; Fan, H. Evaporation-Induced Self-Assembly: Nanostructures Made Easy. *Adv. Mater.* **1999**, *11* (7), 579–585.

(23) Burrows, N. D.; Lin, W.; Hinman, J. G.; Dennison, J. M.; Vartanian, A. M.; Abadeer, N. S.; Grzincic, E. M.; Jacob, L. M.; Li, J.; Murphy, C. J. Surface Chemistry of Gold Nanorods. *Langmuir* **2016**, *32* (39), 9905–9921.

(24) Nam, J.; Won, N.; Bang, J.; Jin, H.; Park, J.; Jung, S.; Jung, S.; Park, Y.; Kim, S. Surface Engineering of Inorganic Nanoparticles for Imaging and Therapy. *Adv. Drug Deliv. Rev.* **2013**, *65* (5), 622–648.

(25) Sharma, V.; Park, K.; Srinivasarao, M. Colloidal Dispersion of Gold Nanorods: Historical Background, Optical Properties, Seed-Mediated Synthesis, Shape Separation and Self-Assembly. *Mater. Sci. Eng. R Rep.* **2009**, *65*, 1–38.

(26) Lohse, S. E.; Murphy, C. J. The Quest for Shape Control: A History of Gold Nanorod Synthesis. *Chem. Mater.* **2013**, *25* (8), 1250–1261.

(27) Tong, W.; Walsh, M. J.; Mulvaney, P.; Etheridge, J.; Funston, A. M. Control of Symmetry Breaking Size and Aspect Ratio in Gold Nanorods: Underlying Role of Silver Nitrate. *J. Phys. Chem. C* **2017**, *121* (6), 3549–3559.

(28) Polte, J. Fundamental Growth Principles of Colloidal Metal Nanoparticles – a New Perspective. *Cryst. Eng. Comm.* **2015**, *17*, 6809–6830.

(29) Murphy, C. J.; Chang, H.-H.; Falagan-Lotsch, P.; Gole, M. T.; Hofmann, D. M.; Hoang, K. N. L.; McClain, S. M.; Meyer, S. M.; Turner, J. G.; Unnikrishnan, M.; Wu, M.; Zhang, X.; Zhang, Y. Virus-Sized Gold Nanorods: Plasmonic Particles for Biology. *Acc. Chem. Res.* **2019**, *52* (8), 2124–2135.

(30) Mosquera, J.; García, I.; Liz-Marzán, L. M. Cellular Uptake of Nanoparticles versus Small Molecules: A Matter of Size. *Acc. Chem. Res.* **2018**, *51* (9), 2305–2313.

(31) Cai, R.; Ren, J.; Ji, Y.; Wang, Y. W.; Liu, Y.; Chen, Z.; Sabet, Z. F.; Wu, X.; Lynch, I.; Chen, C. Corona of Thorns: The Surface Chemistry-Mediated Protein Corona Perturbs the Recognition and Immune Response of Macrophages. *ACS Appl. Mater. Interfaces* **2019**, *12*, 1997–2008.

(32) Wang, P.; Wang, X.; Wang, L.; Hou, X.; Liu, W.; Chen, C. Interaction of Gold Nanoparticles with Proteins and Cells. *Sci. Technol. Adv. Mater.* **2016**, *16* (3), 034610.

(33) García-Álvarez, R.; Hadjidemetriou, M.; Sánchez-Iglesias, A.; Liz-Marzán, L. M.; Kostarelos, K. In Vivo Formation of Protein Corona on Gold Nanoparticles. The Effect of Their Size and Shape. *Nanoscale* **2018**, *10* (3), 1256–1264.

(34) Singh, N.; Marets, C.; Boudon, J.; Millot, N.; Saviot, L.; Maurizi, L. In Vivo Protein Corona on Nanoparticles: Does the Control of All Material Parameters Orient the Biological Behavior? *Nanoscale Adv.* **2021**, *3* (5), 1209–1229.

(35) Murphy, C. J.; Vartanian, A. M.; Geiger, F. M.; Hamers, R. J.; Pedersen, J.; Cui, Q.; Haynes, C. L.; Carlson, E. E.; Hernandez, R.; Klaper, R. D.; Orr, G.; Rosenzweig, Z. Biological Responses to Engineered Nanomaterials: Needs for the Next Decade. *ACS Cent. Sci.* **2015**, *1* (3), 117–123.

(36) Chang, H.-H.; Gole, M. T.; Murphy, C. J. A Golden Time for Nanotechnology. *MRS Bull.* **2020**, *45* (5), 387–393.

(37) Huo, D.; Kim, M. J.; Lyu, Z.; Shi, Y.; Wiley, B. J.; Xia, Y. One-Dimensional Metal Nanostructures: From Colloidal Syntheses to Applications. *Chem. Rev.* **2019**, *119* (15), 8972–9073.

(38) Willets, K. A.; Duyne, R. P. V. Localized Surface Plasmon Resonance Spectroscopy and Sensing. *Annu. Rev. Phys. Chem.* **2007**, *58* (1), 267–297.

(39) Langer, J.; Aberasturi, D. J. de; Aizpurua, J.; Alvarez-Puebla, R. A.; Auguié, B.; Baumberg, J. J.; Bazan, G. C.; Bell, S. E. J.; Boisen, A.; Brolo, A. G.; Choo, J.; Cialla-May, D.; Deckert, V.; Fabris, L.; Faulds, K.; Abajo, F. J. G. de; Goodacre, R.; Graham, D.; Haes, A. J.; Haynes, C. L.; Huck, C.; Itoh, T.; Käll, M.; Kneipp, J.; Kotov, N. A.; Kuang, H.; Ru, E. C. L.; Lee, H. K.; Li, J.-F.; Ling, X. Y.; Maier, S. A.; Mayerhöfer, T.; Moskovits, M.; Murakoshi, K.; Nam, J.-M.; Nie, S.; Ozaki, Y.; Pastoriza-Santos, I.; Pérez-Juste, J.; Popp, J.; Pucci, A.; Reich, S.; Ren, B.; Schatz, G. C.; Shegai, T.; Schlücker, S.; Tay, L.-L.; Thomas, K. G.; Tian, Z.-Q.; Duyne, R. P. V.; Vo-Dinh, T.; Wang, Y.; Willets, K. A.; Xu, C.; Xu, H.; Xu, Y.; Yamamoto, Y. S.; Zhao, B.; Liz-Marzán, L. M. Present and Future of Surface-Enhanced Raman Scattering. *ACS Nano* **2019**, *14* (1), 28–117.

(40) Ali, M. R. K.; Wu, Y.; El-Sayed, M. A. Gold-Nanoparticle-Assisted Plasmonic Photothermal Therapy Advances Toward Clinical Application. *J. Phys. Chem. C* **2019**, *123*, 15375–15393.

(41) Abadeer, N. S.; Murphy, C. J. Recent Progress in Cancer Thermal Therapy Using Gold Nanoparticles. *J. Phys. Chem. C* **2016**, *120* (9), 4691–4716.

(42) Xu, W.; Qian, J.; Hou, G.; Suo, A.; Wang, Y.; Wang, J.; Sun, T.; Yang, M.; Wan, X.; Yao, Y. Hyaluronic Acid-Functionalized Gold Nanorods with PH/NIR Dual-Responsive Drug Release for Synergetic Targeted Photothermal Chemotherapy of Breast Cancer. *ACS Appl. Mater. Interfaces* **2017**, *9* (42), 36533–36547.

(43) Chen, Y.-S.; Zhao, Y.; Yoon, S. J.; Gambhir, S. S.; Emelianov, S. Miniature Gold Nanorods for Photoacoustic Molecular Imaging in the Second Near-Infrared Optical Window. *Nat. Nanotechnol.* **2019**, *14* (5), 465–472.

(44) Fu, G.; Sun, D.-W.; Pu, H.; Wei, Q. Fabrication of Gold Nanorods for SERS Detection of Thiabendazole in Apple. *Talanta* **2019**, *195*, 841–849.

(45) Su, G.; Jiang, H.; Zhu, H.; Lv, J.-J.; Yang, G.; Yan, B.; Zhu, J.-J. Controlled Deposition of Palladium Nanodendrites on the Tips of Gold Nanorods and Their Enhanced Catalytic Activity. *Nanoscale* **2017**, *9* (34), 12494–12502.

(46) Perrault, S. D.; Chan, W. C. W. Synthesis and Surface Modification of Highly Monodispersed, Spherical Gold Nanoparticles of 50−200 Nm. *J. Am. Chem. Soc.* **2009**, *131* (47), 17042–17043.

(47) Brust, M.; Fink, J.; Bethell, D.; Schiffrin, D. J.; Kiely, C. Synthesis and Reactions of Functionalised Gold Nanoparticles. *J. Chem. Soc. Chem. Comm.* **1995**, No. 16, 1655–1656.

(48) Gole, A.; Murphy, C. J. Seed-Mediated Synthesis of Gold Nanorods: Role of the Size and Nature of the Seed. *Chem. Mater.* **2004**, *16* (19), 3633–3640.

(49) Vigderman, L.; Zubarev, E. R. High-Yield Synthesis of Gold Nanorods with Longitudinal SPR Peak Greater than 1200 Nm Using Hydroquinone as a Reducing Agent. *Chem. Mater.* **2013**, *25* (8), 1450–1457.

(50) Ye, X.; Zheng, C.; Chen, J.; Gao, Y.; Murray, C. B. Using Binary Surfactant Mixtures To Simultaneously Improve the Dimensional Tunability and Monodispersity in the Seeded Growth of Gold Nanorods. *Nano Lett.* **2013**, *13* (2), 765–771.

(51) Chang, H.-H.; Murphy, C. J. Mini Gold Nanorods with Tunable Plasmonic Peaks beyond 1000 Nm. *Chem. Mater.* **2018**, *30* (4), 1427–1435.

(52) Hühn, J.; Carrillo-Carrion, C.; Soliman, M. G.; Pfeiffer, C.; Valdeperez, D.; Masood, A.; Chakraborty, I.; Zhu, L.; Gallego, M.; Yue, Z.; Carril, M.; Feliu, N.; Escudero, A.; Alkilany, A. M.; Pelaz, B.; Pino, P. del; Parak, W. J. Selected Standard Protocols for the Synthesis, Phase Transfer, and Characterization of Inorganic Colloidal Nanoparticles. *Chem. Mater.* **2016**, *29* (1), 399–461.

(53) Hatakeyama, Y.; Sasaki, K.; Judai, K.; Nishikawa, K.; Hino, K. Growth Behavior of Gold Nanorods Synthesized by the Seed-Mediated Method: Tracking of Reaction Progress by Time-Resolved X-Ray Absorption Near-Edge Structure, Small-Angle X-Ray Scattering, and Ultraviolet–Visible Spectroscopy. *J. Phys. Chem. C* **2018**, *122* (14), 7982–7991.

(54) Ye, W.; Krüger, K.; Sánchez-Iglesias, A.; García, I.; Jia, X.; Sutter, J.; Celiksoy, S.; Foerster, B.; Liz-Marzán, L. M.; Ahijado-Guzmán, R.; Sönnichsen, C. CTAB Stabilizes Silver on Gold Nanorods. *Chem. Mater.* **2020**, *32*, 1650–1656.

(55) Walsh, M. J.; Tong, W.; Katz-Boon, H.; Mulvaney, P.; Etheridge, J.; Funston, A. M. A Mechanism for Symmetry Breaking and Shape Control in Single-Crystal Gold Nanorods. *Acc. Chem. Res.* **2017**, *50* (12), 2925–2935.

(56) Moreau, L. M.; Jones, M. R.; Roth, E. W.; Wu, J.; Kewalramani, S.; O'Brien, M. N.; Chen, B.-R.; Mirkin, C. A.; Bedzyk, M. J. The Role of Trace Ag in the Synthesis of Au Nanorods. *Nanoscale* **2019**, *11* (24), 11744–11754.

(57) Indrasekara, A. S. D. S.; Wadams, R. C.; Fabris, L. Ligand Exchange on Gold Nanorods: Going Back to the Future. *Part. Part. Syst. Character.* **2014**, *31* (8), 819–838.

(58) Schulz, F.; Friedrich, W.; Hoppe, K.; Vossmeyer, T.; Weller, H.; Lange, H. Effective PEGylation of Gold Nanorods. *Nanoscale* **2016**, *8* (13), 7296–7308.

(59) Gole, A.; Murphy, C. J. Polyelectrolyte-Coated Gold Nanorods: Synthesis, Characterization and Immobilization. *Chem. Mater.* **2005**, *17* (6), 1325–1330.

(60) Caño, R. del; Gisbert-González, J. M.; González-Rodríguez, J.; Sánchez-Obrero, G.; Madueño, R.; Blázquez, M.; Pineda, T. Effective Replacement of Cetyltrimethylammonium Bromide (CTAB) by Mercaptoalkanoic Acids on Gold Nanorod (AuNR) Surfaces in Aqueous Solutions. *Nanoscale* **2020**, *12*, 658–668.

(61) Kluenker, M.; Mondeshki, M.; Tahir, M. N.; Tremel, W. Monitoring Thiol–Ligand Exchange on Au Nanoparticle Surfaces. *Langmuir* **2018**, *34* (4), 1700–1710.

(62) Centi, S.; Cavigli, L.; Borri, C.; Milanesi, A.; Banchelli, M.; Chioccioli, S.; Khlebtsov, B. N.; Khlebtsov, N. G.; Matteini, P.; Bogani, P.; Ratto, F.; Pini, R. Small Thiols Stabilize the Shape of Gold Nanorods. *J. Phys. Chem. C* **2020**, *124* (20), 11132–11140.

(63) Hinman, J. G.; Eller, J. R.; Lin, W.; Li, J.; Li, J.; Murphy, C. J. Oxidation State of Capping Agent Affects Spatial Reactivity on Gold Nanorods. *J. Am. Chem. Soc.* **2017**, *139*, 9851–9854.

(64) Burrows, N. D.; Vartanian, A. M.; Abadeer, N. S.; Grzincic, E. M.; Jacob, L. M.; Lin, W.; Li, J.; Dennison, J. M.; Hinman, J. G.; Murphy, C. J. Anisotropic Nanoparticles and Anisotropic Surface Chemistry. *J. Phys. Chem. Lett.* **2016**, *7* (4), 632–641.

(65) Wu, M.; Vartanian, A. M.; Chong, G.; Pandiakumar, A. K.; Hamers, R. J.; Hernandez, R.; Murphy, C. J. Solution NMR Analysis of Ligand Environment in Quaternary Ammonium-Terminated Self-Assembled Monolayers on Gold Nanoparticles: The Effect of Surface Curvature and Ligand Structure. *J. Am. Chem. Soc.* **2019**, *141* (10), 4316–4327.

(66) Janicek, B. E.; Hinman, J. G.; Hinman, J. J.; Bae, S. hyun; Wu, M.; Turner, J.; Chang, H.-H.; Park, E.; Lawless, R.; Suslick, K. S.; Murphy, C. J.; Huang, P. Y. Quantitative Imaging of Organic Ligand Density on Anisotropic Inorganic Nanocrystals. *Nano Lett.* **2019**, *19* (9), 6308–6314.

(67) Smith, A. M.; Marbella, L. E.; Johnston, K. A.; Hartmann, M. J.; Crawford, S. E.; Kozycz, L. M.; Seferos, D. S.; Millstone, J. E. Quantitative Analysis of Thiolated Ligand Exchange on Gold Nanoparticles Monitored by 1H NMR Spectroscopy. *Anal. Chem.* **2015**, *87* (5), 2771–2778.

(68) Xia, X.; Yang, M.; Wang, Y.; Zheng, Y.; Li, Q.; Chen, J.; Xia, Y. Quantifying the Coverage Density of Poly(Ethylene Glycol) Chains on the Surface of Gold Nanostructures. *ACS Nano* **2011**, *6* (1), 512–522.

(69) Hore, M. J. A.; Ye, X.; Ford, J.; Gao, Y.; Fei, J.; Wu, Q.; Rowan, S. J.; Composto, R. J.; Murray, C. B.; Hammouda, B. Probing the Structure, Composition, and Spatial Distribution of Ligands on Gold Nanorods. *Nano Lett.* **2015**, *15* (9), 5730–5738.

(70) Furukawa, H.; Cordova, K. E.; O'Keeffe, M.; Yaghi, O. M. The Chemistry and Applications of Metal-Organic Frameworks. *Science* **2013**, *341* (6149), 1230444.

(71) Moosavi, S. M.; Nandy, A.; Jablonka, K. M.; Ongari, D.; Janet, J. P.; Boyd, P. G.; Lee, Y.; Smit, B.; Kulik, H. J. Understanding the Diversity of the Metal-Organic Framework Ecosystem. *Nat. Commun.* **2020**, *11*, 4068.

(72) Yuan, S.; Feng, L.; Wang, K.; Pang, J.; Bosch, M.; Lollar, C.; Sun, Y.; Qin, J.; Yang, X.; Zhang, P.; Wang, Q.; Zou, L.; Zhang, Y.; Zhang, L.; Fang, Y.; Li, J.; Zhou, H.-C. Stable Metal-Organic Frameworks: Design, Synthesis, and Applications. *Adv. Mater.* **2018**, *30* (37), 1704303.

(73) Freund, R.; Canossa, S.; Cohen, S. M.; Yan, W.; Deng, H.; Guillerm, V.; Eddaoudi, M.; Madden, D. G.; Fairen-Jimenez, D.; Lyu, H.; Macreadie, L. K.; Ji, Z.; Zhang, Y.; Wang, B.; Haase, F.; Wöll, C.; Zaremba, O.; Andreo, J.; Wuttke, S.; Diercks, C. S. 25 Years of Reticular Chemistry. *Angew. Chem. Int. Ed.* **2021**, *Article ASAP*.

(74) Stock, N.; Biswas, S. Synthesis of Metal-Organic Frameworks (MOFs): Routes to Various MOF Topologies, Morphologies, and Composites. *Chem. Rev.* **2011**, *112* (2), 933–969.

(75) Kalmutzki, M. J.; Hanikel, N.; Yaghi, O. M. Secondary Building Units as the Turning Point in the Development of the Reticular Chemistry of MOFs. *Sci. Adv.* **2018**, *4* (10), eaat9180.

(76) Hendon, C. H.; Rieth, A. J.; Korzyński, M. D.; Dincă, M. Grand Challenges and Future Opportunities for Metal–Organic Frameworks. *ACS Cent. Sci.* **2017**, *3* (6), 554–563.

(77) Gangu, K. K.; Maddila, S.; Mukkamala, S. B.; Jonnalagadda, S. B. A Review on Contemporary Metal-Organic Framework Materials. *Inorganica Chim. Acta* **2016**, *446* (C), 61–74.

(78) Senkovska, I.; Kaskel, S. Ultrahigh Porosity in Mesoporous MOFs: Promises and Limitations. *Chem. Commun.* **2014**, *50* (54), 7089–7098.

(79) Qin, J.-S.; Yuan, S.; Wang, Q.; Alsalme, A.; Zhou, H.-C. Mixed-Linker Strategy for the Construction of Multifunctional Metal–Organic Frameworks. *J. Mater. Chem. A* **2017**, *5* (9), 4280–4291.

(80) Abednatanzi, S.; Derakhshandeh, P. G.; Depauw, H.; Coudert, F.-X.; Vrielinck, H.; Voort, P. V. D.; Leus, K. Mixed-Metal Metal–Organic Frameworks. *Chem. Soc. Rev.* **2019**, *48* (9), 276–31.

(81) Masoomi, M. Y.; Morsali, A.; Dhakshinamoorthy, A.; García, H. Mixed-Metal MOFs: Unique Opportunities in Metal-organic Framework Functionality and Design. *Angew. Chem.* **2019**, *131*, 15330–15447.

(82) Ji, Z.; Wang, H.; Canossa, S.; Wuttke, S.; Yaghi, O. M. Pore Chemistry of Metal–Organic Frameworks. *Adv. Funct. Mater.* **2020**, *30* (41), 2000238.

(83) Silva, P.; Vilela, S. M. F.; Tome, J. P. C.; J. P. C.; Paz, F. A. A. Multifunctional Metal-Organic Frameworks: From Academia to Industrial Applications. *Chem. Soc. Rev.* **2015**, *44* (19), 6774–6803.

(84) Wang, S.; McGuirk, C. M.; d'Aquino, A.; Mason, J. A.; Mirkin, C. A. Metal-Organic Framework Nanoparticles. *Adv. Mater.* **2018**, *423*, 1800202.

(85) Ploetz, E.; Engelke, H.; Lächelt, U.; Wuttke, S. The Chemistry of Reticular Framework Nanoparticles: MOF, ZIF, and COF Materials. *Adv. Funct. Mater.* **2020**, *30* (41), 1909062.

(86) Sindoro, M.; Yanai, N.; Jee, A.-Y.; Granick, S. Colloidal-Sized Metal–Organic Frameworks: Synthesis and Applications. *Acc. Chem. Res.* **2013**, *47* (2), 459–469.

(87) Carné, A.; Carbonell, C.; Imaz, I.; Maspoch, D. Nanoscale Metal–Organic Materials. *Chem. Soc. Rev.* **2011**, *40*, 291–305.

(88) Majewski, M. B.; Noh, H.; Islamoglu, T.; Farha, O. K. NanoMOFs: Little Crystallites for Substantial Applications. *J. Mater. Chem. A* **2018**, *6*, 7338–7350.

(89) Yanai, N.; Granick, S. Directional Self-Assembly of a Colloidal Metal–Organic Framework. *Angew. Chem. Int. Ed.* **2012**, *51* (23), 5638–5641.

(90) Guerrero-Martínez, A.; Pérez-Juste, J.; Liz-Marzán, L. M. Recent Progress on Silica Coating of Nanoparticles and Related Nanomaterials. *Adv. Mater.* **2010**, *22* (11), 1182–1195.

(91) Abadeer, N. S.; Brennan, M. R.; Wilson, W. L.; Murphy, C. J. Distance and Plasmon Wavelength Dependent Fluorescence of Molecules Bound to Silica-Coated Gold Nanorods. *ACS Nano* **2014**, *8* (8), 8392–8406.

(92) Hanske, C.; Sanz-Ortiz, M. N.; Liz-Marzán, L. M. Silica-Coated Plasmonic Metal Nanoparticles in Action. *Adv. Mater.* **2018**, *30*, 1707003.

(93) Wang, F.; Cheng, S.; Bao, Z.; Wang, J. Anisotropic Overgrowth of Metal Heterostructures Induced by a Site-Selective Silica Coating. *Angew. Chem. Int. Ed.* **2013**, *52* (39), 10344–10348.

(94) Chen, L.; Luque, R.; Li, Y. Controllable Design of Tunable Nanostructures inside Metal-Organic Frameworks. *Chem. Soc. Rev.* **2017**, *46*, 4614–4630.

(95) Hinman, J. G.; Turner, J. G.; Hofmann, D. M.; Murphy, C. J. Layer-by-Layer Synthesis of Conformal Metal–Organic Framework Shells on Gold Nanorods. *Chem. Mater.* **2018**, *30* (20), 7255–7261.

(96) Liao, J.; Wang, D.; Liu, A.; Hu, Y.; Li, G. Controlled Stepwise-Synthesis of Core–Shell Au@MIL-100 (Fe) Nanoparticles for Sensitive Surface-Enhanced Raman Scattering Detection. *Analyst* **2015**, *140* (24), 8165–8171.

(97) Fang, L.; Wang, W.; Liu, Y.; Xie, Z.; Chen, L. Zeolitic Imidazole Framework Coated Au Nanorods for Enhanced Photothermal Therapy and Stability. *Dalton Trans.* **2017**, *46* (28), 8933–8937.

(98) Li, Y.; Guo, H.; Yin, Z.; Lyle, K.; Tian, L. Metal–Organic Frameworks for Preserving the Functionality of Plasmonic Nanosensors. *ACS Appl. Mater. Interfaces* **2021**, *13* (4), 5564–5573.

(99) Cai, W.; Wang, J.; Liu, H.; Chen, W.; Wang, J.; Du, L.; Hu, J.; Wu, C. Gold Nanorods@metal-Organic Framework Core-Shell Nanostructure as Contrast Agent for Photoacoustic Imaging and Its Biocompatibility. *J. Alloys Compd.* **2018**, *748*, 193–198.

(100) Zheng, G.; Marchi, S. de; López-Puente, V.; Sentosun, K.; Polavarapu, L.; Pérez-Juste, I.; Hill, E. H.; Bals, S.; Liz-Marzán, L. M.; Pastoriza-Santos, I.; Pérez-Juste, J. Encapsulation of Single Plasmonic Nanoparticles within ZIF-8 and SERS Analysis of the MOF Flexibility. *Small* **2016**, *12* (29), 3935–3943.

(101) Osterrieth, J. W. M.; Wright, D.; Noh, H.; Kung, C.-W.; Vulpe, D.; Li, A.; Park, J. E.; Duyne, R. P. V.; Moghadam, P. Z.; Baumberg, J. J.; Farha, O. K.; Fairen-Jimenez, D. Core–Shell Gold Nanorod@Zirconium-Based Metal–Organic Framework Composites as in Situ Size-Selective Raman Probes. *J. Am. Chem. Soc.* **2019**, *141* (9), 3893–3900.

(102) Zeng, J.-Y.; Zhang, M.-K.; Peng, M.-Y.; Gong, D.; Zhang, X.-Z. Porphyrinic Metal-Organic Frameworks Coated Gold Nanorods as a Versatile Nanoplatform for Combined Photodynamic/Photothermal/Chemotherapy of Tumor. *Adv. Funct. Mater.* **2017**, *28* (8), 1705451.

(103) Li, Y.; Jin, J.; Wang, D.; Lv, J.; Hou, K.; Liu, Y.; Chen, C.; Tang, Z. Coordination-Responsive Drug Release inside Gold Nanorod@metal-Organic Framework Core–Shell Nanostructures for near-Infrared-Induced Synergistic Chemo-Photothermal Therapy. *Nano Res.* **2018**, *11* (6), 3294–3305.

(104) Chen, Q.-Q.; Hou, R.-N.; Zhu, Y.-Z.; Wang, X.-T.; Zhang, H.; Zhang, Y.-J.; Zhang, L.; Tian, Z.-Q.; Li, J.-F. Au@ZIF-8 Core–Shell Nanoparticles as a SERS Substrate for Volatile Organic Compound Gas Detection. *Anal. Chem.* **2021**, *93* (19), 7188–7195.

(105) Tang, L.; Shi, J.; Wu, H.; Zhang, S.; Liu, H.; Zou, H.; Wu, Y.; Zhao, J.; Jiang, Z. In Situ Biosynthesis of Ultrafine Metal Nanoparticles within a Metal-Organic Framework for Efficient Heterogeneous Catalysis. *Nanotechnology* **2017**, *28* (36), 365604.

(106) Zhao, X.; Xu, H.; Wang, X.; Zheng, Z.; Xu, Z.; Ge, J. Monodisperse Metal–Organic Framework Nanospheres with Encapsulated Core–Shell Nanoparticles Pt/Au@Pd@{Co_2(oba)$_4$(3-bpdh)$_2$}4H_2O for the Highly Selective Conversion of CO_2 to CO. *ACS Appl. Mater. Interfaces* **2018**, *10*, 15096–15103.

(107) Hu, H.; Gopinadhan, M.; Osuji, C. O. Directed Self-Assembly of Block Copolymers: A Tutorial Review of Strategies for Enabling Nanotechnology with Soft Matter. *Soft Matter* **2014**, *10* (22), 3867–3889.

(108) Balazs, A. C.; Emrick, T.; Russell, T. P. Nanoparticle Polymer Composites: Where Two Small Worlds Meet. *Science* **2006**, *314* (5802), 1107–1110.

(109) Wolfram, J.; Yang, Y.; Shen, J.; Moten, A.; Chen, C.; Shen, H.; Ferrari, M.; Zhao, Y. The Nano-Plasma Interface: Implications of the Protein Corona. *Colloids Surf. B* **2014**, *124*, 17–24.

(110) Lundqvist, M.; Cedervall, T. Three Decades of Research about the Corona Around Nanoparticles: Lessons Learned and Where to Go Now. *Small* **2020**, *16* (46), 2000892.

(111) Zhang, Y.; Wu, J. L. Y.; Lazarovits, J.; Chan, W. C. W. An Analysis of the Binding Function and Structural Organization of the Protein Corona. *J. Am. Chem. Soc.* **2020**, *142*, 8827–8836.

(112) Boulard, Y.; Marichal, L.; Giraudon--Colas, G.; Cousin, F.; Thill, A.; 0000-0002-1489-0046, J. L. O.; Aude, J.-C.; Pin, S.; Renault, J. P. Protein–Nanoparticle Interactions: What Are the Protein–Corona Thickness and Organization? *Langmuir* **2019**, *35*, 10831–10837.

(113) Martínez-Negro, M.; González-Rubio, G.; Aicart, E.; Landfester, K.; Guerrero-Martínez, A.; Junquera, E. Insights into Colloidal Nanoparticle-Protein Corona Interactions for Nanomedicine Applications. *Adv. Colloid Interface Sci.* **2021**, *289*, 102366.

(114) Dennison, J. M.; Zupancic, J. M.; Lin, W.; Dwyer, J. H.; Murphy, C. J. Protein Adsorption to Charged Gold Nanospheres as a Function of Protein Deformability. *Langmuir* **2017**, *33* (31), 7751–7761.

(115) Lin, W.; Insley, T.; Tuttle, M. D.; Zhu, L.; Berthold, D. A.; Král, P.; Rienstra, C. M.; Murphy, C. J. Control of Protein Orientation on Gold Nanoparticles. *J. Phys. Chem. C* **2015**, *119* (36), 21035–21043.

(116) Yang, J. A.; Lin, W.; Woods, W. S.; George, J. M.; Murphy, C. J. α-Synuclein's Adsorption, Conformation, and Orientation on Cationic Gold Nanoparticle Surfaces Seeds Global Conformation Change. *J. Phys. Chem. B* **2014**, *118* (13), 3559–3571.

(117) Nasir, I.; Lundqvist, M.; Cabaleiro-Lago, C. Size and Surface Chemistry of Nanoparticles Lead to a Variant Behavior in the Unfolding Dynamics of Human Carbonic Anhydrase. *Nanoscale* **2015**, *7* (41), 17504–17515.

(118) Baimanov, D.; Cai, R.; Chen, C. Understanding the Chemical Nature of Nanoparticle–Protein Interactions. *Bioconjugate Chem.* **2019**, *30* (7), 1923–1937.

(119) Yang, J.; Wang, B.; You, Y.; Chang, W.-J.; Tang, K.; Wang, Y.-C.; Zhang, W.; Ding, F.; Gunasekaran, S. Probing the Modulated Formation of Gold Nanoparticles–Beta-Lactoglobulin Corona Complexes and Their Applications. *Nanoscale* **2017**, *9* (45), 17758–17769.

(120) Yong, K. W.; Yuen, D.; Chen, M. Z.; Porter, C. J. H.; Johnston, A. P. R. Pointing in the Right Direction: Controlling the Orientation of Proteins on Nanoparticles Improves Targeting Efficiency. *Nano Lett.* **2019**, *19* (3), 1827–1831.

(121) Kutvonen, A.; Rossi, G.; Puisto, S. R.; Rostedt, N. K. J.; Ala-Nissila, T. Influence of Nanoparticle Size, Loading, and Shape on the Mechanical Properties of Polymer Nanocomposites. *J. Chem. Phys.* **2012**, *137* (21), 214901.

(122) Odegard, G. M.; Clancy, T. C.; Gates, T. S. Modeling of the Mechanical Properties of Nanoparticle/Polymer Composites. *Polymer* **2005**, *46* (2), 553–562.

(123) Thoniyot, P.; Tan, M. J.; Karim, A. A.; Young, D. J.; Loh, X. J. Nanoparticle-Hydrogel Composites: Concept, Design, and Applications of These Promising, Multi-Functional Materials. *Adv. Sci.* **2015**, *2*, 1400010.

(124) Pastoriza-Santos, I.; Kinnear, C.; Perez-Juste, J.; Mulvaney, P.; Liz-Marzan, L. Plasmonic Polymer Nanocomposites. *Nat. Rev. Mater.* **2018**, *3*, 375–391.

(125) Pol, M. H.; Liaghat, G. H. Studies on the Mechanical Properties of Composites Reinforced with Nanoparticles. *Polym. Compos.* **2015**, *38* (1), 205–212.

(126) Zhang, Y. S.; Khademhosseini, A. Advances in Engineering Hydrogels. *Science* **2017**, *356* (6337), eaaf3627.

(127) Sun, J.-Y.; Zhao, X.; Illeperuma, W. R. K.; Chaudhuri, O.; Oh, K. H.; Mooney, D. J.; Vlassak, J. J.; Suo, Z. Highly Stretchable and Tough Hydrogels. *Nature* **2012**, *489* (7414), 133–136.

(128) Chen, Q.; Chen, H.; Zhu, L.; Zheng, J. Fundamentals of Double Network Hydrogels. *J. Mater. Chem. B* **2015**, *3* (18), 3654–3676.

(129) Gong, J. P. Why Are Double Network Hydrogels so Tough? *Soft Matter* **2010**, *6* (12), 2583–2588.

(130) Talebian, S.; Mehrali, M.; Taebnia, N.; Pennisi, C. P.; Kadumudi, F. B.; Foroughi, J.; Hasany, M.; Nikkhah, M.; Akbari, M.; Orive, G.; Dolatshahi-Pirouz, A. Self-Healing Hydrogels: The Next Paradigm Shift in Tissue Engineering? *Adv. Sci.* **2019**, *6*, 1801664.

(131) Mehrali, M.; Thakur, A.; Pennisi, C. P.; Talebian, S.; Arpanaei, A.; Nikkhah, M.; Dolatshahi-Pirouz, A. Nanoreinforced Hydrogels for Tissue Engineering: Biomaterials That Are Compatible with Load-Bearing and Electroactive Tissues. *Adv. Mater.* **2016**, *29* (8), 1603612.

(132) El-Sherbiny, I. M.; Yacoub, M. H. Hydrogel Scaffolds for Tissue Engineering: Progress and Challenges. *Glob. Cardiol. Sci. Pract.* **2013**, *38*, 317–342.

(133) Gilshteyn, E. P.; Lin, S.; Kondrashov, V. A.; Kopylova, D. S.; Tsapenko, A. P.; Anisimov, A. S.; Hart, J. A.; Zhao, X.; Nasibulin, A. G. A One-Step Method of Hydrogel Modification by Single-Walled Carbon Nanotubes for Highly Stretchable and Transparent Electronics. *ACS Appl. Mater. Interfaces* **2018**, *10* (33), 28069–28075.

(134) Rong, Q.; Lei, W.; Liu, M. Conductive Hydrogels as Smart Materials for Flexible Electronic Devices. *Chem. Eur. J.* **2018**, *24* (64), 16930–16943.

(135) Sershen, S. R.; Mensing, G. A.; Ng, M.; Halas, N. J.; Beebe, D. J.; West, J. L. Independent Optical Control of Microfluidic Valves Formed from Optomechanically Responsive Nanocomposite Hydrogels. *Adv. Mater.* **2005**, *17* (11), 1366–1368.

(136) Murphy, C. J.; Orendorff, C. J. Alignment of Gold Nanorods in Polymer Composites and on Polymer Surfaces. *Adv. Mater.* **2005**, *17* (18), 2173–2177.

(137) Pérez-Juste, J.; Rodríguez-González, B.; Mulvaney, P.; Liz-Marzán, L. M. Optical Control and Patterning of Gold-Nanorod-Poly(Vinyl Alcohol) Nanocomposite Films. *Adv. Funct. Mater.* **2005**, *15* (7), 1065–1071.

(138) Lio, G. E.; Palermo, G.; Caputo, R.; Luca, A. D. Opto-Mechanical Control of Flexible Plasmonic Materials. *J. Appl. Phys.* **2019**, *125*, 082533.

(139) Pletsch, H.; Tebbe, M.; Dulle, M.; Förster, B.; Fery, A.; Förster, S.; Greiner, A.; Agarwal, S. Reversible Gold Nanorod Alignment in Mechano-Responsive Elastomers. *Polymer* **2015**, *66* (C), 167–172.

(140) Dai, L.; Lu, X.; Song, L.; Huang, Y.; Liu, B.; Zhang, L.; Zhang, J.; Wu, S.; Chen, T. Macroscopic-Oriented Gold Nanorods in Polyvinyl Alcohol Films for Polarization-Dependent Multicolor Displays. *Adv. Mater. Interfaces* **2018**, *5* (11), 1800026.

(141) Keshavarz, M.; Moloudi, K.; Paydar, R.; Abed, Z.; Beik, J.; Ghaznavi, H.; Shakeri-Zadeh, A. Alginate Hydrogel Co-Loaded with Cisplatin and Gold Nanoparticles for Computed Tomography Image-Guided Chemotherapy. *J. Biomater. Appl.* **2018**, *33* (2), 161–169.

(142) Baei, P.; Jalili-Firoozinezhad, S.; Rajabi-Zeleti, S.; Tafazzoli-Shadpour, M.; Baharvand, H.; Aghdami, N. Electrically Conductive Gold Nanoparticle-Chitosan Thermosensitive Hydrogels for Cardiac Tissue Engineering. *Mater. Sci. Eng. C* **2016**, *63*, 131–141.

CHAPTER 2: LAYER-BY-LAYER SYNTHESIS OF CONFORMAL HKUST-1 SHELLS ON GOLD NANORODS [1]

2.1 Abstract

Because of their possible use in a number of applications such as sensing and catalysis, hybrid materials of metal−organic frameworks (MOFs) with plasmonic nanoparticles have attracted the attention of many researchers. While there have been reports of the synthesis of MOF shells on colloidal metallic nanoparticles, they often provide little control over the thickness and morphology of the MOF shell. This report presents a layer-by-layer technique for synthesizing conformal shells of the MOF HKUST-1 on gold nanorods. The method described deposits the components of the MOF in a truly layer-by-layer fashion, which allows for sub-nanometer control over shell thickness. To synthesize conformal MOF shells, it is crucial to control the surface chemistry of the gold nanorods. By using the conjugate base of the organic linker, the surface charge could be controlled during synthesis, helping prevent nanorod aggregation.

2.2 Introduction

There has been a recent surge in reports of materials that incorporate both metal-organic frameworks (MOFs) and nanoparticles. Interest in MOFs, which consist of metal-containing hubs linked together by organic ligands, often stems from their porous structures that lend themselves to a wide variety of applications including gas storage, separations, and catalysis, among others.[1] While progress has been made towards combining MOFs with a variety of nanomaterials, plasmonic nanoparticles like gold nanorods (AuNRs) are particularly interesting because of their

[1] Adapted and reprinted with permission from Hinman J. G.; Turner, J. G.; Hofmann, D. M.; Murphy, C. J. Layer-by-Layer Synthesis of Conformal Metal-Organic Framework Shells on Gold Nanorods. *Chem. Mater.* **2018**, 30 (20), 7255-7261. Copyright 2018 American Chemical Society

distinct optical properties.[2,3] Hybrid materials of plasmonic nanoparticles and MOFs are promising for several applications, including sensing and catalysis.[4–6] Using plasmonic heating, it may be possible to use light to control the adsorption and desorption of molecules from the pores of hybrid materials of plasmonic nanoparticles and MOFs.[7] Most reported syntheses for MOF shells on metal nanoparticles do not allow for precise control of the shell's morphology, but recently layer-by-layer (LbL) methods have emerged as an alternative that can provide greater control over shell thickness.[8–14] Table 2.1 summarizes the current scope of what has been done in the area of MOF encapsulated metal nanoparticles. Compared to other methods of thin film deposition, LbL assembly often provides superior control over the film thickness.[15,16] Limitations of previously reported LbL MOF shell synthesis include poor control over the morphology of the resulting shells and nanoparticle aggregation, which is often exacerbated by the number layers necessary to form shells of a given thickness. Here, we report the LbL synthesis of MOF shells on AuNRs and we describe improvements to LbL techniques for deposition of MOFs on nanoparticles that allow precise control over the thickness of conformal MOF shells with improved colloidal stability.

Table 2.1: Summary of reported MOF coated colloidal NPs.

Core NP	Surface Chemistry	MOF	MOF shell Thickness (nm)	Ref.
AuNRs, 23x85 nm	11-mercaptoundecanoic acid	HKUST-1	2, 3, 4, 5, 6	This work
Pt-Cu (Octahedron, Flower), 43 nm	Polyvinylpyrrolidone	HKUST-1	4, 11, 24	17
(AuNP - 13, 100 nm, AuNR - 12x15 nm, Pd - 20nm)@Cu2O	Polyvinylpyrrolidone	HKUST-1	50, 75, 100, 125	18
AgNPs, 8, 20, 40 nm	Polyvinylpyrrolidone	IRMOF-3	25, 100, 175	19
PdNPs, 35 nm	Polyvinylpyrrolidone	IRMOF-3	30 - 145	20
AuNPs, 60 nm	Mercaptoacetic acid	MIL-100	5, 20, 35, 50	12
AuNPs, 30 nm	Inositol hexaphosphate	MIL-101	2	14
AuNPs, 30, 50, 60 nm	Polyvinylpyrrolidone	MOF-5	3, 25, 69	21
AuNRs, 8x30 nm	Lipoic acid	Porphyrin MOF	8, 15	8
Ag cubes, 100 nm	Polyvinylpyrrolidone	Re_n-MOF	16, 33	22
Pd cubes, 30 nm; Au cubes, 50 nm	CTAB	ZIF-8	60 - 150	10
AuNRs, 30x60 nm	PEG-SH	$[Al(OH)(1,4\text{-ndc})]_n$	75	9

2.3 Results and Discussion

The MOF we chose to deposit on AuNRs was HKUST-1 (copper(II) benzene-1,3,5-tricarboxylate), a well-studied MOF that has been deposited in layers on a variety of surfaces.[23–25] In our method (Scheme 2.1) cetyltrimethylammonium bromide (CTAB)-capped AuNRs were functionalized with 11-mercaptoundecanoic acid (MUA), then coated with HKUST-1 by alternating additions of copper(II) acetate and the tetramethylammonium salt of 1,3,5-benzenetricarboxylate (TMA-BTC). Between additions of the HKUST-1 precursors, the AuNRs were purified by centrifugation. The resulting shells, shown in Figure 2.1, were mostly smooth and uniform.

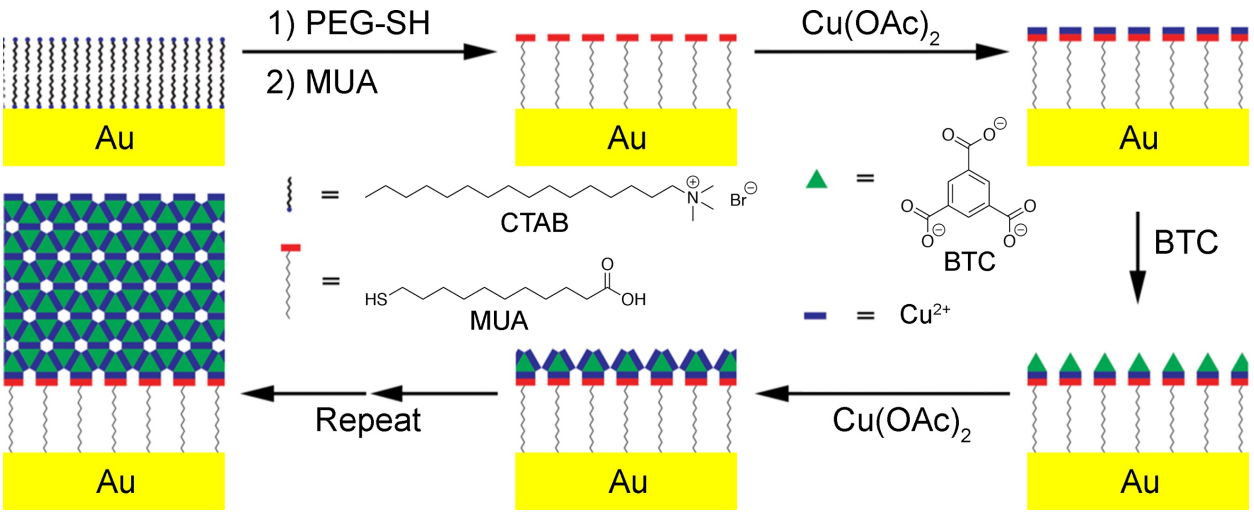

Scheme 2.1: Synthetic conditions used for LbL coating of AuNRs with HKUST-1.

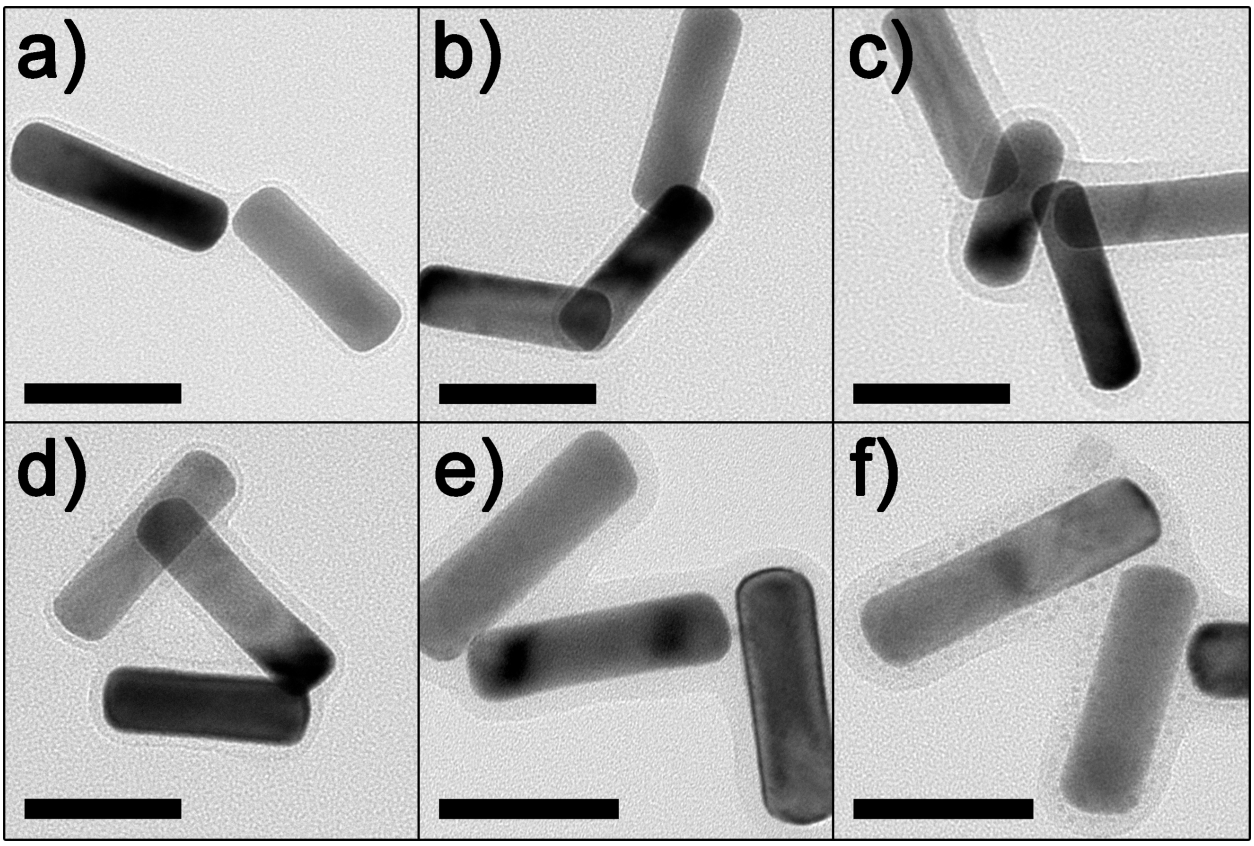

Figure 2.1: Transmission electron microscopy (TEM) images of HKUST-1 coated AuNRs after (a) 4, (b) 8, (c) 12, (d) 16, (e) 20, and (f) 24 layers. Scale bars are 50 nm.

To verify that the AuNRs were coated with HKUST-1, we characterized them by energy dispersive X-ray spectroscopy in scanning transmission electron microscopy (STEM-EDS), powder X-ray diffraction, and attenuated total reflectance Fourier transform infrared spectroscopy (ATR-FTIR). Line scans for copper and gold using STEM-EDS (Figure 2.2a) on AuNRs after depositing 18 layers were consistent with a thin, copper-containing shell around a gold core. Powder XRD of HKUST-1 coated AuNRs after 30 layers (Figure 2.2b) indicated the presence of HKUST-1 in addition to gold. While the broad peak near 8˚ is indicative of amorphous material, small peaks matching the theoretical pattern for HKUST-1 are also present.[26] Similarly, the ATR-FTIR spectrum of HKUST-1 coated AuNRs after 30 layers closely matched that for free HKUST-1.

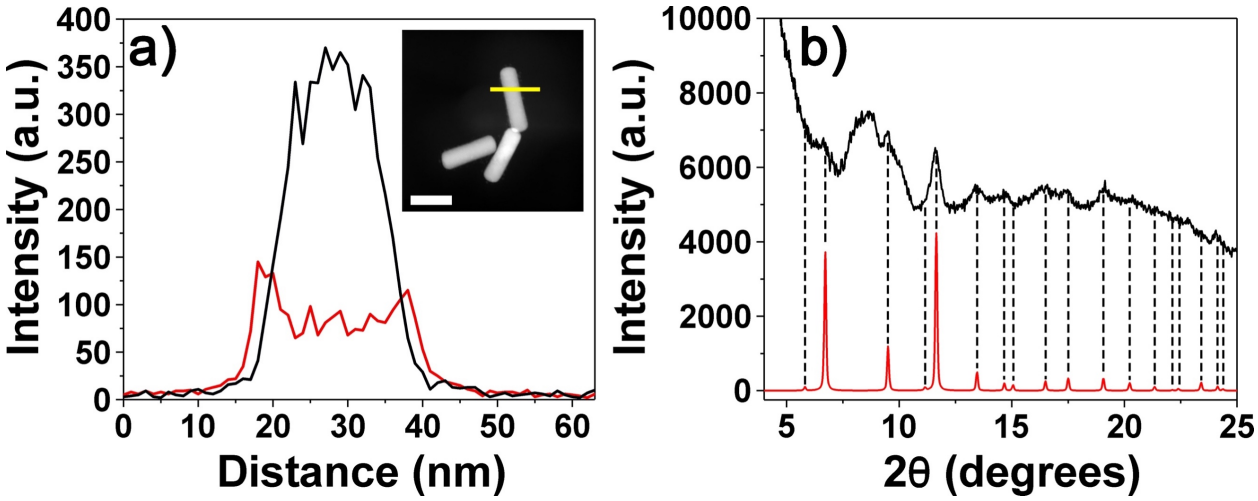

Figure 2.2: (a) STEM-EDS lines scans for copper (red) and gold (black) were taken along the yellow line in the inset dark-field STEM image of HKUST-1 coated AuNRs. Scale bar is 50 nm. (b) The experimentally measured powder XRD pattern for HKUST-1 coated AuNRs is shown in black with the theoretical powder XRD pattern for free HKUST-1 in red. The broad peak near 8 degrees is likely due to amorphous MOF.

We were able to deposit conformal, porous HKUST-1 shells on AuNRs with sub-nanometer control over their thickness. TEM analysis of the HKUST-1 shells revealed that the thickness of the shells increased linearly with the number of layers added (Figure 2.3a). From the slope of the regression line in Figure 2.3a, shell thickness was found to increase by 0.178 ± 0.014 nm per layer and the intercept of the regression line, 1.5 ± 0.2 nm, agrees well with the experimental measurements of the thickness of SAMs of MUA on gold.[27] We collected N_2 adsorption and desorption isotherms for HKUST-1 coated AuNRs (Figure 2.3b) and calculated the BET surface area. After 30 layers of HKUST-1 shell synthesis, the BET surface area was measured to be 63 $m^2 \cdot g^{-1}$ which is considerably less than the 850-1400 $m^2 \cdot g^{-1}$ that are typically reported for free HKUST-1.[28–30] Our relatively small BET surface area could indicate that the shells are amorphous

and therefore are not as porous as typical sample of HKUST-1.[17] However, the majority of the mass of HKUST-1 coated nanorods is in their gold cores. Correcting for the contributions of gold to the mass of the HKUST-1 coated nanorods gives a surface area of 900 $m^2 \bullet g^{-1}$, which is comparable to experimental measurements of the surface area of free HKUST-1 (See Materials and Methods section for details). While some reports of MOF-coated nanoparticles show large surface areas without the correction, we suggest that such measurements may reflect the presence of free MOF nanoparticles.

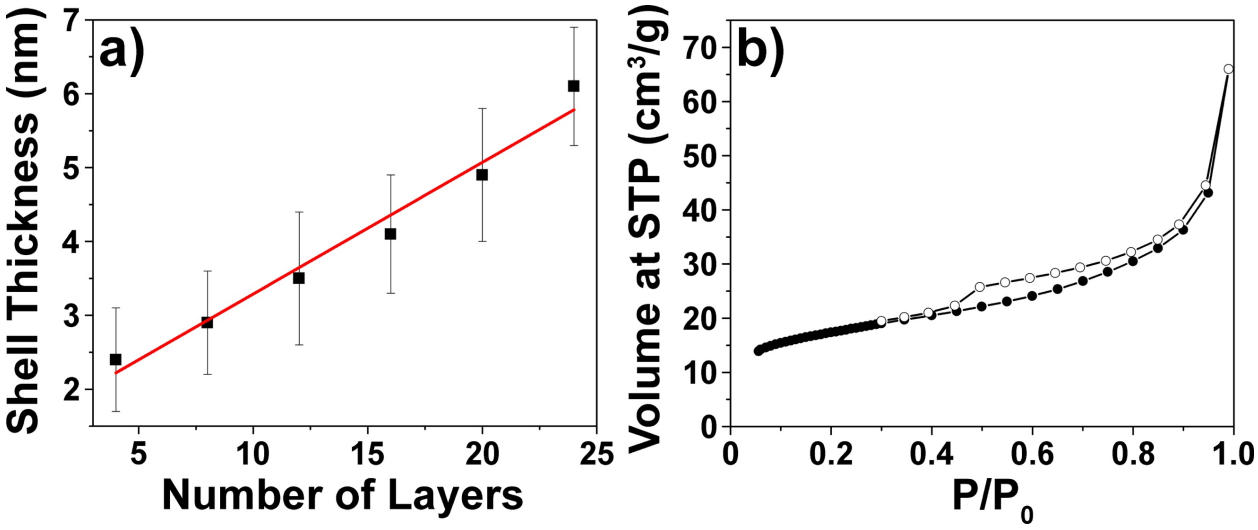

Figure 2.3: (a) HKUST-1 shell thickness from TEM analysis plotted against the number of layers of deposited. The red line represents the weighted line of regression. Error bars show standard deviation. (b) N_2 adsorption (closed circles) and desorption (open circles) isotherms for AuNRs after 30 layers of HKUST-1 shell synthesis.

We discovered certain key parameters in the synthesis that enabled reproducible LbL growth on AuNRs. Adding TMA-BTC rather than H_3BTC reduced aggregation during LbL synthesis. Aggregation is a significant challenge for LbL syntheses of MOF shells on

nanoparticles. Over the potentially large number of layers deposited, even relatively small amounts of aggregation at early stages lead to aggregation difficulties at later stages. Often in the synthesis of LbL MOF films, organic linkers are added as carboxylic acids. When the surfaces of MOF coated nanoparticles are terminated in protonated carboxylic acids, their surfaces are nearly charge neutral, which can lead to aggregation. Using the conjugate base of the linker instead, with a TMA counterion, gives the surface a negative charge, improving MOF coated nanoparticles' colloidal stability. Measurements of the ζ-potential of HKUST-1 coated AuNRs after each layer for 24 layers of LbL synthesis show that following the addition of TMA-BTC, HKUST-1 coated AuNRs have a negative surface charge (Figure 2.4b). Relatively little broadening of the longitudinal localized surface plasmon resonance (LSPR) in the UV-Vis spectra of HKUST-1 coated AuNRs (Figure 2.4d) after 24 layers of LbL synthesis connotes only a small degree of aggregation. In contrast, after adding H_3BTC as the organic linker the measured ζ-potentials for HKUST-1 coated AuNRs are close to neutral (Figure 2.4a). Increased broadening of the longitudinal LSPR (Figure 2.4c) illustrates the importance of electrostatic stabilization to prevent the aggregation of HKUST-1 coated AuNRs during LbL synthesis.

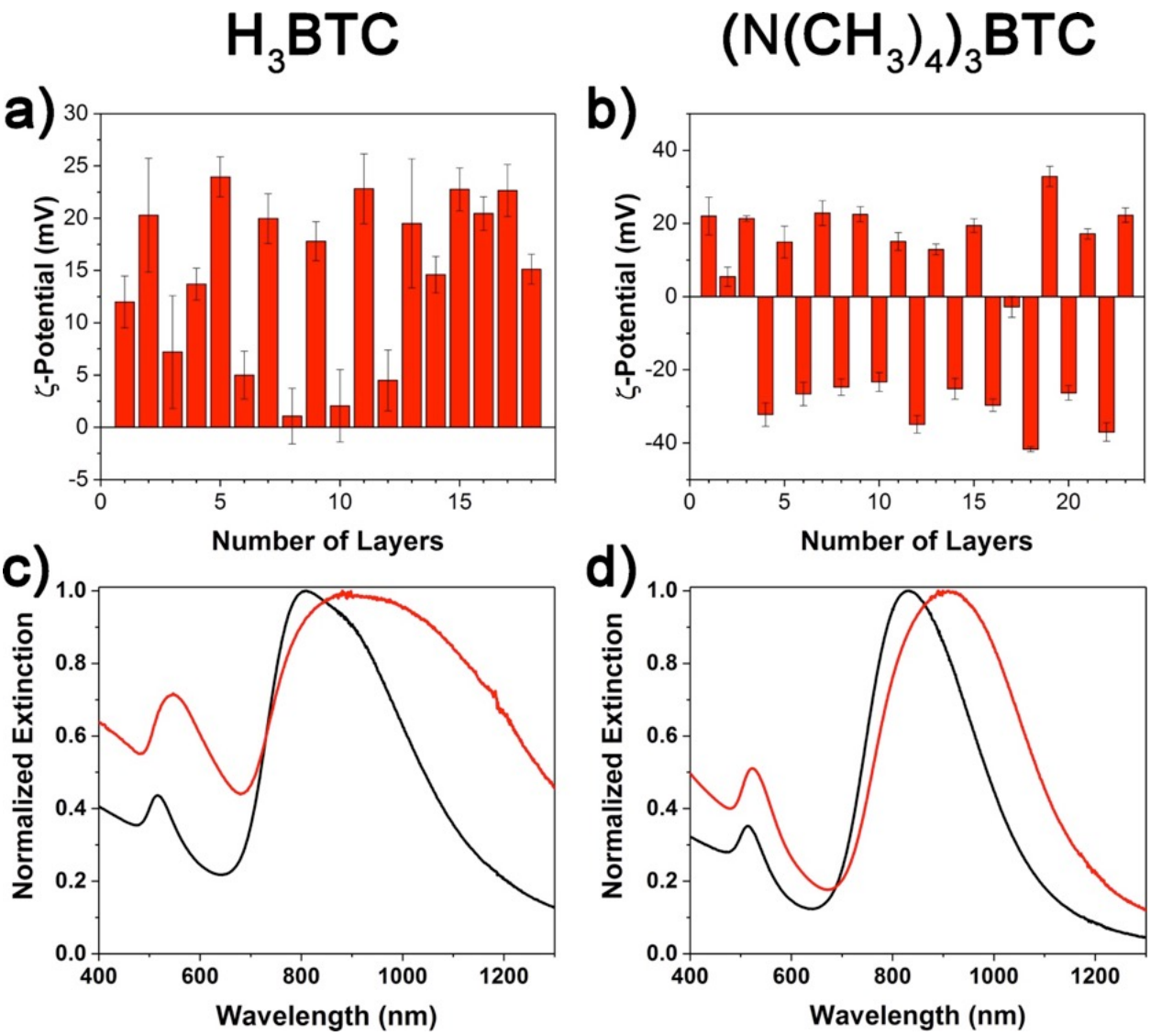

Figure 2.4: ζ-potentials of HKUST-1 coated AuNRs are plotted against the number of layers added for syntheses using (a) H_3BTC and (b) $(N(CH_3)_4)_3BTC$. Odd layers correspond to $Cu(OAc)_2$ additions and even to BTC additions. UV-Vis spectra after 1 (black) and 18 (red) layers are shown for AuNRs coated with HKUST-1 using (c) H_3BTC and (d) $(N(CH_3)_4)_3BTC$.

Aggregation can also be prevented by using slower centrifugation speeds during cleaning and purification. Although excess $Cu(OAc)_2$ and BTC were removed by three rounds of

centrifugation between layers, some free HKUST-1 particles still formed. The presence of free MOF nanoparticles often induces particle aggregation. However, when HKUST-1 coated AuNRs were centrifuged at speeds less than 2000 rcf we found that it is possible to separate the AuNRs from free MOF nanoparticles, as shown in Figure 2.5.

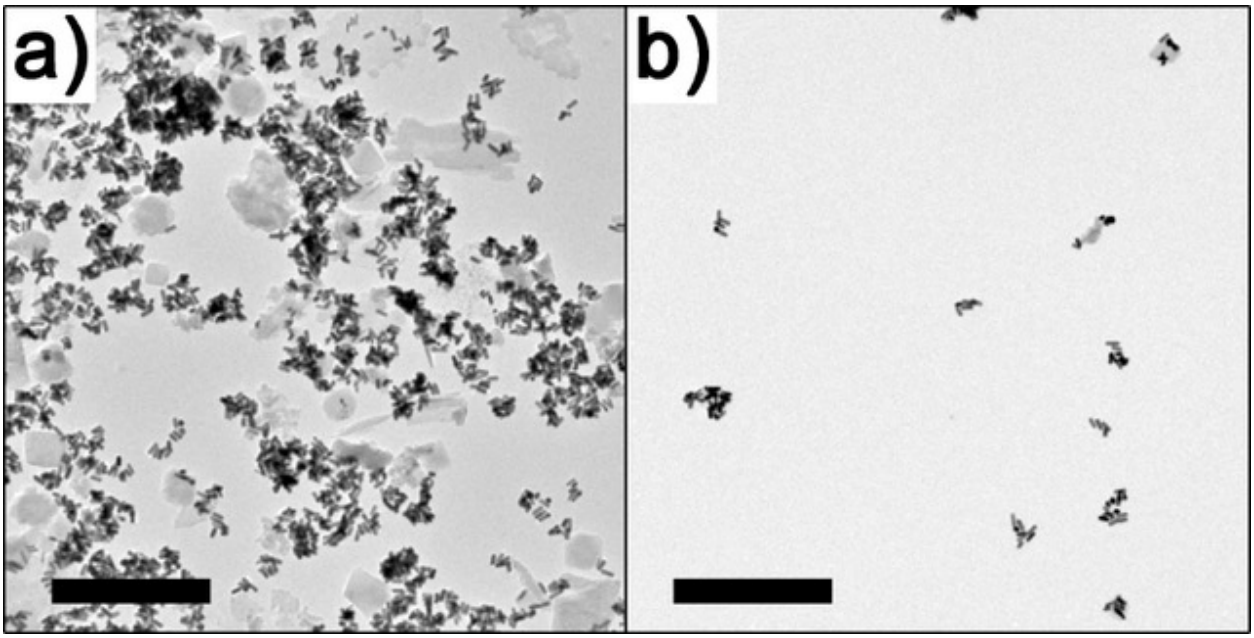

Figure 2.5: TEM images of the comparison between the LbL synthesis with (a) fast centrifugation (8000 rcf) and (b) slow centrifugation (2000 rcf or less), showing the presence of more free MOF particles when using fast centrifugation. Scale bars are 500 nm.

Surface functionalization of the AuNRs was also critical to ensure controllable deposition of conformal HKUST-1 shells. MOF thin films prepared using LbL techniques have been reported on a number of different surfaces including silica, self-assembled monolayers of alkanethiols on gold, and polymer coated gold.[13,25,31] However, we observed pronounced differences in the resulting MOFs on AuNRs depending on the surface chemistry. Following Shekhah and

coworker's success growing both HKUST-1 and ZIF-8 on silica, we prepared silica-coated AuNRs using a previously published procedure as a substrate for LbL HKUST-1 synthesis.[25,32] Although HKUST-1 was deposited on the silica surface, TEM analysis after 10 layers revealed island growth rather than thin film growth (Figure 2.6a). In contrast, on MUA-functionalized AuNRs HKUST-1 was deposited as a thin, conformal shell (Figure 2.6b). Our same procedure was also tried using polyelectrolyte wrapped gold nanorods. Polyelectrolyte wrapping was done according to previously published methods.[15] With the negatively charged poly(acrylic acid) sodium salt (PAA) surface, we did not observe any MOF growth as evident by TEM analysis The effect of nanoparticle surface functionalization may explain, in part, differences in the morphology of the LbL MOF shells previously reported in the literature. MOF shells on nanoparticles functionalized with carboxylic acid terminated alkanethiols like mercaptoacetic acid often appear smoother and more uniform than those on nanoparticles with surface coatings like polyvinylpyrrolidone, that are less likely to coordinate as strongly to the metal ions of the MOF.[12,13]

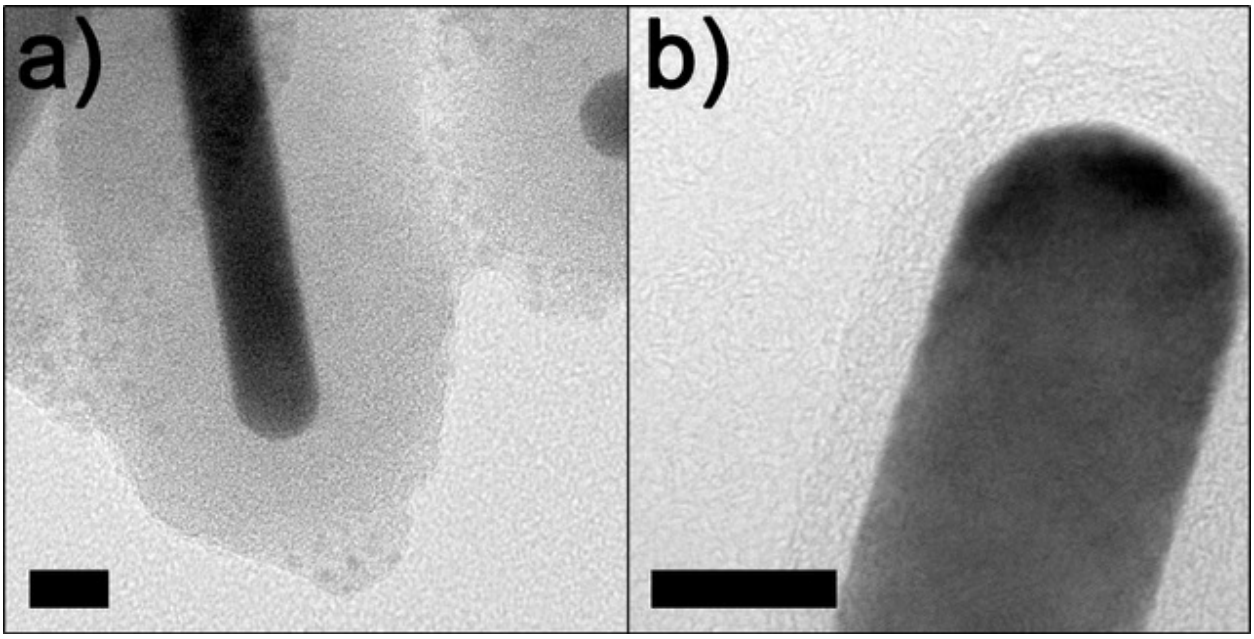

Figure 2.6: TEM images illustrating the different growth of HKUST-1 on (a) the surface of silica coated gold nanorods and (b) the surface of MUA functionalized gold nanorods. Scale bars are 10 nm.

2.4 Conclusions

In conclusion, we have presented improved methodology for the synthesis of conformal, controllable MOF shells on AuNRs. Our protocols allow for precise control over the thickness of an HKUST-1 shell on gold nanorods. We demonstrated the importance of choosing the appropriate surface functionalization on the AuNRs to ensure the growth of conformal and uniform MOF shells. Aggregation can be minimized by using the conjugate base of the organic linker BTC to improve the electrostatic stability of the MOF coated AuNRs and by separating free MOF nanoparticles using slow centrifugation speeds.

2.5 Materials and Methods

2.5.1 Materials and Instrumentation

Chloroauric acid ($HAuCl_4 \cdot 3H_2O$), 99.9%; hydroquinone, 99%; cetyltrimethylammonium bromide (CTAB) 99%; silver nitrate (AgNO3), 99%; sodium borohydride (99%). Copper(II) acetate ($Cu(OAc)_2$), 98%; 1,3,5-benzenetricarboxylic acid (BTC), 95%; tetramethylammonium hydroxide solution, 1.0 M electrochemical grade; and 11-mercaptoundecanoic acid (MUA), 95% were purchased from Sigma-Aldrich. Thiolated poly(ethylene glycol) (PEG-SH) 5000 M.W. was purchased from Nanocs. ACS reagent grade sodium hydroxide was purchased from Fisher Scientific. Ethanol, 200 proof, was purchased from Decon Labs Inc., and used without purification. Deionized water was purified using a Barnstead Nanopure II purification system.

UV-Vis extinction spectra were measured using a Cary 5000 UV-vis-NIR spectrophotometer. ξ-potentials were measured using a Brookhaven ZetaPals and/or a Malvern Zetasizer Nano ZS. Powder X-ray diffraction (XRD) was measured using a Bruker D8 Venture Duo. Nitrogen adsorption measurements were carried out on a Micromeritics 3 Flex Surface Area and Pore Analyzer. ATR-FTIR measurements were collected on a Nicolet Nexus 670 spectrometer equipped with a germanium crystal plate. Transmission electron microscopy was carried out on a JEOL 2010 LaB_6 or 2100 Cryo LaB_6 operated at 200 kV. STEM-EDS element line scans were measured on a JEOL 2010F. All sizing analysis was done using ImageJ, for nanorod sizing a minimum of 300 nanorods were measured, for MOF shell sizing a minimum of 50 shells were measured for each sample.

2.5.2 Synthesis of Gold Nanorods

To synthesize gold nanorods, we adapted the methods described by Vigderman and Zubarev.[33] For CTAB-capped gold seeds, a seed solution was prepared by adding 500 μL of 0.010 M chloroauric acid to 9.5 mL 0.10 M CTAB. While stirring the seed solution rapidly, 460 μL of freshly prepared, ice-cold 0.10 M sodium borohydride in 0.010 M NaOH was quickly added. The seed solution color changed to dark brown immediately following the addition of $NaBH_4$. The seeds were aged for 1 hour before use. To prepare large batches of nanorods, more seed solution is required. Replicate batches of 10 mL seed solutions were prepared simultaneously to yield the required amount of seed solution.

On a 1 L scale, the AuNR growth solution was prepared by adding 1.30 mL of 0.10 M AgNO3 to 950 mL of 0.10 M CTAB followed by 50 mL of 0.010 M HAuCl4 with stirring. Then, 50 mL of 0.10 M hydroquinone was added and the solution was stirred until it turned colorless, at which time 16 mL of CTAB-capped gold seeds were added. The growth solution was stored overnight at 27 °C. The nanorods were purified by centrifugation at 8000 rcf for 20 minutes. After discarding the supernatant, the AuNRs were redispersed in nanopure water and stored at room temperature until use.

2.5.3 Nanorod Surface Functionalization

CTAB-capped nanorods were further purified by an additional round of centrifugation at 8000 rcf. For ligand exchange, the supernatant was discarded and the AuNRs were dispersed in nanopure water to a concentration of 1 nM in gold nanorods (extinction coefficient 1.6×10^{10} $M^{-1}cm^{-1}$).[34] On a 40 mL scale, CTAB was exchanged for PEG-SH (5000 M.W.) by adding 1 mL of 50 mg/mL PEG-SH to the 40 mL solution of 1 nM nanorods. The solution was gently shaken

overnight. To purify the nanorods, they were centrifuged at 8000 rcf for 30 minutes, the supernatant was discarded, and the pellet was dispersed in 40 mL water. The AuNRs were centrifuged a second time; however, the pellet was only dispersed in 20 mL water. Then, 2 mL of 0.1 M NaOH was added to the nanorods, along with 4 mL of 20 mM ethanolic MUA before dilution to 40 mL with water. The gold nanorods were shaken gently overnight. To purify the nanorods, they were centrifuged at 8000 rcf for 30 minutes, the supernatant was discarded and the pellet was dispersed in 2 mL of 0.1 M NaOH and then dispersed to a total volume of 40 mL. TEM images (Figure 2.7a and b), UV-vis (Figure 2.7c) spectra of the gold nanorods before and after functionalization, and the corresponding ζ-potentials (Figure 2.7d) for the nanorods with different surface ligands is also shown.

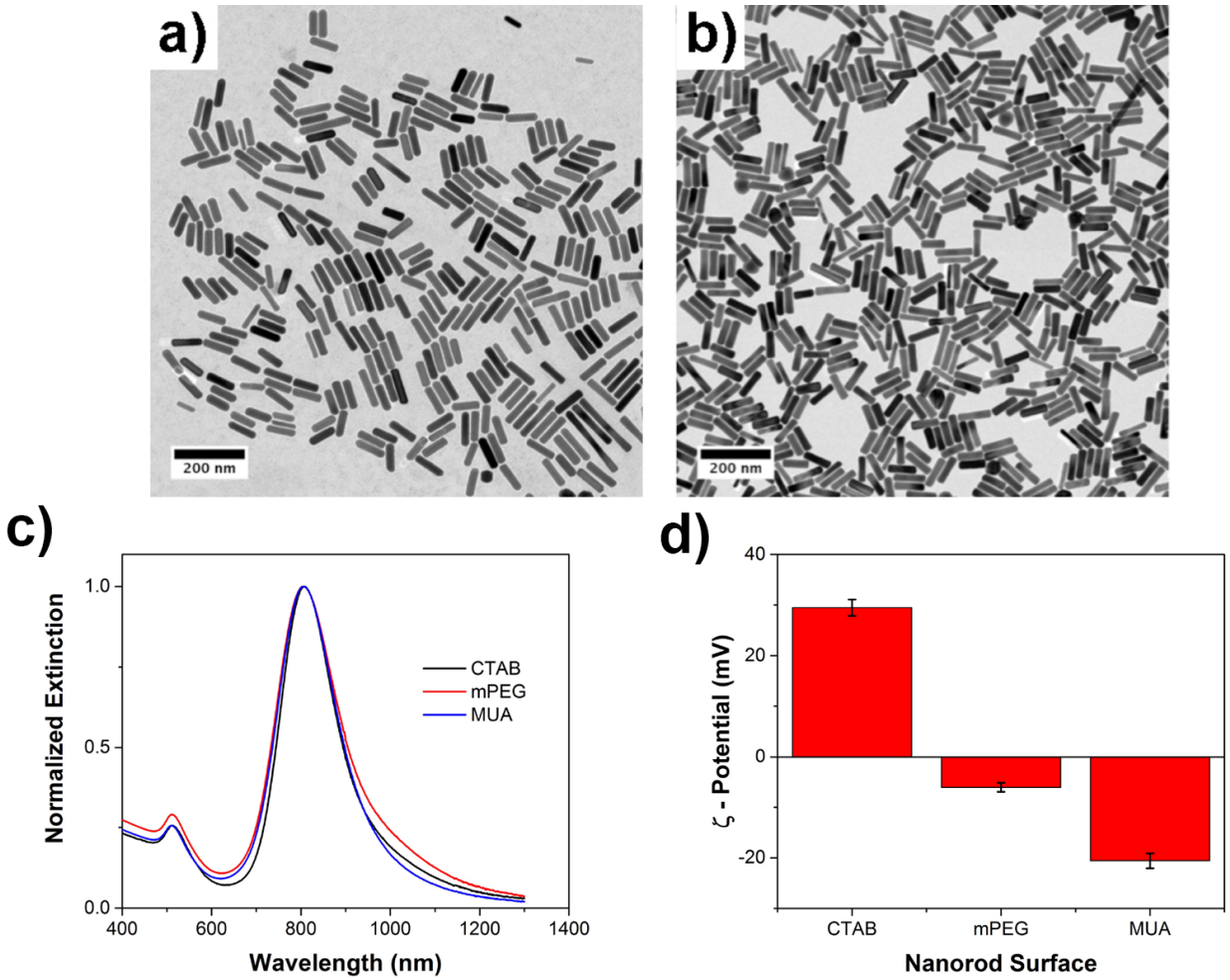

Figure 2.7: Characterization date of AuNRs and the surface functionalization process. TEM images of (a) as synthesized AuNRs and (b) AuNRs after MUA surface functionalization. (c) UV-vis spectra of AuNR solutions with different surface ligands. (d) ζ-potential of AuNR solutions with various surface ligands.

2.5.4 Tetramethylammonium 1,3,5-benzenetricarboxylate Salt Preparation

Tetramethylammonium 1,3,5-benzenetricarboxylate salt (TMA-BTC) was prepared by adding stoichiometric amounts of BTC to 1.0 M tetramethylammonium hydroxide. (**NOTE**: **Caution** should be taken when working with concentrated solutions of tetramethylammonium

hydroxide due to its high toxicity, especially through skin contact). After dissolving BTC, the solution was stirred for one hour. Once dissolved, the stir bar was removed and TMA-BTC was recovered by lyophilizing the solution, after which a white powder remained. The powder was analyzed by ATR-FTIR (see Figure 2.8). Individual peak designations were confirmed from previously reported results.[35,36]

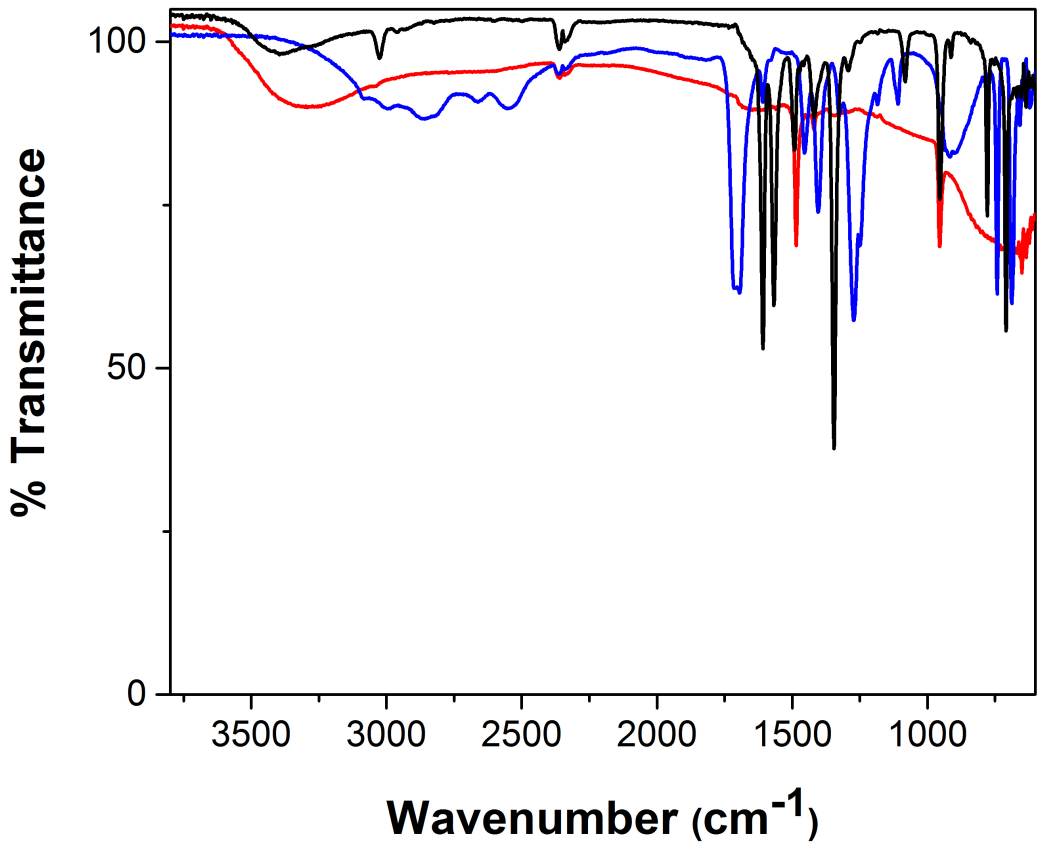

Figure 2.8: ATR-FTIR of the synthesized TMA-BTC salt (black) overlaid with trimesic acid (blue) and tetramethylammonium hydroxide (red).Peak assignments for TMA-BTC are: 3388 cm^{-1}(OH stretch), 3026 cm^{-1}(CH stretch), 1608 cm^{-1}(OH bend), 1567 cm^{-1}(CC stretch), 1490 cm^{-1}(CH3 bend), 1417 cm^{-1}(CH bend), 1344 cm^{-1}(CO stretch), 951 cm^{-1}(CN stretch). Peaks at 2363 cm^{-1} were due to CO2.

2.5.5 Layer-by-Layer HKUST-1 Deposition

Our method for layer-by-layer synthesis of MOF shells on gold nanorods was adapted and modified from previously reported procedures for layer-by-layer MOF deposition.[12,13,25,31] On a 1 mL scale, 1 mL aliquots of 1 nM MUA-functionalized nanorods were dispensed into the desired number of microcentrifuge tubes (i.e. to deposit 20 layers, 20 microcentrifuge tubes were used). Prior to adding the first layer in the MOF shell synthesis the MUA nanorods were centrifuged at 8000 rcf for 30 minutes, the supernatants were discarded, the pellets were dispersed in 1 mL of water. Centrifugation was repeated a second time after which the pellets were dispersed in 0.5 mL of ethanol. Then 0.5 mL of 20 mM copper(II) acetate was added, the tubes were inverted to mix, and incubated for 10 minutes. After the elapsed 10 minutes, the tubes were centrifuged at 2000 rcf for 30 min (10 min for all additional copper layers) to remove excess copper(II) acetate. For each copper layer, there were two washes. For the first wash, the pellets were dispersed in ethanol and centrifuged at 2000 rcf for 30 minutes (10 minutes for all additional copper layers). The pellets were each dispersed in 1 mL ethanol and then centrifuged at 500 rcf for 45 min (30 minutes for all additional copper layers) for the second wash. After the third round of centrifugation, the supernatants were discarded and the pellets were dispersed in 0.5 mL ethanol. Then 0.5 mL of 20 mM TMA-BTC dissolved in ethanol was added, the contents were mixed, briefly sonicated, and then allowed to stand for 10 minutes. Excess TMA-BTC salt was removed by three rounds of centrifugation at 2000 rcf for 10 minutes each, dispersing the pellet in 1 mL of ethanol after each. After the third round of centrifugation, the AuNRs were each dispersed in 0.5 mL of ethanol, such that the next copper addition could be started by adding 0.5 mL of 20 mM copper(II) acetate in ethanol. These steps were repeated to produce the desired number of layers. After each layer, one of the microfuge tubes containing 1 mL of 1 nM HKUST-1 coated AuNRs was saved for analysis.

The concentrations reported were a result of optimizing the synthetic parameters. Concentrations were screened between 1-100 mM for each precursor, 20 mM was chosen as it produced uniform HKUST-1 shells without making large HKUST-1 particles. The UV-vis spectra for each layer can in shown in Figure 2.9.

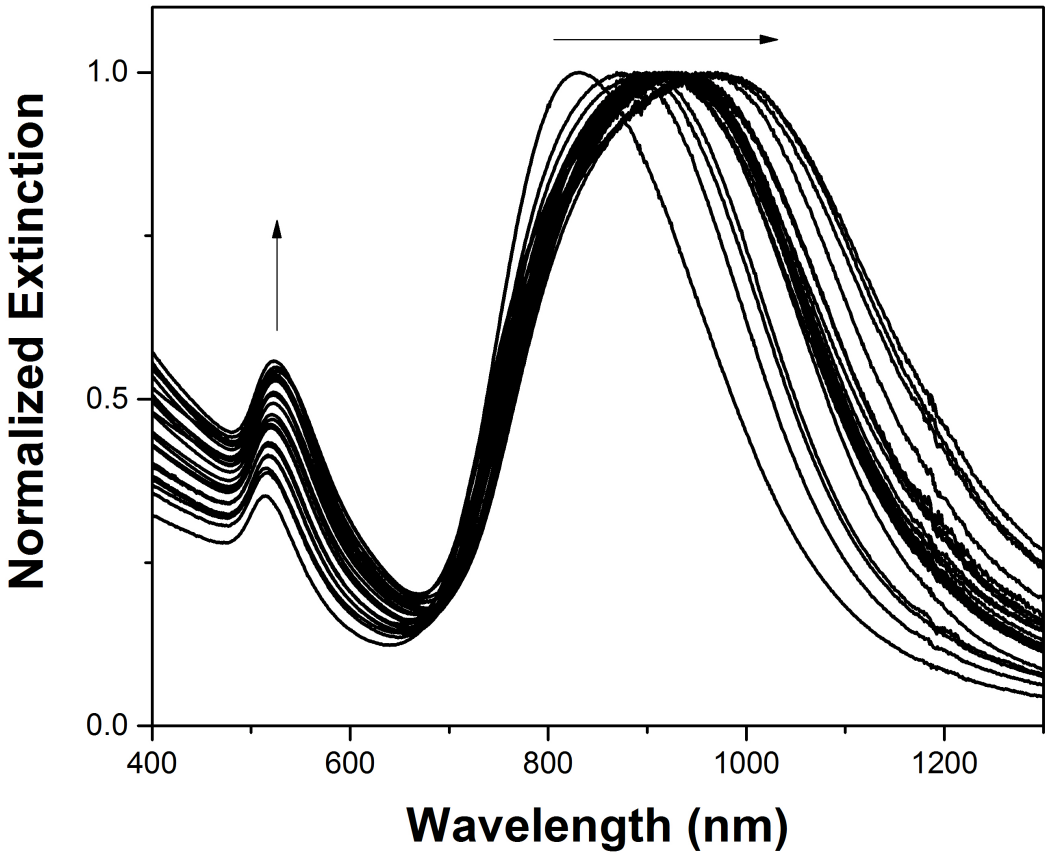

Figure 2.9: Normalized UV-vis of AuNR solutions with HKUST-1 shells for layers 1-24. As layers are added, the transverse plasmon intensity increases, while the longitudinal plasmon red shifts and broadens (as indicated by the arrows).

2.5.6 Scale-Up Method for Layer-by-Layer Process

To scale up the synthesis, 18 mL of 20 nM MUA-functionalized AuNRs were separated into 1 mL aliquots in microcentrifuge tubes. To remove excess MUA, the AuNRs were centrifuged at 8000 rcf for 30 minutes, the supernatants were discarded, and the pellets were dispersed in 1 mL of water each. Centrifugation was repeated a second time but after removing the supernatant the pellets were dispersed in 0.5 mL of ethanol. For the copper layers, 0.5 mL of 50 mM copper(II) acetate in ethanol was added, the contents of the tubes were mixed and sonicated, and then allowed to stand for 10 minutes. Excess copper(II) acetate was removed via centrifugation at 8000 rcf for 30 min (2000 rcf for 15 min for all additional copper layers). The supernatants were discarded and each pellet was dispersed in 1 mL ethanol. This was followed by a second round of centrifugation at 2000 rcf for 30 min (2000 rcf for 15 min for all additional copper layers) and a third round of centrifugation at 500 rcf for 1 hr (500 rcf for 30 min for all additional copper layers) to separate free MOF particles. After the last round of centrifugation, the pellets were each dispersed in 0.5 mL ethanol. Then 0.5 mL of 50 mM TMA-BTC salt was added to each tube, the contents of each tube were mixed and sonicated, then allowed to stand for 10 minutes. Excess TMA- BTC salt was removed and AuNRs were washed with ethanol by three rounds of centrifugation at 2000 rcf for 15 minutes. After the last round of centrifugation, the pellets were dispersed in 0.5 mL of ethanol each in preparation for the next copper addition. These steps were repeated for the desired number of layers. When following the scale-up procedure using concentrated gold nanorods, nanorods sometimes became stuck near the top of the centrifuge tubes. In this scenario, it was often helpful to transfer the gold nanorod solution to new centrifuge tubes to prevent further nanorod build-up on the walls of the centrifuge tubes.

2.5.7 Adsorption Analysis

The BET equation is not always applicable to microporous materials and when it is applicable it must be applied to the appropriate pressure ranges.[37,38] Instrument software often automatically applies the BET equation to the relative pressure range of 0.05-0.30. For our measurements, that gave a BET surface area of 58 m^2/g and a C-constant of -288. The C-constant is related to the affinity of adsorption of the adsorbate gas to the sample, rendering negative values meaningless.[32,33] To identify the appropriate pressure range to apply the BET equation, the term $Q(P_o-P)$ should continually increase with respect to P/P_o. Accounting for the new relative pressure range the BET surface area was calculated more accurately. This more accurate analysis gave a surface area value of 63 m^2/g with a corresponding C-constant of 173.

To be able to compare the surface area of HKUST-1 coated AuNRs to bulk HKUST-1, the contribution of the AuNRs was subtracted from the total mass so that only the mass of the HKUST-1 shells was considered. First, the contribution of the gold nanorods to the mass of the HKUST-1 coated AuNRs was estimated by measuring the size average size of the AuNRs using TEM, then finding their volume assuming that they are shaped as cylinders with hemispherical end caps. In this case, the AuNRs were 86 ± 16 nm by 23 ± 3 nm, which gave an approximate volume V_{AuNR} of 32000 nm^3. TEM analysis of the HKUST-1 coated AuNRs showed that the average HKUST-1 shell thickness was 6.1 ± 0.8 nm, which was added to the dimensions of the AuNR cores so that an estimate of the total volume of a typical HKUST-1 coated AuNR V_{Total} could be made: 83000 nm^3. Subtracting V_{AuNR} from V_{Total} gave the volume of the HKUST-1 shell V_{MOF}: 51000 nm^3. Using the density of gold d_{Au}, 19.3 g/cm^3, and the ideal density of HKUST-1 d_{MOF}, 0.883 g/cm^3, the total mass of the HKUST-1 coated AuNR m_{total}, as well as the masses due to each component, m_{Au} and m_{MOF} was found.[39] The mass fraction X_{MOF} of HKUST-1 was determined using Equation 2.1.

$$X_{\mathrm{MOF}} = \frac{d_{\mathrm{MOF}} V_{\mathrm{MOF}}}{d_{\mathrm{MOF}} V_{\mathrm{MOF}} + d_{\mathrm{Au}} V_{\mathrm{Au}}}$$ **Equation 2.1**

Because the BET surface area corresponds to m_{total}, the surface area due to HKUST-1 alone was estimated by multiplying the BET surface area by X_{MOF}^{-1}. For our HKUST-1 coated AuNRs, that yielded a value of 900 m^2/g.

2.6 References

(1) Furukawa, H.; Cordova, K. E.; O'Keeffe, M.; Yaghi, O. M. The Chemistry and Applications of Metal-Organic Frameworks. *Science* **2013**, *341* (6149), 1230444.

(2) Burrows, N. D.; Lin, W.; Hinman, J. G.; Dennison, J. M.; Vartanian, A. M.; Abadeer, N. S.; Grzincic, E. M.; Jacob, L. M.; Li, J.; Murphy, C. J. Surface Chemistry of Gold Nanorods. *Langmuir* **2016**, *32* (39), 9905–9921.

(3) Chen, H.; Shao, L.; Li, Q.; Wang, J. Gold Nanorods and Their Plasmonic Properties. *Chem. Soc. Rev.* **2013**, *42* (7), 2679–2724.

(4) Koh, C. S. L.; Lee, H. K.; Han, X.; Sim, H. Y. F.; Ling, X. Y. Plasmonic Nose: Integrating MOF-Enabled Molecular Preconcentration with Plasmonic Array for Molecular-Level Volatile Organic Compounds Recognition. *Chem. Commun.* **2018**, *54* (20), 2546–2549.

(5) Xiao, J.-D.; Han, L.; Luo, J.; Yu, S.-H.; Jiang, H.-L. Integration of Plasmonic Effects and Schottky Junctions into Metal-Organic Framework Composites: Steering Charge Flow for Enhanced Visible-Light Photocatalysis. *Angew. Chem. Int. Ed.* **2017**, *57* (4), 1103–1107.

(6) Fu, X.; Lv, R.; Su, J.; Li, H.; Yang, B.; Gu, W.; Liu, X. A Dual-Emission Nano-Rod MOF Equipped with Carbon Dots for Visual Detection of Doxycycline and Sensitive Sensing of MnO4−. *RSC Adv.* **2018**, *8* (9), 4766–4772.

(7) Lin, W.; Murphy, C. J. A Demonstration of Le Chatelier's Principle on the Nanoscale. *ACS Cent. Sci.* **2017**, *3* (10), 1096–1102.

(8) Zeng, J.-Y.; Wang, X.-S.; Zhang, M.-K.; Li, Z.-H.; Gong, D.; Pan, P.; Huang, L.; Cheng, S.-X.; Cheng, H.; Zhang, X.-Z. Universal Porphyrinic Metal–Organic Framework Coating to Various Nanostructures for Functional Integration. *ACS Appl. Mater. Interfaces* **2017**, *9* (49), 43143–43153.

(9) Khaletskaya, K.; Reboul, J.; Meilikhov, M.; Nakahama, M.; Diring, S.; Tsujimoto, M.; Isoda, S.; Kim, F.; Kamei, K.; Fischer, R. A.; Kitagawa, S.; Furukawa, S. Integration of Porous Coordination Polymers and Gold Nanorods into Core–Shell Mesoscopic Composites toward Light-Induced Molecular Release. *J. Am. Chem. Soc.* **2013**, *135* (30), 10998–11005.

(10) Hu, P.; Zhuang, J.; Chou, L.-Y.; Lee, H. K.; Ling, X. Y.; Chuang, Y.-C.; Tsung, C.-K. Surfactant-Directed Atomic to Mesoscale Alignment: Metal Nanocrystals Encased Individually in Single-Crystalline Porous Nanostructures. *J. Am. Chem. Soc.* **2014**, *136* (30), 10561–10564.

(11) Zhao, Y.; Kornienko, N.; Liu, Z.; Zhu, C.; Asahina, S.; Kuo, T.-R.; Bao, W.; Xie, C.; Hexemer, A.; Terasaki, O.; Yang, P.; Yaghi, O. M. Mesoscopic Constructs of Ordered and Oriented Metal–Organic Frameworks on Plasmonic Silver Nanocrystals. *J. Am. Chem. Soc.* **2015**, *137* (6), 2199–2202.

(12) Ke, F.; Zhu, J.; Qiu, L.-G.; Jiang, X. Controlled Synthesis of Novel Au@MIL-100(Fe) Core–Shell Nanoparticles with Enhanced Catalytic Performance. *Chem. Commun.* **2013**, *49* (13), 1267–1269.

(13) Liao, J.; Wang, D.; Liu, A.; Hu, Y.; Li, G. Controlled Stepwise-Synthesis of Core–Shell Au@MIL-100 (Fe) Nanoparticles for Sensitive Surface-Enhanced Raman Scattering Detection. *Analyst* **2015**, *140* (24), 8165–8171.

(14) Cai, Y.; Wu, Y.; Xuan, T.; Guo, X.; Wen, Y.; Yang, H. Core–Shell Au@Metal–Organic Frameworks for Promoting Raman Detection Sensitivity of Methenamine. *ACS Appl. Mater. Interfaces* **2018**, *10* (18), 15412–15417.

(15) Sivapalan, S. T.; Vella, J. H.; Yang, T. K.; Dalton, M. J.; Swiger, R. N.; Haley, J. E.; Cooper, T. M.; Urbas, A. M.; Tan, L.-S.; Murphy, C. J. Plasmonic Enhancement of the Two Photon Absorption Cross Section of an Organic Chromophore Using Polyelectrolyte-Coated Gold Nanorods. *Langmuir* **2012**, *28* (24), 9147–9154.

(16) Richardson, J. J.; Cui, J.; Björnmalm, M.; Braunger, J. A.; Ejima, H.; Caruso, F. Innovation in Layer-by-Layer Assembly. *Chem. Rev.* **2016**, *116* (23), 14828–14867.

(17) Jiang, Y.; Zhang, X.; Dai, X.; Sheng, Q.; Zhuo, H.; Yong, J.; Wang, Y.; Yu, K.; Yu, L.; Luan, C.; Wang, H.; Zhu, Y.; Duan, X.; Che, P. In Situ Synthesis of Core–Shell Pt–Cu Frame@Metal–Organic Frameworks as Multifunctional Catalysts for Hydrogenation Reaction. *Chem. Mater.* **2017**, *29* (15), 6336–6345.

(18) Liu, Y.; Zhang, W.; Li, S.; Cui, C.; Wu, J.; Chen, H.; Huo, F. Designable Yolk–Shell Nanoparticle@MOF Petalous Heterostructures. *Chem. Mater.* **2013**, *26* (2), 1119–1125.

(19) Li, D.; Dai, X.; Zhang, X.; Zhuo, H.; Jiang, Y.; Yu, Y.-B.; Zhang, P.; Huang, X.; Wang, H. Silver Nanoparticles Encapsulated by Metal-Organic-Framework Give the Highest Turnover Frequencies of 10^5 h^{-1} for Three Component Reaction by Microwave-Assisted Heating. *J. Catal.* **2017**, *348*, 276–281.

(20) Zhao, M.; Deng, K.; He, L.; Liu, Y.; Li, G.; Zhao, H.; Tang, Z. Core–Shell Palladium Nanoparticle@Metal–Organic Frameworks as Multifunctional Catalysts for Cascade Reactions. *J. Am. Chem. Soc.* **2014**, *136* (5), 1738–1741.

(21) He, L.; Liu, Y.; Liu, J.; Xiong, Y.; Zheng, J.; Liu, Y.; Tang, Z. Core-Shell Noble-Metal@Metal-Organic-Framework Nanoparticles with Highly Selective Sensing Property. *Angew. Che. Int. Ed.* **2013**, *52* (13), 3741–3745.

(22) Choi, K. M.; Kim, D.; Rungtaweevoranit, B.; Trickett, C. A.; Barmanbek, J. T. D.; Alshammari, A. S.; Yang, P.; Yaghi, O. M. Plasmon-Enhanced Photocatalytic CO_2 Conversion within Metal–Organic Frameworks under Visible Light. *J. Am. Chem. Soc.* **2017**, *139* (1), 356–362.

(23) Shekhah, O.; Wang, H.; Kowarik, S.; Schreiber, F.; Paulus, M.; Tolan, M.; Sternemann, C.; Evers, F.; Zacher, D.; Fischer, R. A.; Wöll, C. Step-by-Step Route for the Synthesis of Metal−Organic Frameworks. *J. Am. Chem. Soc.* **2007**, *129* (49), 15118–15119.

(24) Nan, J.; Dong, X.; Wang, W.; Jin, W.; Xu, N. Step-by-Step Seeding Procedure for Preparing HKUST-1 Membrane on Porous α-Alumina Support. *Langmuir* **2011**, *27* (8), 4309–4312.

(25) Shekhah, O.; Fu, L.; Sougrat, R.; Belmabkhout, Y.; Cairns, A. J.; Giannelis, E. P.; Eddaoudi, M. Successful Implementation of the Stepwise Layer-by-Layer Growth of MOF Thin Films on Confined Surfaces: Mesoporous Silica Foam as a First Case Study. *Chem. Commun.* **2012**, *48* (93), 11434–4.

(26) Chui, S. S.-Y.; Lo, S. M.-F.; Charmant, J. P. H.; Orpen, A. G.; Williams, I. D. A Chemically Functionalizable Nanoporous Material $[Cu_3(TMA)_2(H_2O)_3]_n$. *Science* **1999**, *283* (5405), 1148–1150.

(27) Mendoza, S. M.; Arfaoui, I.; Zanarini, S.; Paolucci, F.; Rudolf, P. Improvements in the Characterization of the Crystalline Structure of Acid-Terminated Alkanethiol Self-Assembled Monolayers on Au(111). *Langmuir* **2007**, *23* (2), 582–588.

(28) Aprea, P.; Caputo, D.; Gargiulo, N.; Iucolano, F.; Pepe, F. Modeling Carbon Dioxide Adsorption on Microporous Substrates: Comparison between Cu-BTC Metal−Organic Framework and 13X Zeolitic Molecular Sieve. *J. Chem. Eng. Data* **2010**, *55* (9), 3655–3661.

(29) Lin, K.-S.; Adhikari, A. K.; Ku, C.-N.; Chiang, C.-L.; Kuo, H. Synthesis and Characterization of Porous HKUST-1 Metal Organic Frameworks for Hydrogen Storage. *Int. J. Hydrog. Energy* **2012**, *37* (18), 13865–13871.

(30) Jabbari, V.; Veleta, J. M.; Zarei-Chaleshtori, M.; Gardea-Torresdey, J.; Villagrán, D. Green Synthesis of Magnetic MOF@GO and MOF@CNT Hybrid Nanocomposites with High Adsorption Capacity towards Organic Pollutants. *Chem. Eng. J.* **2016**, *304* (C), 774–783.

(31) Shekhah, O.; Wang, H.; Strunskus, T.; Cyganik, P.; Zacher, D.; Fischer, R.; Wöll, C. Layer-by-Layer Growth of Oriented Metal Organic Polymers on a Functionalized Organic Surface. *Langmuir* **2007**, *23* (14), 7440–7442.

(32) Abadeer, N. S.; Brennan, M. R.; Wilson, W. L.; Murphy, C. J. Distance and Plasmon Wavelength Dependent Fluorescence of Molecules Bound to Silica-Coated Gold Nanorods. *ACS Nano* **2014**, *8* (8), 8392–8406.

(33) Vigderman, L.; Zubarev, E. R. High-Yield Synthesis of Gold Nanorods with Longitudinal SPR Peak Greater than 1200 Nm Using Hydroquinone as a Reducing Agent. *Chem. Mater.* **2013**, *25* (8), 1450–1457.

(34) Orendorff, C. J.; Murphy, C. J. Quantitation of Metal Content in the Silver-Assisted Growth of Gold Nanorods. *J. Phys. Chem. B* **2006**, *110* (9), 3990–3994.

(35) Mahalakshmi, G.; Balachandran, V. FT-IR and FT-Raman Spectra, Normal Coordinate Analysis and Ab Initio Computations of Trimesic Acid. *Spectrochim. Acta A Mol. Biomol. Spectrosc.* **2014**, *124* (C), 535–547.

(36) Andrade, Â. L.; Fabris, J. D.; Ardisson, J. D.; Valente, M. A.; Ferreira, J. M. F. Effect of Tetramethylammonium Hydroxide on Nucleation, Surface Modification and Growth of Magnetic Nanoparticles. *J. Nanomater.* **2012**, *12*, 454759.

(37) Rouquerol, J.; Llewellyn, P.; Rouquerol, F. Is the BET Equation Applicable to Microporous Adsorbents? *Stud. Surf. Sci. Catal.* **2007**, *160*, 49–56.

(38) Walton, K. S.; Snurr, R. Q. Applicability of the BET Method for Determining Surface Areas of Microporous Metal−Organic Frameworks. *J. Am. Chem. Soc.* **2007**, *129* (27), 8552–8556.

(39) Peng, Y.; Krungleviciute, V.; Eryazici, I.; Hupp, J. T.; Farha, O. K.; Yildirim, T. Methane Storage in Metal–Organic Frameworks: Current Records, Surprise Findings, and Challenges. *J. Am. Chem. Soc.* **2013**, *135* (32), 11887–11894.

CHAPTER 3: SYNTHESIS OF POROUS COLLOIDAL NANOPARTICLES [2]

3.1 Abstract

Porous nanomaterials have very high surface areas and are attractive for many catalytic and biomedical applications. Recently, there have been an increased number of reports of the synthesis of colloidal stable metal-organic framework (MOF) nanoparticles. MOF nanoparticles also present an opportunity for more fundamental nanoparticle research, as it may be possible to use the pores to engineer protein coronas at the surface of nanoparticles. The MOF, ZIF-8, is among the most widely studied MOFs and has exceptional chemical stability making it an ideal candidate to be used as the porous material to control protein orientation at the surface of nanoparticles. The implications of the protein corona remain one of the main challenges faced by nanoparticles and their potential to be used for drug delivery and biomedical imaging. The work presented involves the synthesis and characterization of ZIF-8 nanoparticles and ZIF-8 shells around gold nanoparticles.

[2] This chapter was reproduced from a manuscript in preparation for publication.

3.2 Introduction

Porous nanoparticles present an opportunity to control biomolecules orientation at the surface of the nanoparticle. The chemical makeup and orientation of the protein corona is inherently unpredictable and difficult to control.[1,2] Proteins are known to diffuse through pores in biological systems, and also synthetic systems such as mesoporous silica.[3,4] Metal-organic frameworks (MOFs) have advantages over silica in that they are crystalline materials with defined pore channels, thus they have a uniform pore structure on the surface.[5,6] This makes them intriguing materials to use to partially sequester biomolecules leading to a preferred orientation of the biomolecules on the surface of MOF nanoparticles.

A subclass of MOFs composed of singular metal ions rather than metal containing hubs, are referred to as zeolitic imidazole frameworks, or ZIFs.[6,7] An advantage of ZIFs is their high chemical and thermal stability compared to other MOFs.[8,9] Many MOFs have limited aqueous stability, making them not suitable for the desired application of controlling biomolecular orientation. ZIF-8 is one of the more widely studied MOFs, it has a very well characterized pore structure and diverse synthetic methods that can be used to make nanosized ZIF-8 materials; making ZIF-8 an ideal candidate for the studies looking at controlling biomolecule orientation.[7,10,11]

Interactions between biomolecules and MOFs have been widely studied, but most reports do not use nanoscale MOF materials.[12–16] Biomolecules can be grafted to MOF surfaces, infiltrate the MOF pores, or be encapsulated by a MOF.[17] Chen *et al.* has observed cytochrome c penetrating the pores of a MOF in which the pore size is smaller than that of the protein; they hypothesize the partial unfolding of cytochrome c during the pore migration process.[18] Pan *et al.* has explored how enzymes orient on ZIF-8 surfaces using spin-labelled EPR studies.[19] Deng *et al.* has shown the

ability of ZIF-8 to extract digested peptides in the presence of large proteins.[20] Despite the great work being done surrounding MOF-protein conjugates, there is still a limited number of reports involving MOF nanoparticles, and presently there are not any reports utilizing the MOF pores to control biomolecular orientation.

There has been an increase in the number of reported syntheses for both MOF nanoparticles (nanoMOFs) and gold nanoparticles (AuNP) encapsulated by a MOF shell (AuNP@MOF). In this work, some of these reported syntheses are adapted to synthesize different types of porous nanoparticles. The desired porous nanoparticle library consists of entirely porous nanospheres and nanorods made of ZIF-8, as well as gold nanospheres (AuNS) and nanorods (AuNR) encapsulated with a ZIF-8 shell. ZIF-8 nanoparticles were successfully synthesized along with ZIF-8 shells around AuNRs. ZIF -8 nanorods and ZIF-8 coating of AuNS was attempted, but the reproducible synthesis of those nanoparticles was not achieved.

3.3 Materials and Methods

3.3.1 Materials and Instrumentation

2-methylimidazole (99%), zinc nitrate hexahydrate (98%), Brij® C10, ammonium bicarbonate (>99.5%), polyvinylpyrrolidone (PVP, 29k), hydroquinone (99%), cetyltrimethylammonium bromide (CTAB, 99%), silver nitrate (99%), sodium citrate tribasic dihydrate, and sodium borohydride (99%) were purchased from Sigma-Aldrich. Sodium hydroxide (ACS grade), and sodium chloride were purchased from Fisher Scientific. Ethanol was purchased from Decon Laboratories Inc., cyclohexane and methanol were purchased from Macron Fine Chemicals. All chemicals were used without further purification. Deionized water was purified

using a Barnstead Nanopure II purification system.

Dynamic light scattering (DLS) and ζ-potential were measured using a Malvern Zetasizer Nano ZS instrument. UV-vis spectra were obtained using a Cary 5000 UV–vis–near-infrared spectrophotometer. Scanning electron microscopy (SEM) was performed on a Hitachi S4700 instrument. Transmission electron microscopy (TEM) was performed on a JEOL 2100 Cryo LaB_6 or a JEOL 2010 LaB_6 instrument operated at 200 kV. All sizing analysis was completed using ImageJ and a minimum of 300 nanoparticles was measured. Powder X-ray diffraction (XRD) was taken using a Bruker D8 Venture Duo instrument. Nitrogen adsorption measurements were obtained using a Micromeritics 3 Flex Surface Area and Pore Analyzer.

3.3.2 Synthesis of Gold Nanorods

Gold nanorods with an aspect ratio of 3.7 were synthesized using a method adapted from Vigderman and Zubarev.[21] A typical 1 L synthesis of AuNRs requires two batches of CTAB-capped seeds. Gold seeds were prepared by adding 0.50 mL of 0.010 M $HAuCl_4 \cdot 3H_2O$ to 9.5 mL of 0.10 M CTAB. The seed solution was stirred rapidly, and then ice-cold 0.010 M sodium borohydride in 0.010 M NaOH was freshly prepared. Immediately upon preparation, 460 μL of the sodium borohydride solution was added quickly to the stirring seed solution. Following the addition of sodium borohydride, the seed solution color turned dark brown immediately. The seeds were aged for 1 hour before use.

The typical 1 L growth solution was prepared by adding 950 mL of 0.1 M CTAB to a large Erlenmeyer flask, followed by the addition of 1.30 mL of 0.10 M $AgNO_3$, and then 50 mL of 0.010 M $HAuCl_4 \cdot 3H_2O$. The solution was stirred gently, and then 50 mL of 0.10 M hydroquinone was added. A few seconds after the addition of hydroquinone, the solution turned colorless, at which

time 16 mL of the Au seeds was added. The growth solution was gently stirred overnight and kept at 27 °C. The nanorods were purified with centrifugation at 8,000 rcf, the supernatants were discarded and the nanorod pellet was redispersed in nanopure water. The nanorods were then stored at room temperature. Figure 3.1 shows representative TEM images of the as-synthesized AuNRs. The AuNR dimensions were 67 ± 9 nm long and 18 ± 4 nm wide.

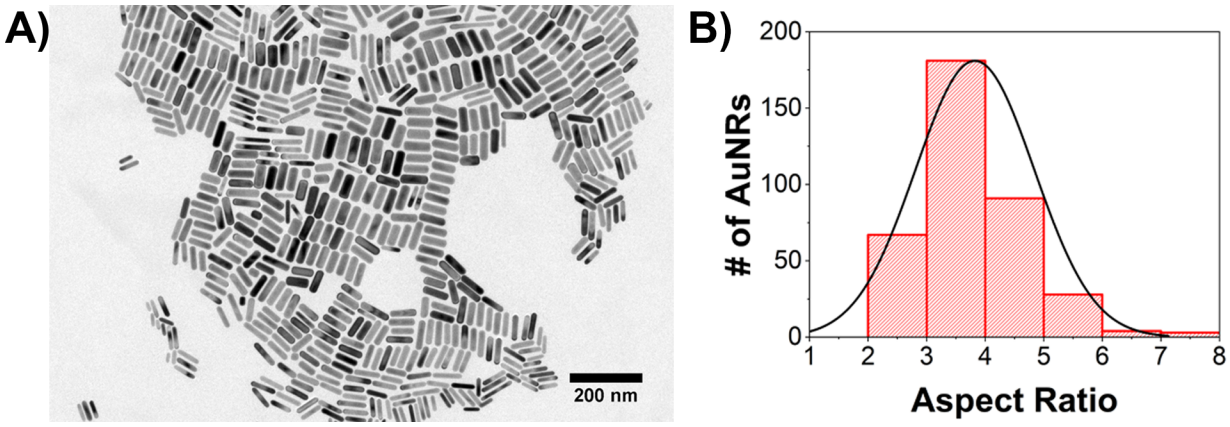

Figure 3.1: Characterization of synthesized AuNRs. (A) TEM image (B) TEM sizing analysis on the aspect ratio of the AuNRs, AR = 3.7.

3.3.3 ZIF-8 Coating of Gold Nanorods

The procedure used for ZIF-8 coating of AuNRs was adapted from Li and co-workers.[22] First, 40 mL of 1 nM CTAB-capped AuNRs were prepared from the more concentrated synthesized AuNR stock solution. The AuNRs were washed by centrifugation at 8,000 rcf and redispersion into 40 mL of nanopure water. The AuNRs were added to a 500 mL Erlenmeyer flask and stirred gently. Next, 200 mL of 50 mg/mL PVP in methanol was prepared and added into the flask. The solution was allowed to stir gently overnight. The AuNRs were purified with centrifugation at 8,000 rcf and were redispersed in methanol.

The PVP-capped AuNRs were then used to template the growth of the ZIF-8 shells. First, 40 mL of 1 nM PVP-capped AuNRs were added to a flask, followed by the addition of 80 mL of 2 methylimidazole (142.5 mg) in methanol. The solution was stirred for 5 minutes, and then a methanol solution of $ZnNO_3 \bullet 6H_2O$ (303.8 mg dissolved in 80 mL of methanol) was added. After 1 hr the ZIF-8 coated AuNRs were centrifuged at 4,000 rcf for 30 min. The resulting AuNR@ZIF-8 nanoparticles were redispersed in methanol, washed again at 4,000 rcf for 30 min, and then slowly washed at 500 rcf for 1 hr to help separate any free ZIF-8 particles. The AuNR@ZIF-8 particles were stored in methanol until use. Figure 3.2 shows the UV-vis and ζ-potential for each step throughout the ZIF-8 coating process.

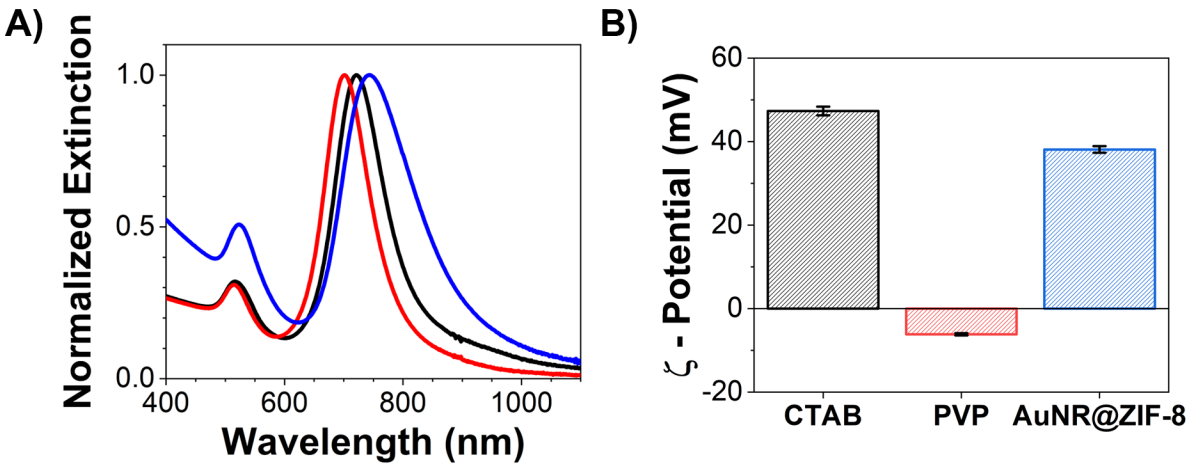

Figure 3.2: Characterization of the process for the ZIF-8 coating of AuNRs. (A) Normalized UV-vis extinction spectra. (B) ζ-potential for each AuNR surface chemistry. The CTAB AuNRs were dispersed in water, while the PVP and ZIF-8 coated AuNRs were dispersed in methanol. (Black data: CTAB, red data: PVP, blue data: ZIF-8 coated AuNRs).

3.3.4 Synthesis of 40 nm Gold Nanospheres

Gold nanospheres (AuNS), roughly 40 nm in size, were synthesized by the seed mediated method reported by Perrault and Chan.[23] Gold seeds were prepared by adding 30 mL of nanopure water to a 100 mL Erlenmeyer flask with 0.30 mL of 0.029 M $HAuCl_4 \bullet 3H_2O$ and vigorously stirred. The solution was heated and brought to a boil, as soon as the solution started to boil 0.9 mL of 1% m/v sodium citrate was quickly added. The flask was removed from heat and stirring after 15 minutes, the synthesis was complete as indicated by the bright red color of the solution. The resulting seeds were around 16 ± 2 nm in size, as determined by TEM. Once the seeds were cooled to room temperature, the growth solution was prepared. To prepare the growth solution, 382 mL of nanopure water was added to a 500 mL Erlenmeyer flask along with 4 mL of 0.029 M $HAuCl_4 \bullet 3H_2O$. Next, 10 mL of freshly prepared seeds were added while stirring, followed by the quick addition of 0.88 mL of 1% m/v sodium citrate, and then 4 mL of 0.030 M hydroquinone was added. The color changed immediately following the addition of hydroquinone, the solution was stirred for 30 minutes and then purified by centrifugation at 4,000 rcf for 20 minutes. The synthesized 44 ± 8 nm gold nanospheres were redispersed in nanopure water and stored until future use. Representative TEM images and UV-vis are shown in Figure 3.3.

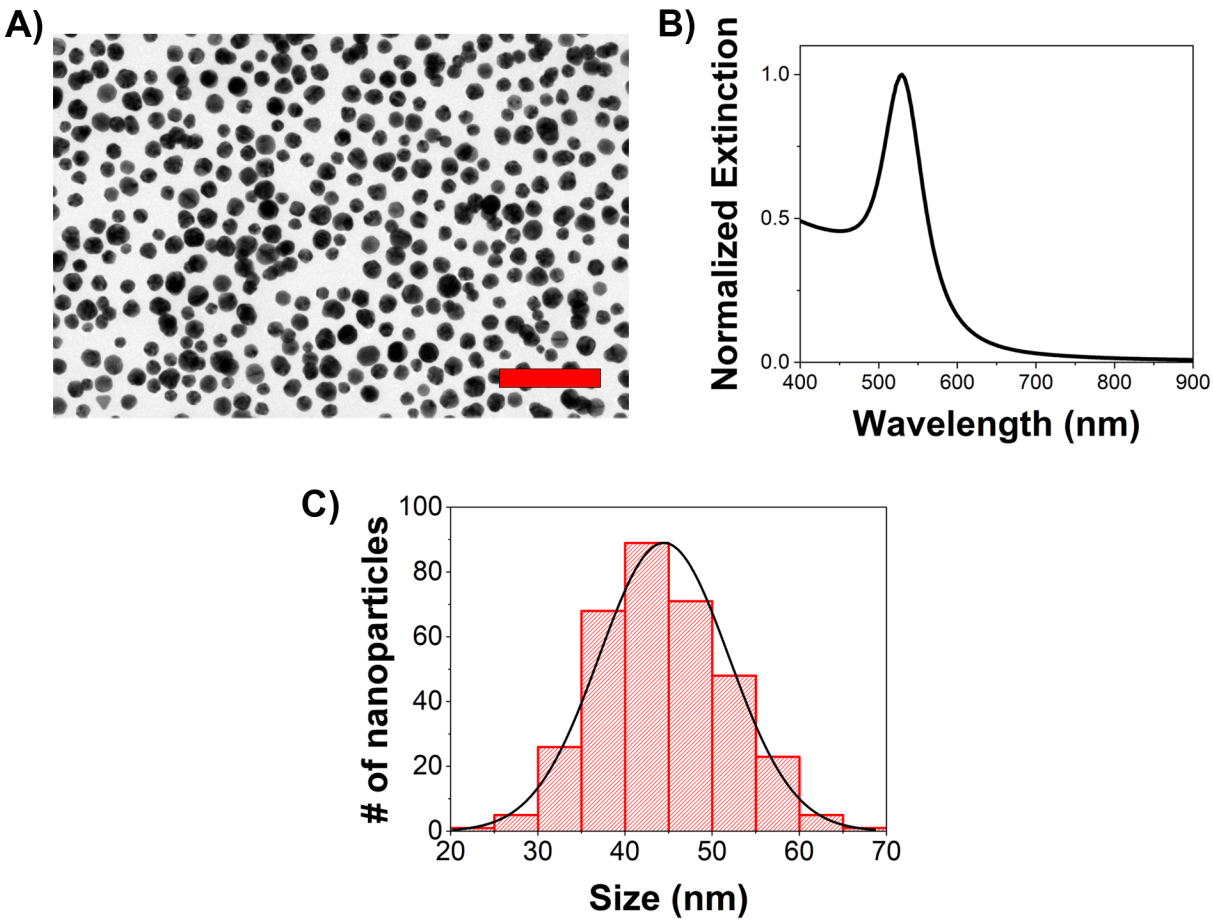

Figure 3.3: Characterization of citrate capped AuNS (44 ± 8 nm). (A) Representative TEM image (scale bar = 300 nm) (B) UV-vis extinction spectrum (C) TEM sizing distribution

3.3.5 ZIF-8 Coating of Gold Nanospheres

The procedure used for ZIF-8 coating of AuNSs was adapted from the reported procedure by Li and co-workers which was used to ZIF-8 coat AuNRs.[22] First, 15 mL of 0.2 nM citrate-capped AuNS roughly 40 nm in size were added to a centrifuge tube. Then, 6 mL of a 50 mg/mL aqueous PVP solution was added to the tube, and the tube was mechanically shaken for 5 hours. The resulting PVP-capped AuNS were centrifuged at 5,000 rcf for 30 minutes, and washed twice

with methanol. For the ZIF-8 coating, 10 mL of 0.2 nM PVP-capped AuNS were added to a small Erlenmeyer flask and stirred. Next, 10 mL of a XX mM methanolic solution of 2-methylimidazole was added. After 5 minutes, 10 mL of a XX mM methanolic solution of $ZnNO_3•6H_2O$ was added. The solution was stirred for 1 hr, and the resulting ZIF-8 coated AuNSs were centrifuged at 2,500 rcf for 20 minutes and washed with methanol three times. This ZIF-8 coating process lacked reproducibility and impeded on the ability to use these nanoparticles for future protein studies.

3.3.6 ZIF-8 Nanoparticle Synthesis

ZIF-8 nanoparticles were synthesized via a reverse micelle method that was previously reported by Zhao and co-workers.[24] For this synthesis, two similar solutions were prepared and then combined. The first solution contained 3.420 g of Brij C10, 15.0 mL of cyclohexane, and 1 mL of 1.0 M aqueous $ZnNO_3•6H_2O$. All of the contents were added into a 50 mL round-bottom flask, heated at 37 °C, and stirred until a clear solution was obtained. The second solution contained 3.420 g of Brij C10, 15.0 mL of cyclohexane, and 1 mL of 4.0 M aqueous 2-methylimidazole. These contents were added into a round-bottom flask, heated at 37 °C, and stirred until a clear solution was obtained as well. Once both solutions were clear, the second solution (containing 2-metyhlimidazole) was poured into the first. The resulting solution was kept under the same heating, and stirring conditions for 2 hrs. The ZIF-8 nanoparticles were then collected by adding in equivalent amounts of ethanol (30 mL), followed by centrifugation at 12,000 rcf for 20 minutes. The product was then washed with ethanol and centrifugation an additional three times before solvent removal under vacuum. Proportional scale-ups were attempted, but did not result in as high quality of ZIF-8 nanoparticles, so multiple batches were synthesized and then combined to have enough material for all desired experiments.

3.3.7 ZIF-8 Nanorod Synthesis

The synthesis of ZIF-8 nanorods was attempted using a procedure reported by Yang and co-workers.[25] In this synthesis, varying amounts of CTAB are used to produce ZIF-8 nanocrystals of different shapes. In a typical synthesis, 0.1812 g of $Zn(OAc)_2$, 2.4333 g of 2-methylimidazole, 0.1337 g of CTAB, and 32 mL of water were added into a Teflon lined hydrothermal reactor cell. The reactor cell was tightly sealed and then placed into an oven at 120 °C for 24 hours. The resulting product was centrifuged at 10,000 rcf for 20 minutes and washed with methanol three times. The reported ZIF-8 nanorods were not able to be reproduced in high quality. Many large irregular shaped ZIF-8 nanoparticles were produced, and the attempts of which did contain nanorods had very poor shape and size control.

3.3.8 Synthesis of ZIF-8 Microcrystals

As a form of comparison in some of the studies, standard ZIF-8 particles were synthesized. These particles were synthesized according to a method reported by Tanaka and co-workers.[26] For the synthesis, a $ZnNO_3 \bullet 6H_2O$ solution was prepared by dissolving 0.745 g in 10 mL of nanopure water and a 2-methylimidazole solution was prepared by dissolving 12.3 g in 90 mL of nanopure water. The $ZnNO_3 \bullet 6H_2O$ solution was then added to the 2-methylimidazole solution while stirring. The solution turned turbid quickly, and was stirred for 24 hrs. The ZIF-8 particles were purified by centrifugation at 4,000 rcf for 15 min and washed with methanol five times. The ZIF-8 particles were dried under vacuum and stored for analysis.

3.3.9 Polyelectrolyte Wrapping Gold Nanoparticles

Polyelectrolyte wrapped AuNS and AuNRs were used as non-porous controls for protein display studies. Both nanoparticle types were terminated with positively-charged polyelectrolytes to match similar surface charge of the ZIF-8 shells and nanoparticles. The methods used for polyelectrolyte wrapping were adapted from previous reports.[27–29] Briefly, 10 mg/mL polymer solutions (cationic PAH, anionic PSS, and cationic PDADMAC) were prepared in a 1 mM NaCl solution. Next, 6 mL of the first polyelectrolyte layer was added to 30 mL of 0.5 nM CTAB-capped AuNRs or citrate-capped AuNSs. The first polyelectrolyte layer for AuNS was PAH and for AuNRs it was PSS. The nanoparticle solutions were stirred overnight and purified with centrifugation before being redispersed in nanopure water. The AuNRs needed a second polyelectrolyte layer to achieve the desired positive charge. The second layer, PDADMAC, was added following the same steps as the first layer. ζ-potential results for the polyelectrolyte wrapping process for AuNSs and AuNRs are shown in Figure 3.4.

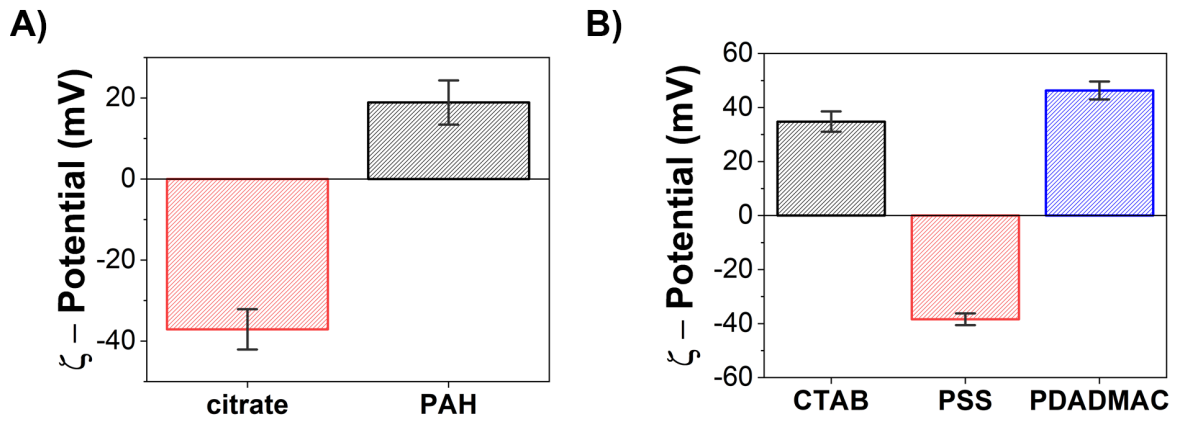

Figure 3.4: ζ-potential of polyelectrolyte wrapping of (A) AuNSs and (B) AuNRs. The terminal polyelectrolyte layer (PAH or PDADMAC) provides a similar positive surface charge to that of the ZIF-8.

3.4 Results and Discussion

In principle, an engineered nano-porous surface could promote a preferred protein orientation if electrostatics or other factors were favorable. Colloidal nanocrystalline MOFs are excellent candidates to explore such interactions; the MOF chosen in these experiments, ZIF-8, has pore sizes of 1.2 nm and 0.34 nm.[30] It has been previously found that MOF shells can be grown on AuNRs.[22,31–33] The comparison of a porous shell to a fully porous nanoparticle may allow to control the degree of protein chain penetration into nanoscale pores, leading to engineered protein coronas on nanoscale surfaces.

The MOF chosen for the studies was ZIF-8, a well-studied MOF composed of 2-methylimidazole linkers and zinc(II) nodes.[7,11] One important factor in the choice of ZIF-8 is its aqueous stability.[8,9] ZIF-8 nanoparticles were synthesized using a previously reported reverse micelle method.[24] Using this method, spherical nanoZIF-8 particles (39 ± 5 nm) were produced (Figure 3.5A and 3.5B), which agrees well with hydrodynamic diameter data from dynamic light scattering (Figure 3.5C). Powder XRD confirmed the presence of crystalline ZIF-8 (Figure 3.6A). The BET surface area was determined from nitrogen adsorption measurements (Figure 3.6B), the surface area was 1274 m^2/g. The calculated BET surface area and c-constant analysis was based off previous reports.[34] Pore size distribution was determined using non-local density functional theory (NLDFT) methods, and the demo version of SAIEUS software from Micromeritics. This pore distribution method has been previously reported, and does a better job at modeling micropores compared to the traditional BJH method.[35] The nanoZIF-8 showed pore size distribution centered around 0.65 nm, 1.1 nm, 2.8 nm, and 24 nm. The full pore distribution is shown in Figure 3.6C and Figure 3.6D. The microporous pores are within range of the anticipated ZIF-8 pores of 1.2 nm and 0.34 nm. The pore distribution around 2.8 nm is attributed to the pore

openings being wider on highly curved surfaces due to multidomain growth, which has previously been observed.[22] The broad pore distribution between 20 – 30 nm is attributed to the space between individually packed nanoZIF-8 particles.

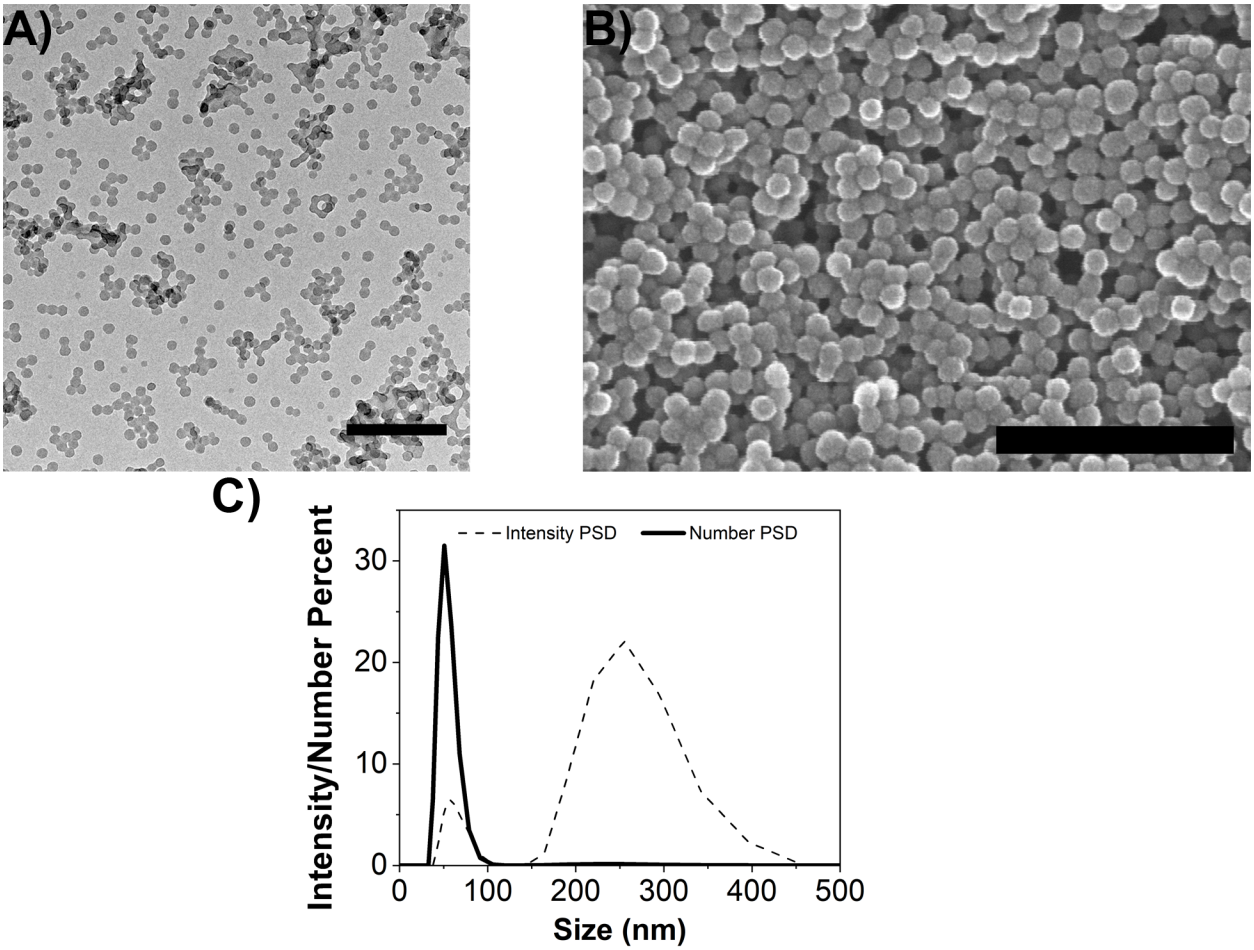

Figure 3.5: Characterization of ZIF-8 nanoparticles. (A) TEM image (scale bar = 300 nm). (B) SEM image (scale bar = 300 nm). (C) Dynamic Light Scattering (DLS) sizing data of nanoZIF-8 particle in EtOH. Using the number particle size distribution, the size was 49 ± 4 nm. The intensity distribution is skewed due to the few large ZIF-8 particles produced during the synthesis.

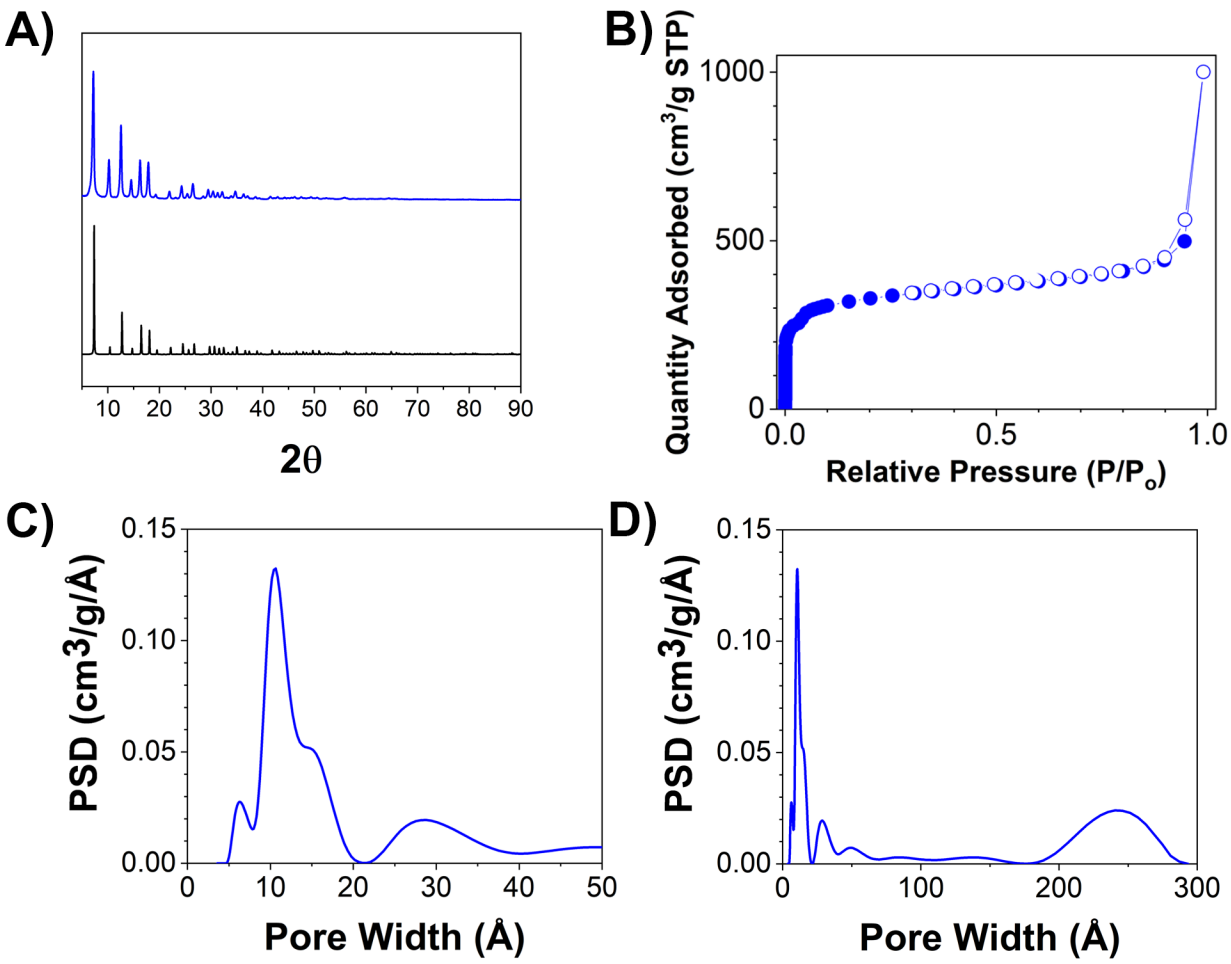

Figure 3.6: Characterization of ZIF-8 nanoparticles. (A) Powder XRD (black data: ZIF-8, blue data: nanoZIF-8). (B) N_2 adsorption isotherm (filled circles: adsorption, open circles: desorption). (C) NanoZIF-8 pore size distribution determined using non-local density functional theory (NLDFT) methods and the demo version of the SAIEUS software from micromeritics. (D) Entire pore size distribution.

The other porous nanoparticle examined consisted of ZIF-8 shells around a AuNRs. The AuNRs were synthesized using the common seed-mediated, hydroquinone reduction method.[21] Using this method produced AuNRs with an aspect ratio of 3.7 and a longitudinal plasmon near 800 nm. The ZIF-8 coating of AuNRs was done according to a previously reported procedure.[22] The AuNR surface was first modified and coated with PVP. Once coated with PVP, methanol solutions containing 2-methylimadzole and $Zn(NO_3)$ were added. After 1 hour of continual stirring, individual AuNRs were coated with ZIF-8 as seen in the electron microscopy images in Figure 3.7A and 3.7B. Using the TEM images, the shell size was measured at 39 ± 8 nm on the ends and 43 ± 6 nm on the sides.

To further confirm the synthesis of ZIF-8 around the AuNRs, STEM-EDS was used to create elemental map, Figure 3.8. Powder XRD (Figure 3.9A) was also used to confirm the presence of ZIF-8, the diffraction pattern clearly shows the crystalline ZIF-8 and Au core. The BET surface area for AuNR@ZIF-8 was 783 m^2/g, and when calculated for just the MOF shell it was 1260 m^2/g, the nitrogen adsorption isotherm is shown in Figure 3.9B. The calculated BET surface area and c-constants analysis was based off of previous reports.[34] Pore size distribution was determined using the same NLDFT methods previously mentioned. For the AuNR@ZIF-8 particles the pore size distributions were centered around 1.1 nm, 1.5 nm, and 2.8 nm. The pore distribution (Figure 3.9C and 3.9D) was very similar to the nanoZIF-8 distribution, except the smallest pore size (0.65 nm) was not observed for the AuNR@ZIF-8 particles. This is not uncommon when MOFs are grown around surfaces, as the multidomain growth often leads to slight changes in the pore structure.

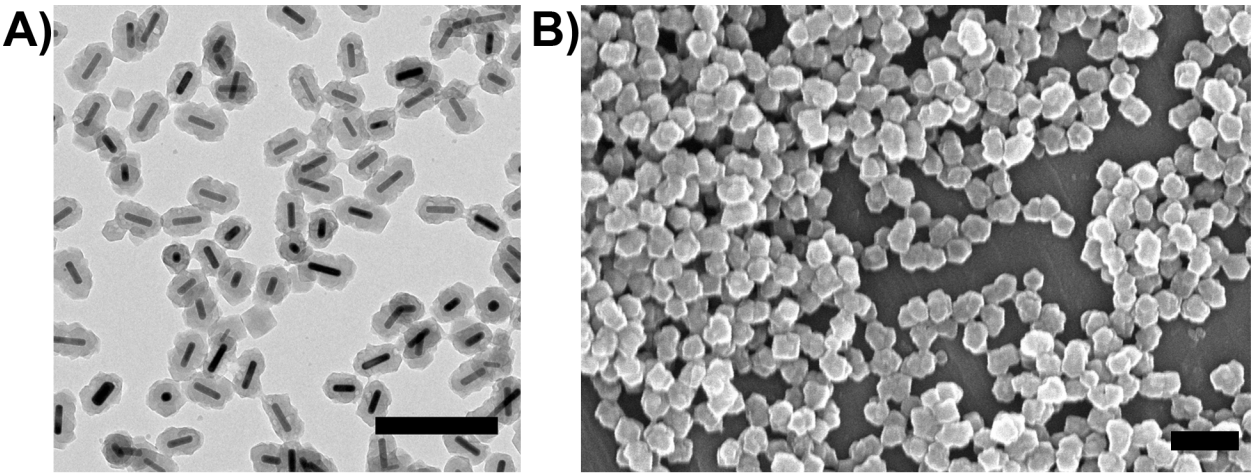

Figure 3.7: Characterization of AuNR@ZIF-8. (A) TEM image (scale bar = 300 nm). (B) SEM image (scale bar = 300 nm).

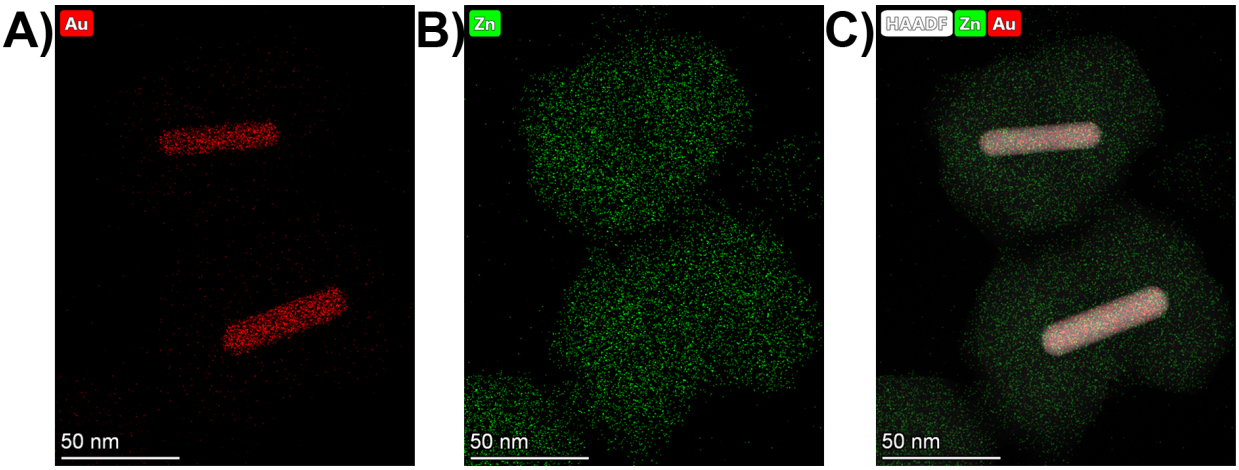

Figure 3.8: STEM-EDS maps for (A) Au (red) (B) Zn (green), and (C) the combined maps.

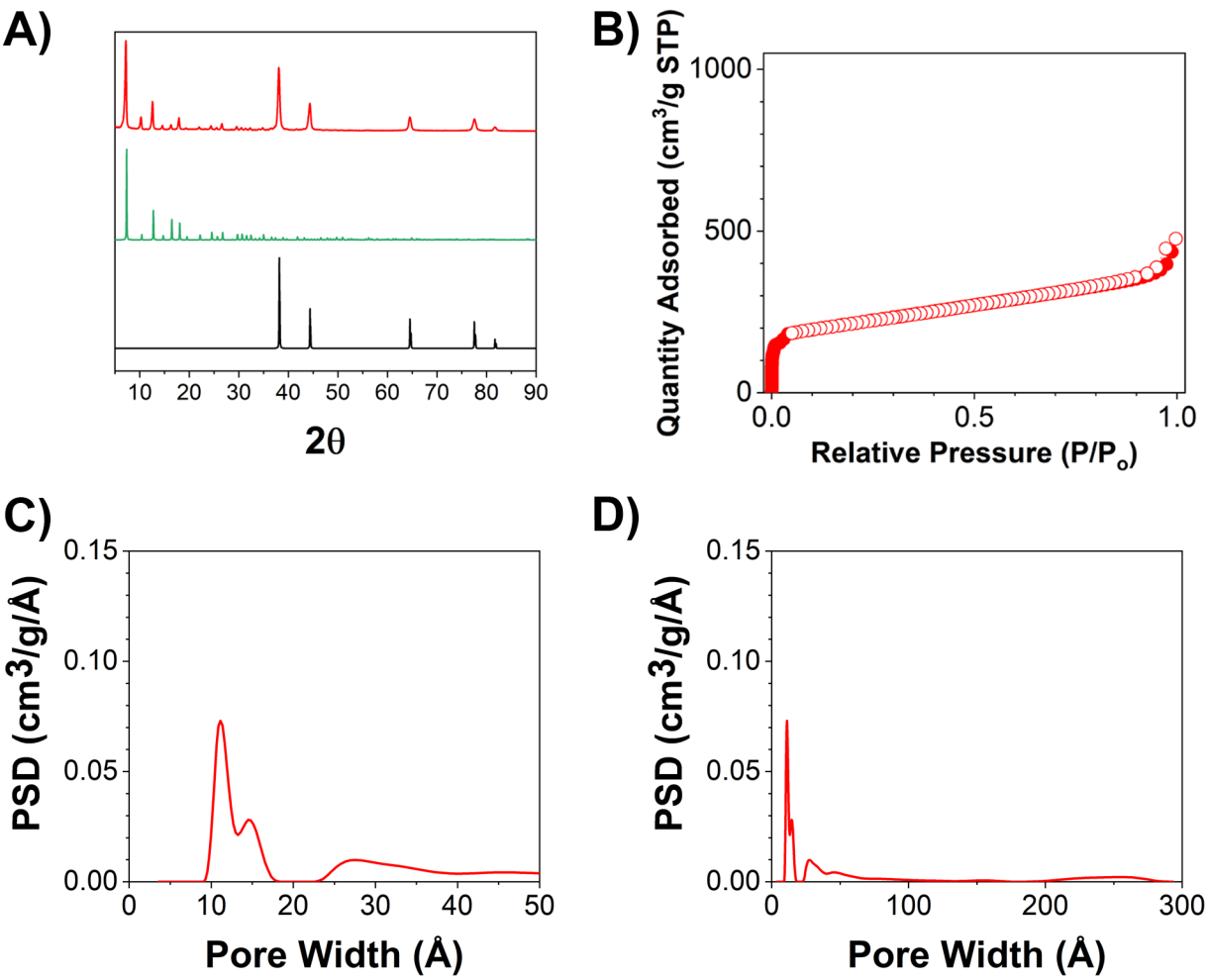

Figure 3.9: Characterization of AuNR@ZIF-8. (A) Powder XRD (black data : Au, green data: ZIF-8, red data: AuNR@ZIF-8). (B) N_2 adsorption isotherm (filled circles: adsorption, open circles: desorption). (C) AuNR@ZIF-8 pore size distribution determined using non-local density functional theory (NLDFT) methods and the demo version of the SAIEUS software from micromeritics. (A) Zoomed in view of the microporous porous region. (D) Entire pore size distribution.

The procedure used to coat AuNRs with ZIF-8 was also employed to try and coat AuNS with ZIF-8. Briefly, 40 nm AuNS were synthesized from a previously reported seed-mediated method.[23] The ZIF-8 coating of AuNS was done by first functionalizing the surface with PVP. The growth of the ZIF-8 shell was done in methanol, where a solution containing the linker (2-methylimidazole) was added to the PVP AuNS, followed by the addition of a solution containing the $Zn(NO_3)$. Characterization from one synthetic batch is shown in Figure 3.10. The AuNS were singularly encapsulated, but there was also a large production of free ZIF-8 nanoparticles. This level of synthetic quality was not able to be reproduced, despite many efforts in changing both the AuNS and MOF precursor concentrations, as well as experimenting with the reaction time. A very recent report showed the successful synthesis of ZIF-8 shells on AuNSs.[36] Their synthetic procedure was very similar, they used 40 nm AuNS that were PVP functionalized. However, for there growth solution they used very small amounts of MOF precursors and heated the growth solution to 50 °C. This may be a quality synthetic method to use in the future to expand the porous nanoparticle library for protein orientation studies.

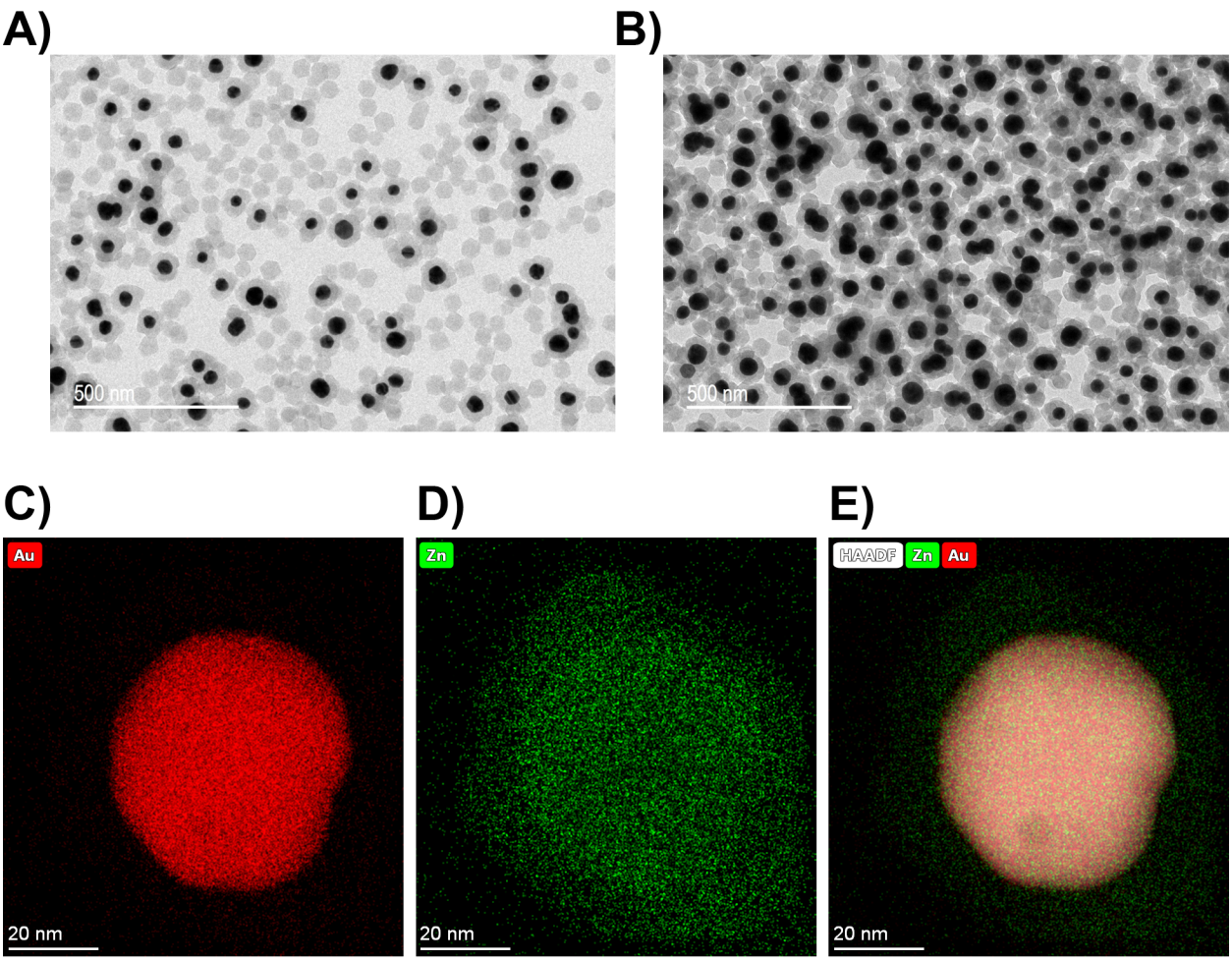

Figure 3.10: Characterization of ZIF-8 coated AuNS, the representative TEM images are shown in (A) and (B). STEM-EDS mapping is shown in (C) Au, red (D) Zn, green and (E) Combined elemental maps.

An effort was made to synthesize ZIF-8 nanorods, which would provide a better comparison to the AuNR@ZIF-8 nanoparticles. There is one reported synthesis of ZIF-8 nanorods, where CTAB is used to control the morphology of the ZIF-8 nanoparticles.[25] In this report, a variety of different ZIF-8 morphologies were produced through a hydrothermal synthesis and varying the amount of CTAB. Many attempts were tried to reproduce this work with no success,

Figure 3.11 shows the TEM images from a typical synthesis. While some rod-shapes were produced, there was very poor shape yield. The anticipated ZIF-8 nanorods would have dimensions in the hundreds of nanometers range, which is far too large to provide an accurate comparison to the AuNR@ZIF-8 nanoparticles. Significant work is necessary to develop an adequate procedure to make ZIF-8 nanorods if that nanoparticle type is desired in the future.

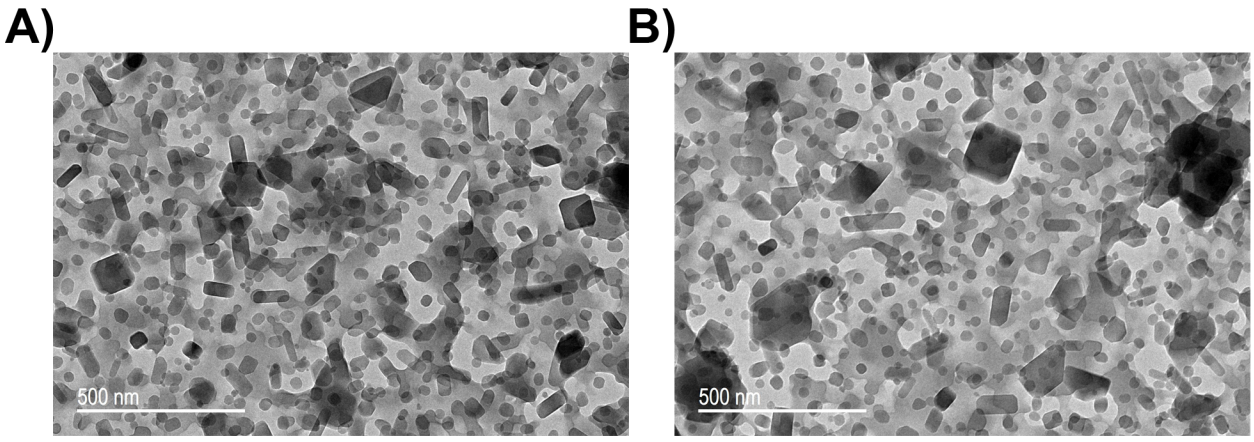

Figure 3.11: Representative TEM images of the attempted ZIF-8 nanorod synthesis. A broad distribution of ZIF-8 shapes and sizes were produced, with only few nanoparticles resembling that of a rod shape.

The ultimate goal if this work is to use porous nanoparticle surfaces to control protein orientation. To do so, the reliable and reproducible synthesis of porous nanoparticles was necessary. This work shows that two types of porous nanoparticles were produced, one being an entirely porous ZIF-8 nanoparticle and the other being a ZIF-8 shell around a AuNR. With ZIF-8 being one of the more aqueous stable MOFs, these nanoparticles are well suited for the desired protein orientation studies. The two nanoparticle types provide an interesting comparison for the protein orientation experiments, to see if the orientation behavior is dependent on the porous

nanoparticle shape, as well as whether or not the nanoparticle is entirely porous or has a rigid core.

3.5 Conclusions

The successful synthesis of ZIF-8 nanoparticles and ZIF-8 shells around AuNRs was achieved. The spherical ZIF-8 nanoparticles and individually encapsulated AuNRs with a ZIF-8 shell were clearly visualized using both TEM and SEM. Powder XRD and N_2 adsorption measurements were used to characterize and confirm the ZIF-8 structure. The pore size distribution of both types of nanoparticles were also investigated, and the pore distributions were very similar to one another. These porous nanoparticles will provide great platforms for the protein interaction studies explored in Chapter 4. Unfortunately, the current porous nanoparticle library was unable to be expanded to ZIF-8 nanorods and ZIF-8 coated AuNS. The synthetic methods used for those nanoparticles produced low quality nanoparticles with poor reproducibility, more synthetic development is required to produce adequate ZIF-8 nanorods and ZIF-8 coated AuNS.

3.6 References

(1) Wolfram, J.; Yang, Y.; Shen, J.; Moten, A.; Chen, C.; Shen, H.; Ferrari, M.; Zhao, Y. The Nano-Plasma Interface: Implications of the Protein Corona. *Colloids Surf. B* **2014**, *124*, 17–24.

(2) Lundqvist, M.; Cedervall, T. Three Decades of Research about the Corona Around Nanoparticles: Lessons Learned and Where to Go Now. *Small* **2020**, *16* (46), 2000892.

(3) Schlipf, D. M.; Rankin, S. E.; Knutson, B. L. Pore-Size Dependent Protein Adsorption and Protection from Proteolytic Hydrolysis in Tailored Mesoporous Silica Particles. *ACS Appl. Mater. Interfaces* **2013**, *5* (20), 10111–10117.

(4) Hamman, B. D.; Chen, J.-C.; Johnson, E. E.; Johnson, A. E. The Aqueous Pore through the Translocon Has a Diameter of 40–60 Å during Cotranslational Protein Translocation at the ER Membrane. *Cell* **1997**, *89* (4), 535–544.

(5) Stock, N.; Biswas, S. Synthesis of Metal-Organic Frameworks (MOFs): Routes to Various MOF Topologies, Morphologies, and Composites. *Chem. Rev.* **2011**, *112* (2), 933–969.

(6) Furukawa, H.; Cordova, K. E.; O'Keeffe, M.; Yaghi, O. M. The Chemistry and Applications of Metal-Organic Frameworks. *Science* **2013**, *341* (6149), 1230444.

(7) Chen, B.; Yang, Z.; Zhu, Y.; Xia, Y. Zeolitic Imidazolate Framework Materials: Recent Progress in Synthesis and Applications. *J. Mater. Chem. A* **2014**, *2* (40), 16811–16831.

(8) Yuan, S.; Feng, L.; Wang, K.; Pang, J.; Bosch, M.; Lollar, C.; Sun, Y.; Qin, J.; Yang, X.; Zhang, P.; Wang, Q.; Zou, L.; Zhang, Y.; Zhang, L.; Fang, Y.; Li, J.; Zhou, H.-C. Stable Metal-Organic Frameworks: Design, Synthesis, and Applications. *Adv. Mater.* **2018**, *30* (37), 1704303.

(9) Burtch, N. C.; Jasuja, H.; Walton, K. S. Water Stability and Adsorption in Metal–Organic Frameworks. *Chem. Rev.* **2014**, *114* (20), 10575–10612.

(10) Ploetz, E.; Engelke, H.; Lächelt, U.; Wuttke, S. The Chemistry of Reticular Framework Nanoparticles: MOF, ZIF, and COF Materials. *Adv. Funct. Mater.* **2020**, *30* (41), 1909062.

(11) Jin, C.-X.; Shang, H.-B. Synthetic Methods, Properties and Controlling Roles of Synthetic Parameters of Zeolite Imidazole Framework-8: A Review. *J. Solid State Chem.* **2021**, *297*, 122040.

(12) Liang, W.; Ricco, R.; Maddigan, N. K.; Dickinson, R. P.; Xu, H.; Li, Q.; Sumby, C. J.; Bell, S. G.; Falcaro, P.; Doonan, C. J. Control of Structure Topology and Spatial Distribution of Biomacromolecules in Protein@ZIF-8 Biocomposites. *Chem. Mater.* **2018**, *30* (3), 1069–1077.

(13) Liu, G.; Xu, Y.; Han, Y.; Wu, J.; Xu, J.; Meng, H.; Zhang, X. Immobilization of Lysozyme Proteins on a Hierarchical Zeolitic Imidazolate Framework (ZIF-8). *Dalton Trans.* **2017**, *46* (7), 2114–2121.

(14) Lykourinou, V.; Chen, Y.; Wang, X.-S.; Meng, L.; Hoang, T.; Ming, L.-J.; Musselman, R. L.; Ma, S. Immobilization of MP-11 into a Mesoporous Metal–Organic Framework, MP-11@mesoMOF: A New Platform for Enzymatic Catalysis. *J. Am. Chem. Soc.* **2011**, *133* (27), 10382–10385.

(15) Chen, Y.; Han, S.; Li, X.; Zhang, Z.; Ma, S. Why Does Enzyme Not Leach from Metal–Organic Frameworks (MOFs)? Unveiling the Interactions between an Enzyme Molecule and a MOF. *Inorg. Chem.* **2014**, *53* (19), 10006–10008.

(16) Raja, D. S.; Liu, W.-L.; Huang, H.-Y.; Lin, C.-H. Immobilization of Protein on Nanoporous Metal-Organic Framework Materials. *Comments Inorg. Chem.* **2015**, *35* (6), 331–349.

(17) Doonan, C.; Ricco, R.; Liang, K.; Bradshaw, D.; Falcaro, P. Metal–Organic Frameworks at the Biointerface: Synthetic Strategies and Applications. *Acc. Chem. Res.* **2017**, *50* (6), 1423–1432.

(18) Chen, Y.; Lykourinou, V.; Vetromile, C.; Hoang, T.; Ming, L.-J.; Larsen, R. W.; Ma, S. How Can Proteins Enter the Interior of a MOF? Investigation of Cytochrome CTranslocation into a MOF Consisting of Mesoporous Cages with Microporous Windows. *J. Am. Chem. Soc.* **2012**, *134* (32), 13188–13191.

(19) Pan, Y.; Li, H.; Farmakes, J.; Xiao, F.; Chen, B.; Ma, S.; Yang, Z. How Do Enzymes Orient When Trapped on Metal–Organic Framework (MOF) Surfaces? *J. Am. Chem. Soc.* **2018**, *140* (47), 16032–16036.

(20) Zhao, M.; Xie, Y.; Chen, H.; Deng, C. Efficient Extraction of Low-Abundance Peptides from Digested Proteins and Simultaneous Exclusion of Large-Sized Proteins with Novel Hydrophilic Magnetic Zeolitic Imidazolate Frameworks. *Talanta* **2017**, *167*, 392–397.

(21) Vigderman, L.; Zubarev, E. R. High-Yield Synthesis of Gold Nanorods with Longitudinal SPR Peak Greater than 1200 Nm Using Hydroquinone as a Reducing Agent. *Chem. Mater.* **2013**, *25* (8), 1450–1457.

(22) Li, Y.; Jin, J.; Wang, D.; Lv, J.; Hou, K.; Liu, Y.; Chen, C.; Tang, Z. Coordination-Responsive Drug Release inside Gold Nanorod@metal-Organic Framework Core–Shell Nanostructures for near-Infrared-Induced Synergistic Chemo-Photothermal Therapy. *Nano Res.* **2018**, *11* (6), 3294–3305.

(23) Perrault, S. D.; Chan, W. C. W. Synthesis and Surface Modification of Highly Monodispersed, Spherical Gold Nanoparticles of 50−200 nm. *J. Am. Chem. Soc.* **2009**, *131* (47), 17042–17043.

(24) Zhao, X.; Fang, X.; Wu, B.; Zheng, L.; Zheng, N. Facile Synthesis of Size-Tunable ZIF-8 Nanocrystals Using Reverse Micelles as Nanoreactors. *Sci. China Chem.* **2013**, *57* (1), 141–146.

(25) Yang, F.; Mu, H.; Wang, C.; Xiang, L.; Yao, K. X.; Liu, L.; Yang, Y.; Han, Y.; Li, Y.; Pan, Y. Morphological Map of ZIF-8 Crystals with Five Distinctive Shapes: Feature of Filler in Mixed-Matrix Membranes on C_3H_6/C_3H_8 Separation. *Chem. Mater.* **2018**, *30* (10), 3467–3473.

(26) Tanaka, S.; Kida, K.; Okita, M.; Ito, Y.; Miyake, Y. Size-Controlled Synthesis of Zeolitic Imidazolate Framework-8 (ZIF-8) Crystals in an Aqueous System at Room Temperature. *Chem. Lett.* **2012**, *41* (10), 1337–1339.

(27) Gole, A.; Murphy, C. J. Polyelectrolyte-Coated Gold Nanorods: Synthesis, Characterization and Immobilization. *Chem. Mater.* **2005**, *17* (6), 1325–1330.

(28) Hauck, T. S.; Ghazani, A. A.; Chan, W. C. W. Assessing the Effect of Surface Chemistry on Gold Nanorod Uptake, Toxicity, and Gene Expression in Mammalian Cells. *Small* **2008**, *4* (1), 153–159.

(29) Burrows, N. D.; Lin, W.; Hinman, J. G.; Dennison, J. M.; Vartanian, A. M.; Abadeer, N. S.; Grzincic, E. M.; Jacob, L. M.; Li, J.; Murphy, C. J. Surface Chemistry of Gold Nanorods. *Langmuir* **2016**, *32* (39), 9905–9921.

(30) Hobday, C. L.; Woodall, C. H.; Lennox, M. J.; Frost, M.; Kamenev, K.; Düren, T.; Morrison, C. A.; Moggach, S. A. Understanding the Adsorption Process in ZIF-8 Using High Pressure Crystallography and Computational Modelling. *Nat. Commun.* **2018**, *9* (1), 1429.

(31) Osterrieth, J. W. M.; Wright, D.; Noh, H.; Kung, C.-W.; Vulpe, D.; Li, A.; Park, J. E.; Duyne, R. P. V.; Moghadam, P. Z.; Baumberg, J. J.; Farha, O. K.; Fairen-Jimenez, D. Core–Shell Gold Nanorod@Zirconium-Based Metal–Organic Framework Composites as in Situ Size-Selective Raman Probes. *J. Am. Chem. Soc.* **2019**, *141* (9), 3893–3900.

(32) Zeng, J.-Y.; Wang, X.-S.; Zhang, M.-K.; Li, Z.-H.; Gong, D.; Pan, P.; Huang, L.; Cheng, S.-X.; Cheng, H.; Zhang, X.-Z. Universal Porphyrinic Metal–Organic Framework Coating to Various Nanostructures for Functional Integration. *ACS Appl. Mater. Interfaces* **2017**, *9* (49), 43143–43153.

(33) Zheng, G.; Marchi, S. de; López-Puente, V.; Sentosun, K.; Polavarapu, L.; Pérez-Juste, I.; Hill, E. H.; Bals, S.; Liz-Marzán, L. M.; Pastoriza-Santos, I.; Pérez-Juste, J. Encapsulation of Single Plasmonic Nanoparticles within ZIF-8 and SERS Analysis of the MOF Flexibility. *Small* **2016**, *12* (29), 3935–3943.

(34) Hinman, J. G.; Turner, J. G.; Hofmann, D. M.; Murphy, C. J. Layer-by-Layer Synthesis of Conformal Metal–Organic Framework Shells on Gold Nanorods. *Chem. Mater.* **2018**, *30* (20), 7255–7261.

(35) Kupgan, G.; Liyana-Arachchi, T. P.; Colina, C. M. NLDFT Pore Size Distribution in Amorphous Microporous Materials. *Langmuir* **2017**, *33* (42), 11138–11145.

(36) Chen, Q.-Q.; Hou, R.-N.; Zhu, Y.-Z.; Wang, X.-T.; Zhang, H.; Zhang, Y.-J.; Zhang, L.; Tian, Z.-Q.; Li, J.-F. Au@ZIF-8 Core–Shell Nanoparticles as a SERS Substrate for Volatile Organic Compound Gas Detection. *Anal. Chem.* **2021**, *93* (19), 7188–7195.

CHAPTER 4: HOW PROTEINS ASSOCIATE WITH POROUS NANOSCALE SURFACES [3]

4.1 Abstract

It is well-known that colloidal nanomaterials, upon exposure to a complex biological medium, acquire biomolecules on their surface to form coronas. The protein corona is an important aspect in understanding the nano-bio interface, as it becomes the face of the nanoparticle to the biological environment. Porous nanomaterials present an opportunity to sequester biomolecules and/or control their orientation at the surface. In this report, a metal-organic framework (MOF) shell around gold nanorods was compared to MOF nanocrystals as potential protein sponges to adsorb several common proteins and potentially control their orientation at the surface. Even after correction for surface area, MOF shell/gold nanorod materials adsorbed more protein than the analogous nanoMOFs, a result that is hypothesized to be due to the higher surface roughness of the MOF shells compared to MOF nanocrystals. For the set of proteins and nanomaterials in this study, all protein-surface interactions were exothermic as judged by isothermal titration calorimetry. Protein display at the surfaces was determined from limited proteolysis experiments, and it was found that protein orientation was dependent on the nature of the nanoparticle surface.

[3] This chapter was reproduced from a manuscript in preparation for publication.

4.2 Introduction

There is increasing interest in nanoscale materials that have controllable nanoscale pores; thus, synthetic methods that describe materials composed of both metal-organic frameworks (MOFs) and nanoparticles have appeared recently.[1–4] These materials have applications in drug delivery, sensing, and catalysis.[5–10] MOFs themselves have a wide variety of applications including gas storage, separations, and catalysis due to their very high surface areas.[11,12] Among nanoparticle types, plasmonic nanoparticles are particularly interesting because of their optical properties. Gold nanoparticles have garnered much attention due to their ability to scatter light, produce local electric fields, and produce heat upon resonant illumination at visible and near-infrared plasmon band maxima.[13,14] In particular, gold nanorods (AuNRs) are well-known to produce tunable plasmons from ~500-1200 nm.[15–17] These properties make gold nanoparticles suitable materials for applications such as sensing and diagnostics, surface-enhanced spectroscopies, and photothermal therapeutics.[18–20]

With gold nanoparticles becoming more prevalent across many technological sectors, much research has focused on the biological and environmental fate of such materials.[21–23] A more complete understanding of how nanoparticles interact with individual biomolecules and cells will serve as a basis for understanding of the fate of these nanoparticles in entire organisms and ecosystems.[24,25] Furthermore, a deeper understanding of these biomolecular and cellular interactions will greatly improve the design of nanoparticles for therapeutics, imaging agents, and other biologically relevant applications.[26]

The first chemical step in understanding the nano-bio interface is to assess the adsorption of biomolecules to the nanoparticles; frequently the biomolecules are proteins, and thus the adsorbed proteins are called the protein coronas.[27–29] The chemical nature of the nanoparticle

surface would, intuitively, have influence over the biomolecular composition of the protein corona.[27,30] There have been reports in which porous materials sequester, or even control, the orientation of bound biomolecules.[31–34] Nanoscale MOFs and nanoparticles with MOF shells present unique materials that may lead to controllable protein orientations and hence coronas at the surfaces. MOFs have the advantages being crystalline materials with defined pore channels and pore sizes, and they are highly tunable structures.

In this report, the interactions of a set of standard proteins with AuNRs coated with the standard MOF ZIF-8 (AuNR@ZIF-8) was studied. The same biomolecular interactions were also studied with ZIF-8 nanoparticles (nanoZIF-8), to assess the similarities and differences of proteins binding to entirely porous nanoparticles versus a porous shell, in an effort to engineer protein coronas. The amount of protein adsorbed to each surface was quantified, as was the thermodynamics of adsorption by isothermal titration calorimetry. Limited proteolysis experiments were used to infer protein display on the nanoscale surface.

4.3 Materials and Methods

4.3.1 Materials and Instrumentation

2-methylimidazole (99%), zinc nitrate hexahydrate (98%), Brij® C10, ammonium bicarbonate (>99.5%), polyvinylpyrrolidone (PVP, 29k), β-lactoglobulin-A from bovine milk (BLG-A, >90%), lysozyme from chicken egg white (LYS), trypsin from bovine pancreas, chloroauric acid (99.9%), hydroquinone (99%), cetyltrimethylammonium bromide (CTAB, 99%), silver nitrate (99%), sodium citrate tribasic dihydrate, poly(diallyldimethylammonium chloride) solution (PDADMAC, 35 wt%), poly(sodium 4-styrenesulfonate) (PSS), poly(allylamine

hydrochloride) (PAH), and sodium borohydride (99%) were purchased from Sigma-Aldrich. Sodium hydroxide (ACS grade), and sodium chloride were purchased from Fisher Scientific. Bovine serum albumin was purchased from ChemCruz. Ethanol was purchased from Decon Laboratories Inc., cyclohexane and methanol were purchased from Macron Fine Chemicals. All chemicals were used without further purification. Deionized water was purified using a Barnstead Nanopure II purification system.

Dynamic light scattering (DLS) and ζ-potential were measured using a Malvern Zetasizer Nano ZS instrument. UV-vis spectra were obtained using a Cary 5000 UV–vis–near-infrared spectrophotometer. Isothermal titration calorimetry (ITC) measurements were done using a TA instruments Affinity ITC. Scanning electron microscopy (SEM) was performed on a Hitachi S4700 instrument. Transmission electron microscopy (TEM) was performed on a JEOL 2100 Cryo LaB_6 or a JEOL 2010 LaB_6 instrument operated at 200 kV. All sizing analysis was completed using ImageJ and a minimum of 300 nanoparticles was measured. Powder X-ray diffraction (XRD) was taken using a Bruker D8 Venture Duo instrument. Protein fragmentation results were obtained Thermo UltiMate 3000 UHPLC system coupled online to a high resolution Thermo Orbitrap Fusion Tribrid mass spectrometer.

4.3.2 Protein Quantification

The amount of protein adsorbed to the nanoparticles was determined using a Pierce BCA Protein Assay Kit. Briefly, 1 mL of 0.5 mg/mL nanoZIF-8 and 1 mL of 0.5 nM AuNR@ZIF-8 were added to multiple microcentrifuge tubes. Three tubes were used for each time point and for each protein to give an average and standard deviation. The nanoparticles were centrifuged at 4,000 rcf for 20 minutes and the supernatants were removed. To each pellet, 1 mL of 1 mg/mL protein

in a 0.1 mM NH_4HCO_3 solution was added. The tubes were mechanically shaken very gently for the desired amount of time (1, 5, 12, 24, and 48 hrs). At each time point, the corresponding tubes were removed from the mechanical shaker and the nanoparticles were then centrifuged at 4,000 rcf for 20 minutes. The supernatants were removed and saved for analysis with the colorimetric BCA assay. The BCA assay was done on the supernatants using the test-tube method with the standard protocol of 37 °C for 30 minutes. Each set of protein-nanoparticle pairs had a set of standards that was created from the same protein solution that was initially added to the nanoparticles. The amount of protein adsorbed to the nanoparticles was determined by subtracting the amount remaining in the supernatant from the total amount of protein added.

4.3.3 Limited Proteolysis

The procedure used for limited proteolysis experiments was adapted from a previous report.[35] For a typical experiment, 1 mL of 1 nM AuNPs (AuNR@ZIF-8, PDADMAC AuNRs, PAH AuNSs) and 1 mL of 1 mg/mL nanoZIF-8 were centrifuged and the pellets were redispersed in 1 mL of a 1 mg/mL protein solution. The nanoparticles were then incubated with protein overnight (>16 hrs). After incubation, the nanoparticles were washed twice with centrifugation to rid the sample of free protein, and redispersed in 0.1 mM NH_4HCO_3 each time. Next, the remaining protein adsorbed to the nanoparticles was digested by adding 50 μL of 0.050 mg/mL trypsin. The digestion was carried out for 12 hrs at 37 °C. The samples were then centrifuged to separate the nanoparticles from the digested protein fragments, the supernatants containing the protein fragments were removed and sent for mass spectrometry analysis using previously reported protocols.[36]

The digested material was lyophilized and dissolved in 5% acetonitrile containing 0.1%

formic acid before injection for LC/MS. For LC/MS, 2 μg of digested sample was used. The system used was a Thermo UltiMate 3000 UHPLC system coupled with a high resolution Thermo Orbitrap Fusion Tribid mass spectrometer. Peptides were separated by reversed-phase chromatography using a 15 cm Acclaim PepMap 100 C18 column with mobile phases of (A) 0.1% formic acid and (B) 0.1% formic acid in acetonitrile. A linear gradient from 4% B to 35% B over the course of 45 minutes was employed for peptide separation, followed by additional steps for column washing and regeneration. The mass spectrometer was operated in a data dependent manner in which precursor scans from 300 to 1500 m/z (120,000 resolution) were followed by collision induced dissociation of the most abundant precursors over a maximum cycle time of 3 s (35% NCE, 1.6 m/z isolation window, 60 s dynamic exclusion window). The raw LC-MS/MS data was analyz4ed against the Swissprot database using Mascot peptide and fragment mass tolerances were set to 10 ppm and 0.6 Da, respectively. Variable modifications included oxidation of methionine was added to the search against the Mouse database.

4.3.4 Isothermal Titration Calorimetry

ITC was done to evaluate protein-nanoparticle thermodynamics using optimized parameters.[43] Typical experiments consisted of 25 injections of 2.5 μL of 4 mM protein into a cell containing 300 μL of nanoparticles. Typical nanoparticle concentrations used were 1 nM of AuNR@ZIF-8 and 0.25 mg/mL of nanoZIF-8. The NanoAnalyze software was used to determine the change in enthalpy and dissociation constants, by fitting with either an independent or linear model depending on the quality of the titration curve.

4.4 Results and Discussion

Proteins can diffuse through porous structures; for instance, 60 kDa random-coil proteins, corresponding with a radius of gyration of around 3.5 nm, are able to diffuse through 5 nm nuclear pores.[37–39] In principle, an engineered nano-porous surface could promote a preferred protein orientation if partial insertion of a protein was achieved, and electrostatics or other factors were favorable. Colloidal nanocrystalline MOFs are excellent candidates to explore such interactions; the MOF chosen in these experiments, ZIF-8, has pore sizes of 1.2 nm and 0.34 nm.[40] It has been previously found that MOF shells can be grown on AuNRs.[2,8,9,41] The comparison of a porous shell to a fully porous nanoparticle may allow to control the degree of protein chain penetration into nanoscale pores, leading to engineered protein coronas on nanoscale surfaces.

The MOF chosen for the studies was ZIF-8, a well-studied MOF composed of 2-methylimidazole linkers and zinc(II) nodes.[42,43] One important factor in the choice of ZIF-8 is its aqueous stability.[44,45] The details of the synthesis and characterization can be found in Chapter 4. ZIF-8 nanoparticles were synthesized using a previously reported reverse micelle method.[46] The other porous nanoparticle of interest is one containing a ZIF-8 shell around a AuNR. The AuNRs were synthesized using the common seed-mediated, hydroquinone reduction method.[47] Using this method produced AuNRs with an aspect ratio of 3.7 and a longitudinal plasmon near 800 nm. The ZIF-8 coating of AuNRs was done according to a previously reported procedure.[9] The AuNR surface was first modified and coated with PVP. Once coated with PVP, methanol solutions containing 2-methylimadzole and $Zn(NO_3)$ were added. After 1 hour of continual stirring, individual AuNRs were coated with ZIF-8.

The proteins used for the experiments, were chosen based off of two main criteria, protein size and charge. The nanoZIF-8 and AuNR@ZIF-8 nanoparticles both exhibit positive ζ–potentials

in a 0.1 mM ammonium bicarbonate solution (pH = 7.1), nanoZIF-8 ζ–potential was 21.0 ± 0.9 mV and the AuNR@ZIF-8 ζ–potential was 17.2 ± 0.6 mV. For protein binding experiments, proteins that would be negatively charged at pH = 7.1 would be expected to associate reasonably well with these nanomaterials based on electrostatics. Table 4.1 summarizes the key protein characteristics of the three proteins being studied, β-lactoglobulin-A (BLG-A), lysozyme (LYS), and bovine serum albumin (BSA). BLG-A and BSA have similar isoelectric points and are negatively charged under the solution conditions (pH = 7.1), whereas LYS has an isoelectric point of 10.7 and is not electrostatically favored to bind to the nanomaterials. BLG-A and LYS are relatively small proteins with radii of gyration of 2.04 nm and 1.4 nm, respectively, which could in principle fit partially into the ZIF-8 micropores.[37,48] The larger BSA, with radius of gyration of 2.76 nm, would be expected to favor surface adsorption and not stick its "feet" into the ZIF-8 pores.[37]

Table 4.1: Characteristics of proteins in the study.

Protein	pI (Charge)	Size (kDa)	Size (nm)	Ref.
BLG-A	5.2 (-)	18.4	4.4 x 4.4	49,50
LYS	10.7 (+)	14.3	4.0 x 4.0	51,52
BSA	4.7 (-)	66.5	4 x 14	53

Initial experiments were done to ensure the nanoZIF-8 and AuNR@ZIF-8 stability in the ammonium bicarbonate solution and in the presence of the proteins. After being dispersed in 0.1 mM ammonium bicarbonate, powder XRD confirmed that the nanoZIF-8 particles maintained their structure. The stability of the AuNR@ZIF-8 was monitored with UV-vis spectroscopy to

monitor the plasmon band positions of the gold nanorod cores. The AuNR@ZIF-8 particles were stable in the presence of each protein, illustrated by the consistent plasmon peaks with minimal line broadening in the UV-vis spectra. The ζ-potential was also monitored, and the AuNR@ZIF-8 particles exhibit similar ζ-potentials to that of the free proteins after the proteins adsorbed to the surface.

The overall amount of protein adsorbed by the nanoparticles was determined using a colorimetric BCA assay, inferring amounts bound from total protein inputs and free protein found after separation from the nanoparticles. The amount of protein adsorbed was normalized by the total surface area of nanoparticles in solution; the resulting normalized protein adsorption amounts are shown in Figure 4.1A (nanoZIF-8) and 4.1B (AuNR@ZIF-8).

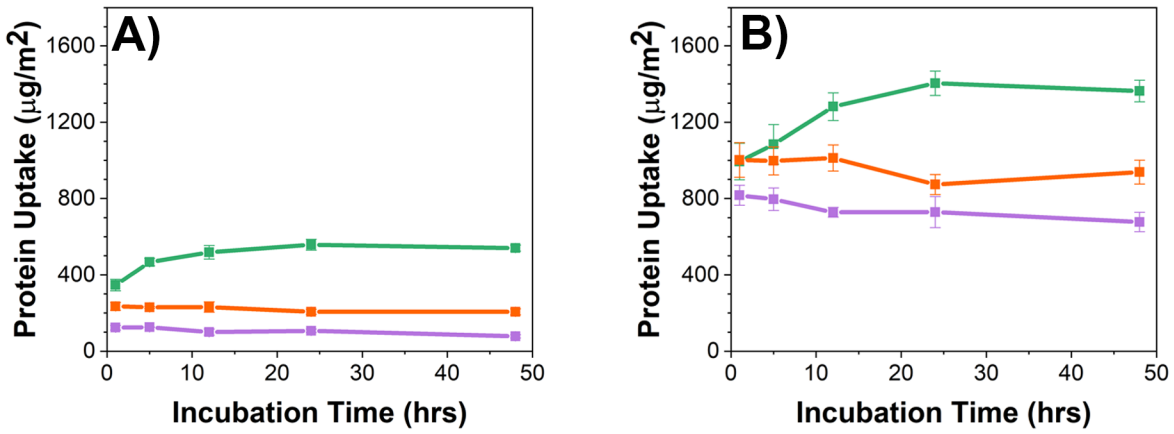

Figure 4.1: The amount of protein adsorbed as a function of time for (A) nanoZIF-8 and (B) AuNR@ZIF-8, normalized by the total nanoparticle surface area in solution. The nanoparticle concentrations were 1 mg/mL for nanoZIF-8 and 1 nM for AuNR@ZIF-8. (Green data: BLG-A, orange data: BSA, purple data: LYS).

The first major observable difference between the protein adsorption is that the

AuNR@ZIF-8 had a much higher amount of protein adsorbed per unit surface area compared to that of nanoZIF-8. As previously discussed, the pore size between the nanoZIF-8 and AuNR@ZIF-8 are very similar, so it is unlikely the increased protein adsorption for AuNR@ZIF-8 is a result of larger pores or any difference in pore structure. Instead, the hypothesis is that the increased protein adsorption is due to the increased surface roughness of the AuNR@ZIF-8 particles compared to the nanoZIF-8. Examination of the electron microscopy images, both TEM and SEM, show that the surface of the nanoZIF-8 is qualitatively smoother than the AuNR@ZIF-8 surface. Surface roughness has previously been shown to have a significant impact on the amount of protein adsorbed.[54,55] The higher surface roughness for AuNR@ZIF-8 would explain the increased adsorption for all three proteins studied. For both nanoparticle types, the degree of adsorption was BLG-A > BSA > LYS. This is an accord with expectations for favorable electrostatic adsorption of the three proteins to the cationic nanoparticle surfaces. BLG-A also had some time dependence to its adsorption, as there was an initial increase throughout the first 24 hours for both nanoparticle types, whereas both LYS and BSA showed no time dependence in the adsorption for either nanoparticle types.

Isothermal titration calorimetry was used to determine association constants and the change in enthalpy for each protein-nanoparticle pair. The titration curves for each protein titrated into nanoZIF-8 and AuNR@ZIF-8 are shown in Figure 4.2. The determined binding (association) constants K_a and ΔH from the titration curves are summarized in Table 4.2. The binding constants were generally larger for the AuNR@ZIF-8/protein complexes compared to that of the nanoZIF-8, indicating that the proteins bind more strongly to the ZIF-8 shell rather than the ZIF-8 nanoparticle. This may be due to the surface roughness of the ZIF-8 shell compared to that of the nanoZIF-8, creating more points of contact for the bound protein.[56,57] The protein affinity for the

surface for the ZIF-8 shell nanoparticles was BLG-A >> LYS ~ BSA, while that for the nanoZIF-8 was BLG-A >LYS ~ BSA. Clearly, the smallest anionic protein was the protein most likely to adsorb most tightly to either type of cationic nanoparticle. The ITC data also reveal the enthalpy of each pair of interactions (Table 4.2). The most notable feature of this data is the modest enthalpy of interaction of BLG-A for either nanoscale porous surface, suggesting that the interactions are driven by entropy (e.g., expulsion of water or counterions from the interface).[58]

Table 4.2: Summarized ITC results for each nanoparticle – protein pair.

Biomolecule	**NP type**	**K_d (M)**	**ΔH (kJ/mol)**
BLG-A	nanoZIF-8	2.8×10^5	-9.4
LYS	nanoZIF-8	6.2×10^3	-117
BSA	nanoZIF-8	1.5×10^3	-287
BLG-A	AuNR@ZIF-8	3.0×10^5	-10.5
LYS	AuNR@ZIF-8	3.5×10^4	-89
BSA	AuNR@ZIF-8	2.1×10^4	-78

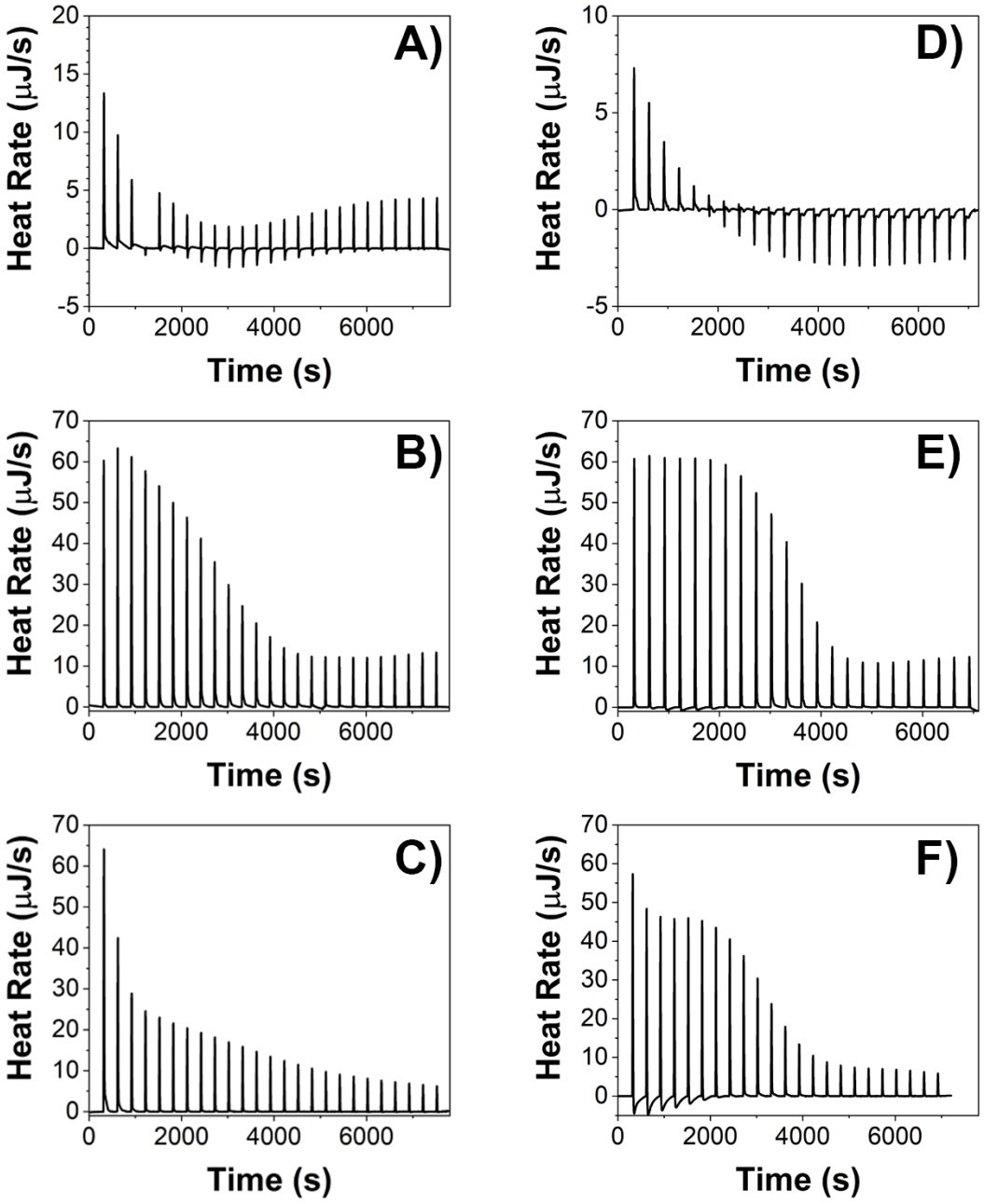

Figure 4.2: ITC curves for protein titrated into nanoparticles. Both the protein and the nanoparticles were n 0.1 mM NH_4HCO_3. (A) 4.0 μM BLG-A into 0.2 mg/mL nanoZIF-8 (B) 4.0 μM LYS into 0.2 mg/mL nanoZIF-8 (C) 4.0 μM BSA into 0.2 mg/mL nanoZIF-8 (D) 4.0 μM BLG-A into 1.0 nM AuNR@ZIF-8 (E) 4.0 μM LYS into 0.2 nM AuNR@ZIF-8 (F) 4.0 μM BSA into 0.5 nM AuNR@ZIF-8.

One interpretation of the BLG-A data is that it is likely to penetrate the pores of the nanoMOF surfaces, leading to release of more counterions/water from the pores compared to the surface. If this is the case, then it would be expected that portions of the protein would be sequestered from the environment. To test this hypothesis, limited proteolysis experiments were conducted in which proteins adsorbed to the nanoparticle surface were enzymatically digested followed by mass spectrometric analysis of the protein fragments. In these experiments, the nanoparticles were incubated with each protein for 16 hours, followed by centrifugation to remove any remaining free protein. Trypsin was then added to the resuspended pellet to digest the adsorbed proteins for 12 hours at 37 °C. As "soft shell" controls, polyelectrolyte-wrapped AuNSs and AuNRs with similar sizes and zeta potentials to that of the nanoZIF-8 and AuNR@ZIF-8 (Figure S13; the polyelectrolytes were poly(allylamine) hydrochloride (PAH) and poly(diallydimethylammonium) chloride (PDADMAC) were also used as substrates to measure protein protection from degradation and hence orientation.

Figures 4.3, 4.4, and 4.5 show the results for each of the four nanoparticle types and for the three proteins. The plots show the percent difference between the digestion patterns of each free protein and that of the adsorbed protein. Amino acids that are in positive percentage difference are more solvent exposed. Amino acids that are in a negative percentage difference are less solvent exposed. In Figure 4.3, the BLG-A digestion patterns show that the bound protein has its N-terminus more exposed to the solvent than free protein, independent of nanoparticle type. This result is in accord with the nature of the amino acids in the protein; the C-terminus does contain more negatively charged residues than the N-terminus and thus would be expected to be oriented closer to the cationic nanoparticle surfaces.[50] Electrostatics as the predominant factor controlling protein orientation has been previously observed.[59–62] However, these data neither refute nor

support the hypothesis that BLG-A's C terminus is sequestered in nanoscale pores.

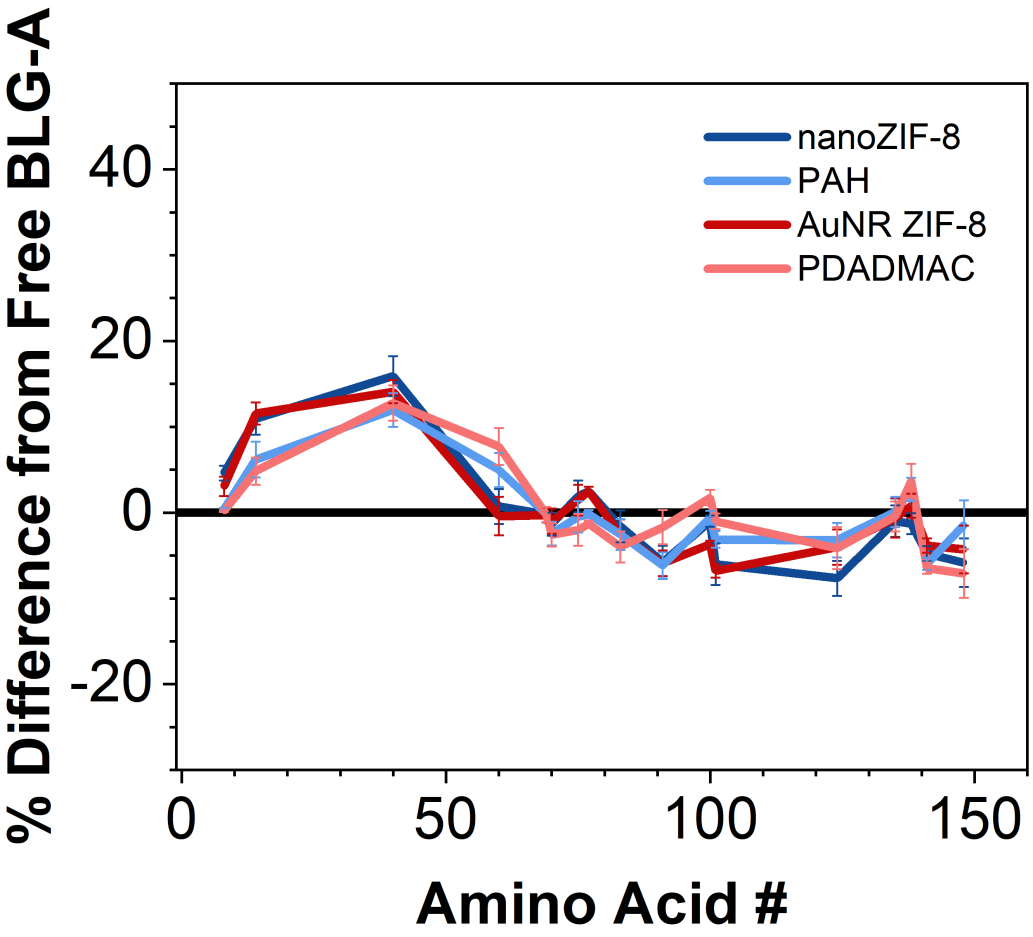

Figure 4.3: Percent difference between the protein digestion amounts of free BLG-A and the BLG-A adsorbed for each nanoparticle type. A positive percent difference corresponds to amino acid residues that are more solvent exposed, and a negative percent difference corresponds to being less solvent exposed. (dark red: AuNR@ZIF-8, light red: PDADMAC AuNRs, dark blue: nanoZIF-8, light blue: PAH AuNS).

The lysozyme results, Figure 4.4, show similar digestion patterns for each nanoparticle type (N-terminus more exposed, middle portion of protein protected from digestion) but the

AuNR@ZIF-8 sample showed significantly more proteolysis of the N-terminus of the bound protein and protection of the middle portion compared to other samples. This is similar to the conclusion drawn from a study that examined lysozyme orientation on larger ZIF-8 crystals using EPR; that group also determined the N-terminus was more exposed to the solvent whereas the C-terminus was more buried into the ZIF-8.[33] We attribute the C-terminus being less solvent exposed not to electrostatics (as the anionic amino acid residues in LYS are sparse and not clustered) but to the increased number of aromatic residues near the C-terminus that π-stack with the imidazole rings of the ZIF-8. Thus, π-stacking interactions are also a likely source of protein-NP interactions, should the surface of the NP provide a suitable chemical environment.

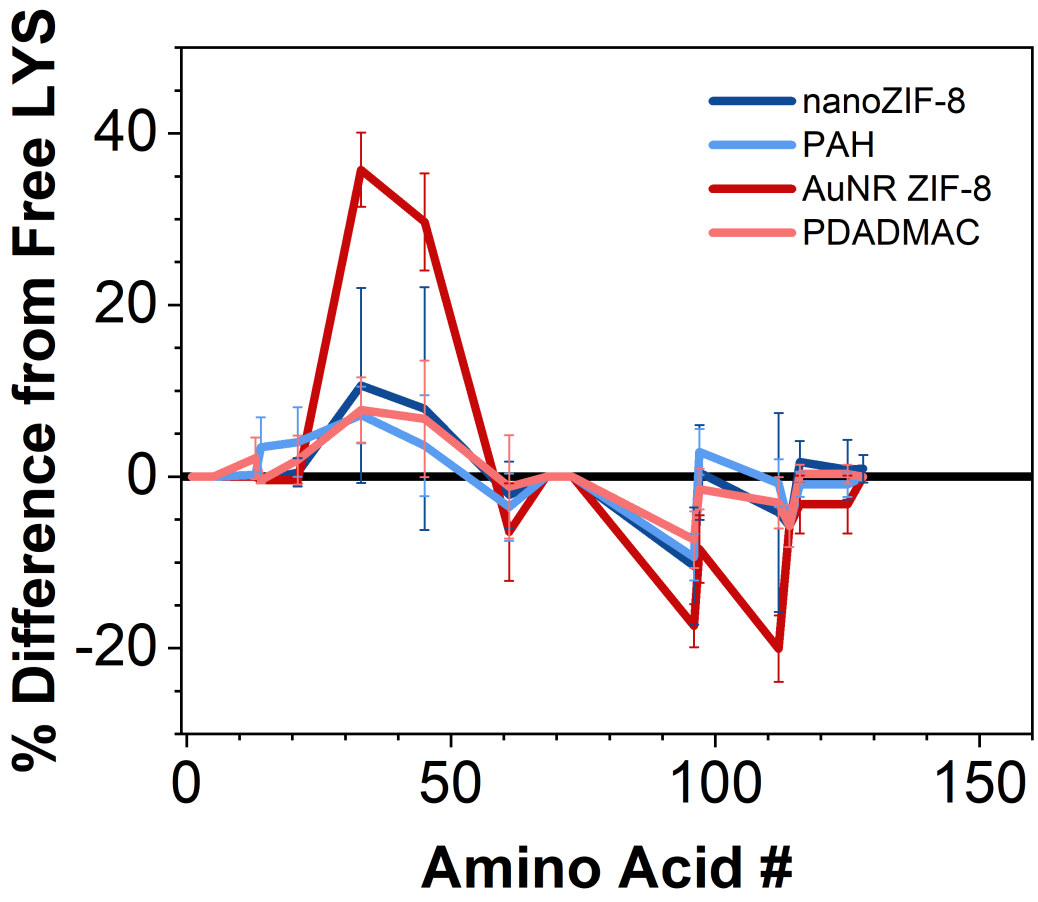

Figure 4.4: Percent difference between the protein digestion amounts of free LYS and the LYS adsorbed for each nanoparticle type. A positive percent difference corresponds to amino acid residues that are more solvent exposed, and a negative percent difference corresponds to being less solvent exposed. (dark red: AuNR@ZIF-8, light red: PDADMAC AuNRs, dark blue: nanoZIF-8, light blue: PAH AuNS).

In Figure 4.5, the results from the BSA digestion experiments show very similar patterns for all nanoparticle types tested and very little difference compared to free protein. These results indicate that BSA has no preferred orientation at any of the nanoparticle surfaces.

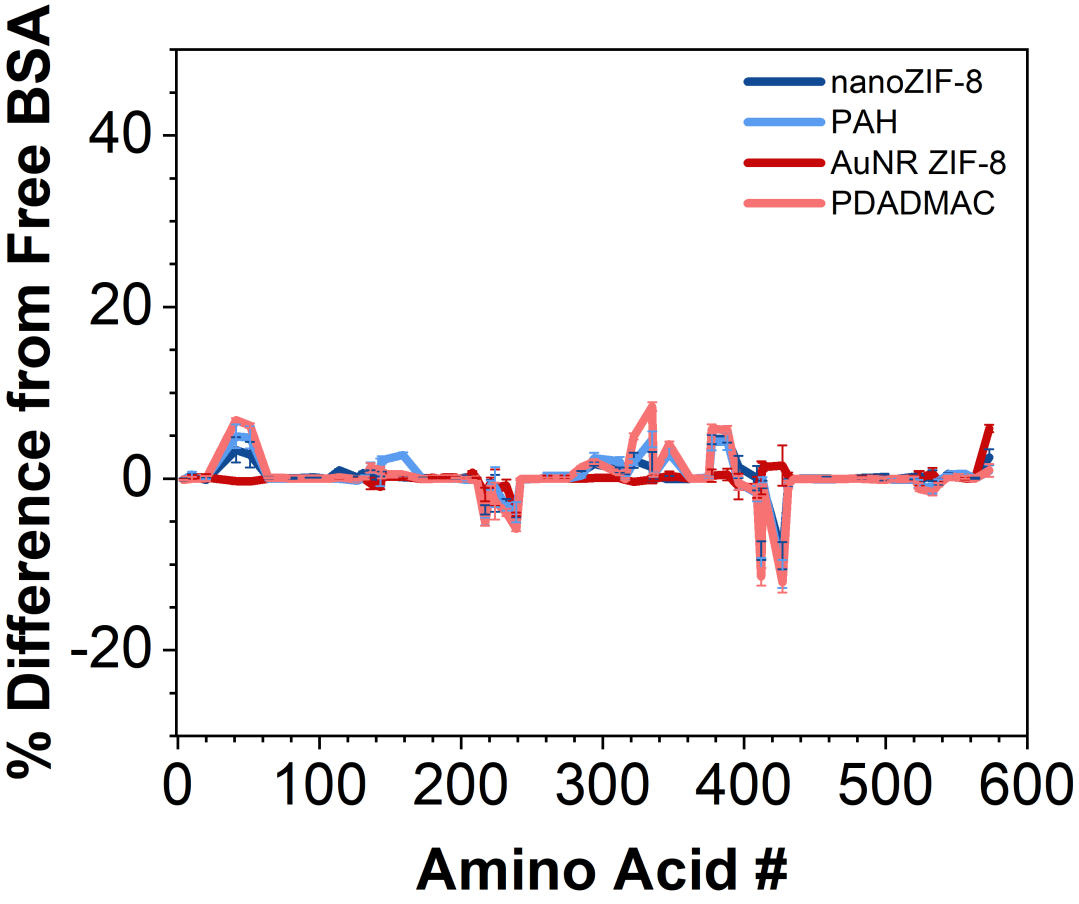

Figure 4.5: Percent difference between the protein digestion amounts of free BSA and the BSA adsorbed for each nanoparticle type. A positive percent difference corresponds to amino acid residues that are more solvent exposed, and a negative percent difference corresponds to being less solvent exposed. (dark red: AuNR@ZIF-8, light red: PDADMAC AuNRs, dark blue: nanoZIF-8, light blue: PAH AuNS).

In summary, the amount of protein that was adsorbed to the nanoparticle surfaces is largely predictable considering favorable electrostatic interactions, as more BLG-A and BSA was adsorbed to the surfaces than LYS. In a study looking at the immobilization of proteins on the

surface of larger ZIF-8 crystals with a hierarchical pore structure, they found the amount of protein adsorbed to the surface was solely based upon the size of the protein.[32] In their case, the presence of mesopores made it possible for lysozyme to penetrate the pores, thus leading to a higher adsorption amount. With the nanoZIF-8 and AuNR@ZIF-8 having only micropores, neither protein is small enough to fully penetrate the pores, thus the protein size is not the main factor contributing to the adsorption amount. In the case where neither protein can actually penetrate the pores, these results suggest that the protein charge is the main factor impacting the adsorption capacity.

The AuNR@ZIF-8 particles had more protein bound to their surfaces compared to the analogous nanoZIF-8 proteins for all three proteins studied; our hypothesis is that this increased adsorption is due to the increased surface roughness of the AuNR@ZIF-8. Interestingly, BLG-A was also the only protein studied that had a time dependence to its adsorption, showing that over the course of hours smaller proteins that have favorable electrostatic interactions may continually coat the surface of nanoparticles and may even have the propensity to replace other bound proteins.

Isothermal titration calorimetry data show that the BLG-A had the largest affinity for cationic surfaces, and all nanoparticle-protein pairs here showed exothermic behavior upon binding. Previous reports using ITC to determine ΔH with BSA and lysozyme on polyelectrolyte-wrapped AuNRs found similar values for lysozyme and PVS AuNRs. However, in this previous report the BSA AuNR interaction was endothermic, albeit for different polyelectrolytes than those used here.[61]

The protein display at the nanoparticle surface was unique for each protein examined. The current hypothesis is that smaller proteins that are electrostatically favorable, such as BLG-A, will orient themselves via the favorable electrostatic interactions regardless of the nanoparticle's

physical surface structure. If a smaller protein does not have an electrostatically favorable interaction with the surface, as was the case for LYS, then the physical surface structure of nanoparticles can induce a favored orientation at the surface, as was observed for the N-terminus being much more exposed when bound to the AuNR@ZIF-8 particles. For proteins that are much larger than the pore size, such as BSA, there is no preferred orientation, as the protein is too large to stick its "feet" into the pores. These results help shed light on the complexity of each protein-nanoparticle interaction and show that porous nanoparticles may be a route toward engineered protein coronas.

4.5 Conclusions

In this study, protein interactions at nanoscale metal-organic framework surfaces were evaluated. The nanoparticles of interest were ZIF-8 nanoparticles synthesized via a reverse micelle method, and ZIF-8 shells around AuNRs synthesized through a one-pot method. Of the three proteins investigated, the smallest protein that was also electrostatically favorable (BLG-A) had the most protein adsorbed to the surface of the nanoparticles, and the AuNR@ZIF-8 adsorbed a higher amount of protein than nanoZIF-8. The thermodynamics of each protein-nanoparticle pair were also similar in that they were all exothermic with association constants between 10^3 – 10^5. The orientation of the protein on the surface of the nanoparticles show that while electrostatics can govern the protein orientation, the hydrophobic and porous structure at the nanoparticle surface may control the protein orientation as well. In the future, using a MOF with a larger pore size, or functionalizing the pores of the MOF may induce even more specific protein orientations at the surface. These results will provide a baseline of comparison for future studies using porous nanomaterials to control and predict protein orientation.

4.6 References

(1) Chen, L.; Luque, R.; Li, Y. Controllable Design of Tunable Nanostructures inside Metal-Organic Frameworks. *Chem. Soc. Rev.* **2017**, *46*, 4614–4630.

(2) Zeng, J.-Y.; Wang, X.-S.; Zhang, M.-K.; Li, Z.-H.; Gong, D.; Pan, P.; Huang, L.; Cheng, S.-X.; Cheng, H.; Zhang, X.-Z. Universal Porphyrinic Metal–Organic Framework Coating to Various Nanostructures for Functional Integration. *ACS Appl. Mater. Interfaces* **2017**, *9* (49), 43143–43153.

(3) Rungtaweevoranit, B.; Zhao, Y.; Choi, K. M.; Yaghi, O. M. Cooperative Effects at the Interface of Nanocrystalline Metal–Organic Frameworks. *Nano Res.* **2016**, *9* (1), 47–58.

(4) Koh, C. S. L.; Sim, H. Y. F.; Leong, S. X.; Boong, S. K.; Chong, C.; Ling, X. Y. Plasmonic Nanoparticle-Metal–Organic Framework (NP–MOF) Nanohybrid Platforms for Emerging Plasmonic Applications. *ACS Mater. Lett.* **2021**, *3* (5), 557–573.

(5) Chen, Q.-Q.; Hou, R.-N.; Zhu, Y.-Z.; Wang, X.-T.; Zhang, H.; Zhang, Y.-J.; Zhang, L.; Tian, Z.-Q.; Li, J.-F. Au@ZIF-8 Core–Shell Nanoparticles as a SERS Substrate for Volatile Organic Compound Gas Detection. *Anal. Chem.* **2021**, *93* (19), 7188–7195.

(6) Zhao, Y.; Ni, X.; Ye, S.; Gu, Z.-G.; Li, Y.; Ngai, T. A Smart Route for Encapsulating Pd Nanoparticles into a ZIF-8 Hollow Microsphere and Their Superior Catalytic Properties. *Langmuir* **2020**, *36* (8), 2037–2043.

(7) Liu, Y.; Wang, S.; Lv, P.; Zhang, Y.; Zhao, Y.; Kong, X.; Zhang, J.; Guo, Z.; Xu, W.; Chen, X. Inserting Pt Nanoparticles at the Designated Location inside Metal− Organic Frameworks for Promoted Catalytic Performance. *Inorg. Chem.* **2020**, *59* (9), 6060–6066.

(8) Osterrieth, J. W. M.; Wright, D.; Noh, H.; Kung, C.-W.; Vulpe, D.; Li, A.; Park, J. E.; Duyne, R. P. V.; Moghadam, P. Z.; Baumberg, J. J.; Farha, O. K.; Fairen-Jimenez, D. Core–Shell Gold Nanorod@Zirconium-Based Metal–Organic Framework Composites as in Situ Size-Selective Raman Probes. *J. Am. Chem. Soc.* **2019**, *141* (9), 3893–3900.

(9) Li, Y.; Jin, J.; Wang, D.; Lv, J.; Hou, K.; Liu, Y.; Chen, C.; Tang, Z. Coordination-Responsive Drug Release inside Gold Nanorod@metal-Organic Framework Core–Shell Nanostructures for near-Infrared-Induced Synergistic Chemo-Photothermal Therapy. *Nano Res.* **2018**, *11* (6), 3294–3305.

(10) Zeng, J.-Y.; Zhang, M.-K.; Peng, M.-Y.; Gong, D.; Zhang, X.-Z. Porphyrinic Metal-Organic Frameworks Coated Gold Nanorods as a Versatile Nanoplatform for Combined Photodynamic/Photothermal/Chemotherapy of Tumor. *Adv. Funct. Mater.* **2017**, *28* (8), 1705451.

(11) Furukawa, H.; Cordova, K. E.; O'Keeffe, M.; Yaghi, O. M. The Chemistry and Applications of Metal-Organic Frameworks. *Science* **2013**, *341* (6149), 1230444.

(12) Hendon, C. H.; Rieth, A. J.; Korzyński, M. D.; Dincă, M. Grand Challenges and Future Opportunities for Metal–Organic Frameworks. *ACS Cent. Sci.* **2017**, *3* (6), 554–563.

(13) Chen, H.; Shao, L.; Li, Q.; Wang, J. Gold Nanorods and Their Plasmonic Properties. *Chem. Soc. Rev.* **2013**, *42* (7), 2679–2724.

(14) Chang, H.-H.; Gole, M. T.; Murphy, C. J. A Golden Time for Nanotechnology. *MRS Bull.* **2020**, *45* (5), 387–393. https://doi.org/10.1557/mrs.2020.119.

(15) Zhao, P.; Li, N.; Astruc, D. State of the Art in Gold Nanoparticle Synthesis. *Coord. Chem. Rev.* **2013**, *257*, 638–665.

(16) Sharma, V.; Park, K.; Srinivasarao, M. Colloidal Dispersion of Gold Nanorods: Historical Background, Optical Properties, Seed-Mediated Synthesis, Shape Separation and Self-Assembly. *Mater. Sci. Eng. R Rep.* **2009**, *65*, 1–38.

(17) Vigderman, L.; Khanal, B. P.; Zubarev, E. R. Functional Gold Nanorods: Synthesis, Self-Assembly, and Sensing Applications. *Adv. Mater.* **2012**, *24* (36), 4811–4841.

(18) Zhan, C.; Chen, X.-J.; Yi, J.; Li, J.-F.; Wu, D.-Y.; Tian, Z.-Q. From Plasmon-Enhanced Molecular Spectroscopy to Plasmon-Mediated Chemical Reactions. *Nat. Rev. Chem.* **2018**, *2*, 216–230.

(19) Huo, D.; Kim, M. J.; Lyu, Z.; Shi, Y.; Wiley, B. J.; Xia, Y. One-Dimensional Metal Nanostructures: From Colloidal Syntheses to Applications. *Chem. Rev.* **2019**, *119* (15), 8972–9073.

(20) Rastinehad, A. R.; Anastos, H.; Wajswol, E.; Winoker, J. S.; Sfakianos, J. P.; Doppalapudi, S. K.; Carrick, M. R.; Knauer, C. J.; Taouli, B.; Lewis, S. C.; Tewari, A. K.; Schwartz, J. A.; Canfield, S. E.; George, A. K.; West, J. L.; Halas, N. J. Gold Nanoshell-Localized Photothermal Ablation of Prostate Tumors in a Clinical Pilot Device Study. *Proc. Natl. Acad. Sci.* **2019**, *116* (37), 18590–18596.

(21) Albanese, A.; Tang, P. S.; Chan, W. C. W. The Effect of Nanoparticle Size, Shape, and Surface Chemistry on Biological Systems. *Annu. Rev. Biomed. Eng.* **2012**, *14*, 1–16.

(22) Murphy, C. J.; Chang, H.-H.; Falagan-Lotsch, P.; Gole, M. T.; Hofmann, D. M.; Hoang, K. N. L.; McClain, S. M.; Meyer, S. M.; Turner, J. G.; Unnikrishnan, M.; Wu, M.; Zhang, X.; Zhang, Y. Virus-Sized Gold Nanorods: Plasmonic Particles for Biology. *Acc. Chem. Res.* **2019**, *52* (8), 2124–2135.

(23) Alkilany, A. M.; Lohse, S. E.; Murphy, C. J. The Gold Standard: Gold Nanoparticle Libraries To Understand the Nano–Bio Interface. *Acc. Chem. Res.* **2012**, *46* (3), 650–661.

(24) Baimanov, D.; Cai, R.; Chen, C. Understanding the Chemical Nature of Nanoparticle–Protein Interactions. *Bioconjugate Chem.* **2019**, *30* (7), 1923–1937.

(25) Murphy, C. J.; Vartanian, A. M.; Geiger, F. M.; Hamers, R. J.; Pedersen, J.; Cui, Q.; Haynes, C. L.; Carlson, E. E.; Hernandez, R.; Klaper, R. D.; Orr, G.; Rosenzweig, Z. Biological Responses to Engineered Nanomaterials: Needs for the Next Decade. *ACS Cent. Sci.* **2015**, *1* (3), 117–123.

(26) Singh, N.; Marets, C.; Boudon, J.; Millot, N.; Saviot, L.; Maurizi, L. In Vivo Protein Corona on Nanoparticles: Does the Control of All Material Parameters Orient the Biological Behavior? *Nanoscale Adv.* **2021**, *3* (5), 1209–1229.

(27) Wolfram, J.; Yang, Y.; Shen, J.; Moten, A.; Chen, C.; Shen, H.; Ferrari, M.; Zhao, Y. The Nano-Plasma Interface: Implications of the Protein Corona. *Colloids Surf. B* **2014**, *124*, 17–24.

(28) Nguyen, V. H.; Lee, B.-J. Protein Corona: A New Approach for Nanomedicine Design. *Int. J. Nanomed.* **2017**, *12*, 3137–3151.

(29) Lundqvist, M.; Cedervall, T. Three Decades of Research about the Corona Around Nanoparticles: Lessons Learned and Where to Go Now. *Small* **2020**, *16* (46), 2000892.

(30) Zhang, Y.; Wu, J. L. Y.; Lazarovits, J.; Chan, W. C. W. An Analysis of the Binding Function and Structural Organization of the Protein Corona. *J. Am. Chem. Soc.* **2020**, *142*, 8827–8836.

(31) Doonan, C.; Ricco, R.; Liang, K.; Bradshaw, D.; Falcaro, P. Metal–Organic Frameworks at the Biointerface: Synthetic Strategies and Applications. *Acc. Chem. Res.* **2017**, *50* (6), 1423–1432.

(32) Liu, G.; Xu, Y.; Han, Y.; Wu, J.; Xu, J.; Meng, H.; Zhang, X. Immobilization of Lysozyme Proteins on a Hierarchical Zeolitic Imidazolate Framework (ZIF-8). *Dalton Trans.* **2017**, *46* (7), 2114–2121.

(33) Pan, Y.; Li, H.; Farmakes, J.; Xiao, F.; Chen, B.; Ma, S.; Yang, Z. How Do Enzymes Orient When Trapped on Metal–Organic Framework (MOF) Surfaces? *J. Am. Chem. Soc.* **2018**, *140* (47), 16032–16036.

(34) Schlipf, D. M.; Rankin, S. E.; Knutson, B. L. Pore-Size Dependent Protein Adsorption and Protection from Proteolytic Hydrolysis in Tailored Mesoporous Silica Particles. *ACS Appl. Mater. Interfaces* **2013**, *5* (20), 10111–10117.

(35) McClain, S. M.; Ojoawo, A. M.; Lin, W.; Rienstra, C. M.; Murphy, C. J. Interaction of Alpha-Synuclein and Its Mutants with Rigid Lipid Vesicle Mimics of Varying Surface Curvature. *ACS Nano* **2020**, *14* (8), 10153–10167.

(36) Rappsilber, J.; Mann, M.; Ishihama, Y. Protocol for Micro-Purification, Enrichment, Pre-Fractionation and Storage of Peptides for Proteomics Using StageTips. *Nat. Protoc.* **2007**, *2* (8), 1896–1906.

(37) Smilgies, D. M.; Folta-Stogniew, E. Molecular Weight–Gyration Radius Relation of Globular Proteins: A Comparison of Light Scattering, Small-Angle X-Ray Scattering and Structure-Based Data. *J. Appl. Crystallogr.* **2015**, *48* (5), 1604–1606.

(38) Hamman, B. D.; Chen, J.-C.; Johnson, E. E.; Johnson, A. E. The Aqueous Pore through the Translocon Has a Diameter of 40–60 Å during Cotranslational Protein Translocation at the ER Membrane. *Cell* **1997**, *89* (4), 535–544.

(39) Wang, R.; Brattain, M. G. The Maximal Size of Protein to Diffuse through the Nuclear Pore Is Larger than 60 KDa. *FEBS Lett.* **2007**, *581* (17), 3164–3170.

(40) Hobday, C. L.; Woodall, C. H.; Lennox, M. J.; Frost, M.; Kamenev, K.; Düren, T.; Morrison, C. A.; Moggach, S. A. Understanding the Adsorption Process in ZIF-8 Using High Pressure Crystallography and Computational Modelling. *Nat. Commun.* **2018**, *9* (1), 1429.

(41) Zheng, G.; Marchi, S. de; López-Puente, V.; Sentosun, K.; Polavarapu, L.; Pérez-Juste, I.; Hill, E. H.; Bals, S.; Liz-Marzán, L. M.; Pastoriza-Santos, I.; Pérez-Juste, J. Encapsulation of Single Plasmonic Nanoparticles within ZIF-8 and SERS Analysis of the MOF Flexibility. *Small* **2016**, *12* (29), 3935–3943.

(42) Chen, B.; Yang, Z.; Zhu, Y.; Xia, Y. Zeolitic Imidazolate Framework Materials: Recent Progress in Synthesis and Applications. *J. Mater. Chem. A* **2014**, *2* (40), 16811–16831.

(43) Jin, C.-X.; Shang, H.-B. Synthetic Methods, Properties and Controlling Roles of Synthetic Parameters of Zeolite Imidazole Framework-8: A Review. *J. Solid State Chem.* **2021**, *297*, 122040.

(44) Burtch, N. C.; Jasuja, H.; Walton, K. S. Water Stability and Adsorption in Metal–Organic Frameworks. *Chem. Rev.* **2014**, *114* (20), 10575–10612.

(45) Yuan, S.; Feng, L.; Wang, K.; Pang, J.; Bosch, M.; Lollar, C.; Sun, Y.; Qin, J.; Yang, X.; Zhang, P.; Wang, Q.; Zou, L.; Zhang, Y.; Zhang, L.; Fang, Y.; Li, J.; Zhou, H.-C. Stable Metal-Organic Frameworks: Design, Synthesis, and Applications. *Adv. Mater.* **2018**, *30* (37), 1704303.

(46) Zhao, X.; Fang, X.; Wu, B.; Zheng, L.; Zheng, N. Facile Synthesis of Size-Tunable ZIF-8 Nanocrystals Using Reverse Micelles as Nanoreactors. *Sci. China Chem.* **2013**, *57* (1), 141–146.

(47) Vigderman, L.; Zubarev, E. R. High-Yield Synthesis of Gold Nanorods with Longitudinal SPR Peak Greater than 1200 nm Using Hydroquinone as a Reducing Agent. *Chem. Mater.* **2013**, *25* (8), 1450–1457.

(48) Krigbaum, W. R.; Kugler, F. R. Molecular Conformation of Egg-White Lysozyme and Bovine. *Biochemistry* **1970**, *9* (5), 1216–1223.

(49) Parker, R.; Noel, T. R.; Brownsey, G. J.; Laos, K.; Ring, S. G. The Nonequilibrium Phase and Glass Transition Behavior of β-Lactoglobulin. *Biophys. J.* **2005**, *89* (2), 1227–1236.

(50) Kontopidis, G.; Holt, C.; Sawyer, L. Invited Review: β-Lactoglobulin: Binding Properties, Structure, and Function. *J. Dairy Sci.* **2004**, *87* (4), 785–796.

(51) Vilcacundo, R.; Méndez, P.; Reyes, W.; Romero, H.; Pinto, A.; Carrillo, W. Antibacterial Activity of Hen Egg White Lysozyme Denatured by Thermal and Chemical Treatments. *Sci. Pharm.* **2018**, *86* (4), 48.

(52) Parmar, A. S.; Muschol, M. Hydration and Hydrodynamic Interactions of Lysozyme: Effects of Chaotropic versus Kosmotropic Ions. *Biophys. J.* **2009**, *97* (2), 590–598.

(53) Su, T. J.; Lu, J. R.; Thomas, R. K.; Cui, Z. F. Effect of PH on the Adsorption of Bovine Serum Albumin at the Silica/Water Interface Studied by Neutron Reflection. *J. Phys. Chem. B* **1999**, *103* (18), 3727–3736.

(54) Rechendorff, K.; Hovgaard, M. B.; Foss, M.; Zhdanov, V. P.; Besenbacher, F. Enhancement of Protein Adsorption Induced by Surface Roughness. *Langmuir* **2006**, *22* (26), 10885–10888.

(55) Scopelliti, P. E.; Borgonovo, A.; Indrieri, M.; Giorgetti, L.; Bongiorno, G.; Carbone, R.; Podestà, A.; Milani, P. The Effect of Surface Nanometre-Scale Morphology on Protein Adsorption. *Plos One* **2010**, *5* (7), e11862.

(56) Bacakova, L.; Filova, E.; Parizek, M.; Ruml, T.; Svorcik, V. Modulation of Cell Adhesion, Proliferation and Differentiation on Materials Designed for Body Implants. *Biotechnol. Adv.* **2011**, *29* (6), 739–767.

(57) Donaldson, S. H.; Valtiner, M.; Gebbie, M. A.; Harada, J.; Israelachvili, J. N. Interactions and Visualization of Bio-Mimetic Membrane Detachment at Smooth and Nano-Rough Gold Electrode Surfaces. *Soft Matter* **2013**, *9* (21), 5231–5238.

(58) Prozeller, D.; Morsbach, S.; Landfester, K. Isothermal Titration Calorimetry as a Complementary Method for Investigating Nanoparticle–Protein Interactions. *Nanoscale* **2019**, *11* (41), 19265–19273.

(59) Lin, W.; Insley, T.; Tuttle, M. D.; Zhu, L.; Berthold, D. A.; Král, P.; Rienstra, C. M.; Murphy, C. J. Control of Protein Orientation on Gold Nanoparticles. *J. Phys. Chem. C* **2015**, *119* (36), 21035–21043.

(60) Dennison, J. M.; Zupancic, J. M.; Lin, W.; Dwyer, J. H.; Murphy, C. J. Protein Adsorption to Charged Gold Nanospheres as a Function of Protein Deformability. *Langmuir* **2017**, *33* (31), 7751–7761.

(61) Yang, J.; Wang, B.; You, Y.; Chang, W.-J.; Tang, K.; Wang, Y.-C.; Zhang, W.; Ding, F.; Gunasekaran, S. Probing the Modulated Formation of Gold Nanoparticles–Beta-Lactoglobulin Corona Complexes and Their Applications. *Nanoscale* **2017**, *9* (45), 17758–17769.

(62) Chen, K.; Xu, Y.; Rana, S.; Miranda, O. R.; Dubin, P. L.; Rotello, V. M.; Sun, L.; Guo, X. Electrostatic Selectivity in Protein–Nanoparticle Interactions. *Biomacromolecules* **2011**, *12* (7), 2552–2561.

CHAPTER 5: GOLD NANOROD IMPACT ON MECHANICAL PROPERTIES OF STRETCHABLE HYDROGELS [4]

5.1 Abstract

Double-network hydrogels have attracted much attention because of their superior mechanical properties, which are more similar to rubbers and soft tissues than classic hydrogels. In this report, plasmonic gold nanorods (AuNRs) are incorporated into a stretchable double-network hydrogel, composed of alginate and acrylamide. The impact of gold nanorod concentration and surface chemistry on bulk mechanical properties such as Young's modulus and elongation at break was investigated. AuNRs with three different surface chemistries, cetyltrimethylammonium bromide, thiolated poly(ethylene glycol), and 11-mercaptoundecanoic acid were successfully dispersed into alginate/polyacrylamide hydrogels. The AuNR-loaded hydrogels could be reversibly stretched, leading to AuNR reversible alignment along the stretch direction as judged by polarized optical spectroscopy. With the proper surface chemistry, hydrogel nanorod composites were able to be stretched to more than 3,000% their initial length without fracturing. These results show that plasmonic gold nanorods can be well dispersed in multi-component polymer systems, certain surface chemistries can enhance the bulk mechanical properties, and AuNR orientation can be controlled through varying strains on the matrix.

[4] Adapted and reprinted with permission from Turner, J. G.; Og, J. H.; Murphy, C. J. Gold nanorod impact on mechanical properties of stretchable hydrogels. *Soft Matter* **2020**, 16, 6582-6590.

5.2 Introduction

In the last 15 years, hydrogels have become extensively studied materials because of their biocompatibility, stimuli-responsiveness, and swelling/deswelling properties, among others.[1–3] Hydrogels are soft materials that consist of three-dimensional crosslinked polymer networks dispersed in high amounts of water (above 50 wt%) useful for waste treatment, tissue engineering, biosensing, and show promise in areas such as wearable electronics.[2,4–8] More recent advances in engineering hydrogels have been made to further enhance their properties and make them extremely tough, conductive, and/or self-healable.[1,8–12] Among these advanced hydrogels, double-network hydrogels have shown extraordinary mechanical properties making them ideal materials for tissue engineering and flexible electronics.[3] These mechanical properties include high fracture energies, high stretchability, and high modulus, all of which are comparable to that of tendons, ligaments, and rubbers.[1,3]

Adding nanomaterials as fillers to polymer composites to enhance materials is common practice. The auto-industry has added nanoparticle clays to strengthen materials for decades.[13] Nanomaterials such as ZnO nanorods, carbon nanotubes, and gold nanoparticles have been successfully dispersed into polyurethanes to provide advanced properties such as conductivity and shape-memory.[14–16] Control over nanoparticle orientation and assembly in polymer composites is challenging, especially in multi-polymer systems.[13] It has been shown that gold nanorod (AuNR) alignment can be controlled by the strain of stretchable materials, these examples embed or disperse the AuNRs in polymer films.[17–21] Understanding how nanoparticles behave in multi-polymer 3D systems is not well understood. In particular, the behavior of nanorods in 3D polymer networks is not as well studied as nanospheres and nanowires. Understanding the impact of

anisotropic nanoparticle fillers on double network hydrogels will be important for future material development.

Many hydrogels have nanomaterials incorporated into them (nanocomposite hydrogels) to help make them conductive, reinforce the mechanical properties, or make them antibacterial.[22–25] Plasmonic nanoparticles are of particular interest because of their strong light absorption and scattering. Among plasmonic nanoparticles, gold nanorods (AuNRs) are unique because their longitudinal plasmon can be tuned from the visible portion of the electromagnetic spectrum to the near-infrared by changing the aspect ratio of the AuNR.[26,27] Previously, gold nanoparticles have been incorporated into hydrogels for protein detection, as an extra-cellular matrix mimic, drug delivery, cardiac tissue engineering, and to give hydrogels optical and thermal responsiveness.[28–36] Stretchable plasmonic materials have been created, but the stretchable substrate is often an elastomer which lacks the biocompatibility and stimuli-responsiveness of hydrogels.[37–39] Stretchable hydrogels present a unique opportunity to create biocompatible stretchable plasmonics that can be used for wearable electronics, bio-sensors, and optical devices. Another advantage of hydrogels is their dispersion medium is water, so a variety of NP surface chemistries can be introduced into the pre-gel solution. Therefore, advanced surface modifications to make the AuNRs well dispersed is not necessary as in other polymer composites.[21,40]

In this report, AuNR hydrogel composites were synthesized where the hydrogel matrix is a double network with alginate and acrylamide (AAm), which itself can be stretched reversibly to more than twenty-times its initial length.[10,41] The Na-alginate/PAAm hydrogels can be ionically crosslinked with Ca^{2+} to yield a much tougher hydrogel compared to Na-alginate/PAAm hydrogel.[10,41] The AuNRs were incorporated into the pre-gel solution and stayed well dispersed throughout the curing process. The Na-alginate/polyacrylamide (PAAm) stretchable hydrogels

align the AuNRs along the stretch direction when elongated. Because the AuNRs were incorporated into the pre-gel solution before polymerization and crosslinking, the influence of AuNR surface chemistry and concentration have on the mechanical properties of these hydrogels was also studied. These properties were investigated as a function of surface chemistry for three different common surface chemistries for AuNRs: cetyltrimethylammonium bromide (CTAB), thiolated poly(ethylene glycol) (PEG-SH), and 11-mercaptoundecanoic acid (MUA). For the non-ionically crosslinked hydrogels (Na-alginate/PAAm) the Young's modulus is dependent on AuNR concentration, but for ionically crosslinked hydrogels (Ca-alginate/PAAm) the Young's modulus is dependent on AuNR concentration and surface chemistry.

5.3 Materials and Methods

5.3.1 Materials and Instrumentation

Chloroauric acid ($HAuCl_4 \cdot 3H_2O$, 99.9%), cetyltrimethylammonium bromide (CTAB, 99%), silver nitrate ($AgNO_3$, 99%), hydroquinone (99%), sodium borohydride ($NaBH_4$, 99%), 11-mercaptoundecanoic acid (MUA, 95%), sodium alginate, acrylamide (98%), ammonium persulfate (APS, 98%), N,N'-methylenebisacrylamide (MBAA, 99.5%), N,N,N',N'-tetramethylethylenediamine (TEMED, 99%) were purchased from Sigma-Aldrich. Sodium hydroxide (NaOH, 98%) was purchased from Fisher Scientific. Thiolated poly(ethylene glycol) (PEG-SH, M.W. 5,000) was purchased from NANOCS. Ethanol (200 proof) was purchased from Decon Laboratories Inc. and used without purification. All water used was DI water purified by a Barnstead Nanopure II purification system (>17.8 MΩ).

Transmission electron microscopy (TEM) of AuNRs was performed using a JEOL 2010 LaB_6 or JEOL 2100 Cryo LaB_6. TEM of hydrogels was done using a Hitachi Hg00 microscope. All nanorod sizing was done using ImageJ and a minimum of 300 nanorods were measured. A Nicolet Nexus 670 spectrometer equipped with a germanium crystal plate was used for ATR-FTIR measurements. Zeta potentials were measured using a Malvern Zetasizer Nano ZS instrument. All Young's modulus results were obtained using a Q800 Dynamic Mechanical Analyzer (DMA). Maximum elongation tensile testing measurements were done using a 1 kN MTS Insight 2 with a 250 N load cell. UV-vis spectra were obtained using a Cary 5000 UV–vis–near-infrared spectrophotometer. For polarized measurements a 5 mm circular aperture was used, along with a Glan-Thompson polarizer.

5.3.2 Synthesis of Gold Nanorods

Gold nanorods were prepared using a seed-mediated method with hydroquinone as the reducing agent.[42] To synthesize the CTAB-capped gold seeds a vial was prepared with 9.5 mL of 0.10 M CTAB and 0.5 mL of 0.10 M $HAuCl_4 \cdot 3H_2O$ was added. While this seed solution was stirred vigorously, 0.460 mL of freshly prepared, ice-cold $NaBH_4$ in 0.010 M NaOH was injected rapidly into the seed solution. The seed solution color became dark brown immediately following the addition of $NaBH_4$. The seeds were aged at room temperature without stirring for 1 hour before use. To prepare enough seeds for the typical 1 L AuNR growth solution, two identical batches of seeds were made. For a 1 L batch of AuNRs, a growth solution was prepared by adding 950 mL of 0.10 M CTAB to a large flask, followed by the addition of 1.30 mL of 0.10 M $AgNO_3$ and 50 mL of 0.010 M $HAuCl_4$, with gentle stirring. Then, 50 mL of 0.10 M hydroquinone was added; the solution was stirred until it was nearly colorless. Next, 16 mL of CTAB-capped gold seeds (aged

for 1-4 hours) was added to the growth solution, which was then stored at 27° C with mild stirring for 12-18 hours. The AuNRs were purified by centrifugation at 8,000 rcf for 20 min. The supernatants were discarded and the AuNR pellets were redispersed in nanopure water and stored at room temperature for future use. For a typical synthesis the AuNRs had an aspect ratio of 3.1 ± 0.4, with a length of 82 ± 8 nm and a width of 27 ± 3 nm.

5.3.3 Gold Nanorod Surface Modifications

Three surface chemistries were studied: CTAB, PEG-SH, and MUA. The procedure used for this surface modifications were adapted from a previous report.[43] The as synthesized gold nanorods are CTAB-capped and they were used after one additional wash by centrifugation at 8,000 rcf. To exchange the CTAB with PEG-SH, 1 mL of 50 mg/mL PEG-SH was added to 40 mL of 1 nM CTAB capped AuNRS (twice centrifuged). The AuNRs were then gently shaken overnight using a mechanical shaker and then purified by two rounds of centrifugation at 8,000 rcf for 30 minutes. These PEG-SH modified AuNRs can be further functionalized by replacing the thiolated polymer with shorter chain thiols, such as MUA.[44] For this process, 2 mL of 0.10 M NaOH were added to 40 mL 1 nM PEG-SH modified AuNRs and then 4 mL of 20 mM MUA dissolved in ethanol was subsequently added. The AuNRs were gently shaken overnight on a mechanical shaker and were then washed twice with water and centrifugation at 8,000 rcf for 30 minutes. The 2 mL of 0.10 M NaOH was added back in after each wash to ensure stability.

5.3.4 Synthesis of Alginate/Acrylamide Hydrogels with and without Gold Nanorods

To synthesize our dual network hydrogels we adopted a procedure from Suo and co-workers.[10,41] First, a series of stock solutions were prepared. A stock solution of 1:6 wt ratio of

alginate to acrylamide was prepared by dissolving 2.325 g of alginate and 13.953 g of acrylamide in 80 mL of nanopure water (83.1 wt%, stirred overnight to dissolve). An ammonium persulfate stock solution was prepared by dissolving 0.0237 g of ammonium persulfate in 5.0 mL of nanopure water. A N,N'-methylenebisacrylamide stock solution was prepared by dissolving 0.0167 g in 10 mL of nanopure water. Once the stock solutions were prepared, they were mixed together in amounts dependent on the total water content desired, where the total water content ultimately controls the hydrogel thickness.

For a typical hydrogel synthesis, our total water content was 6.25 mL. To synthesize the hydrogels, 5.0 mL of the alginate/acrylamide stock solution was added to a small beaker and it was stirred. Then 0.625 mL of additional nanopure water was added, followed by the addition of 0.3125 mL of MBAA (acrylamide crosslinker), 0.3125 mL of APS (thermo-initiator), and 2.81 μL of TEMED (crosslinking accelerator). The resulting solution was stirred for 10 minutes before being poured into our glass mold (60 x 15 mm glass petri dish). The petri dish was covered and placed in a drying oven at 70° C for 1 hour to cure. Once cured the glass mold was removed from the oven and placed in a humid box. The above amounts lead to the desired hydrogel with 86 wt% water, 2 wt% alginate, and 12 wt% acrylamide. Relative to acrylamide monomer the amount of MBAA, APS, and TEMED were 0.028 mol%, 0.053 mol%, and 0.153 mol%, respectively. ATR-FTIR was used to structurally characterize the resulting hydrogel, shown in Figure 5.1.

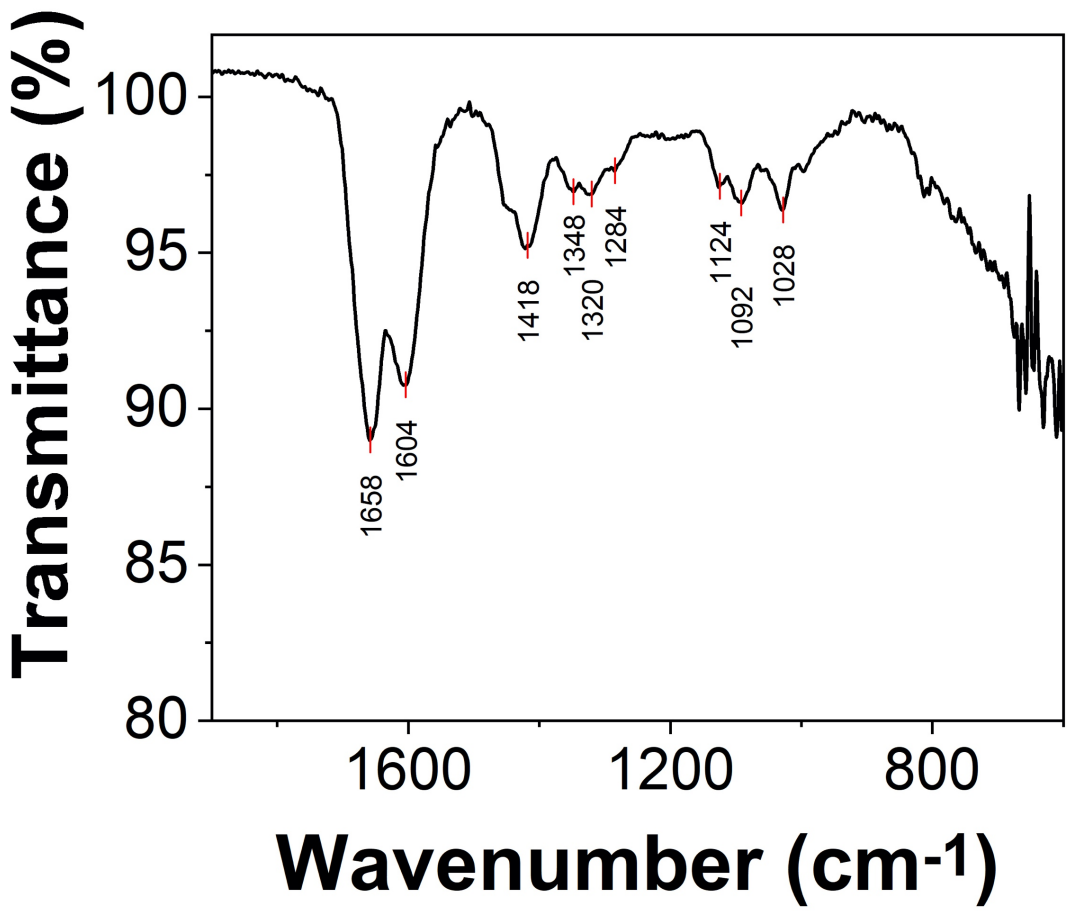

Figure 5.1: ATR-FTIR of Na-alginate/PAAm hydrogel. Sample was prepared by lyophilizing hydrogel and then grinding into a powder. Peak at 1284 cm^{-1} is the C-N stretching of the secondary amide formed between the alginate chains and polyacrylamide. (1658 cm^{-1}: C = O stretching, 1604 cm^{-1}: N-H deformation, 1418 cm^{-1}: C-N stretching, 1348 cm^{-1}: C-H deformation, 1320 cm^{-1}: C-H deformation, 1124 cm^{-1}: NH2 in-plane rocking, 1092 cm^{-1}: C-O stretching, 1028 cm^{-1}: C-O stretching).

The protocol used for synthesizing hydrogels with AuNRs is the same procedure outlined above, except instead of adding 0.625 mL of nanopure water, 0.625 mL of a AuNR solution was added, which leads to a 10-fold dilution of the AuNRs. For example, if 0.625 mL of 10 nM CTAB-capped AuNRs were added, the resulting hydrogel would have 1 nM of CTAB-capped AuNRs incorporated into its network, or about 0.03 wt%. Photographs of representative as synthesized hydrogels are shown in Figure 5.2.

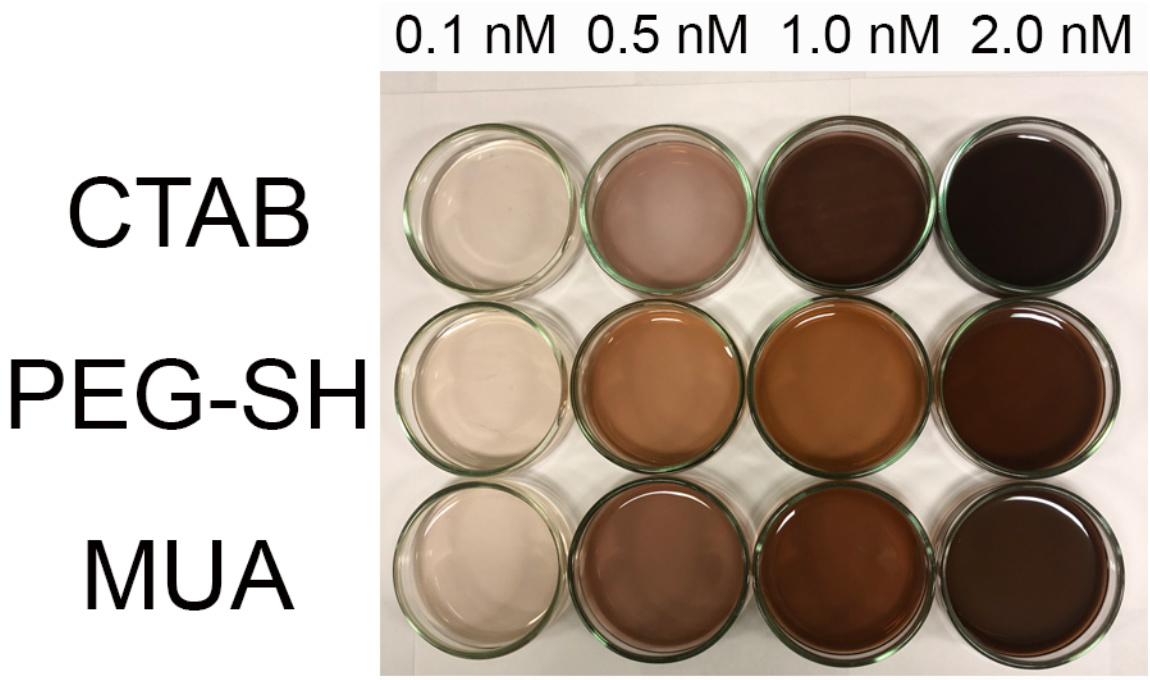

Figure 5.2: Photograph of a representative batch of synthesized Na-alginate/PAAm hydrogels with AuNRs.

5.3.5 Ca^{2+} Crosslinking of Alginate

To crosslink the alginate polymers, we followed a procedure by Suo and co-workers where they describe the strengthening of alginate/acrylamide hydrogels through multivalent cation exchange.[41] We used $CaCl_2$ as the source of Ca^{2+} to strengthen our hydrogels by first carefully removing the hydrogels from the glass petri dish and placing them in a 100 x 15 mm plastic petri dish. Then 30 mL of 0.3 M $CaCl_2$ was added to fully submerge the hydrogels in the solution, and the hydrogels were soaked for 3 hours. Afterwards the $CaCl_2$ was poured out, the hydrogels were rinsed off, and placed back into a humid box.

5.3.6 Mechanical Testing

The as synthesized, circular hydrogels had to be cut into pieces that could be used for mechanical testing. Each hydrogel had four or five rectangular pieces cut out of it all with the approximate dimensions of 40.0 mm long, 7.0 mm wide, and 2.0 mm thick. The hydrogel samples were kept in a humid box except for when they were being cut, measured, and tested.

To determine the Young's modulus these hydrogel pieces were tested using a Q800 DMA with a preload force of 0.0005 N and a ramp rate of 0.04 N/min. The initial gage length was measured by the instrument and each sample was stretched to 100-200% strain. The linear portion of 0-10% strain was then used to determine the Young's modulus of each sample.

A 1 kN MTS Insight 2 was used to determine the maximum elongation length because DMA has a limited achievable displacement. For these measurements the preload force was 0.01 N and the stretch rate was 100 mm/min. The initial gage length for each sample was manually measured before the test was started. The instrument does not consider the cross-sectional area of the sample when reporting stretch length, so the stretch axis was normalized to reflect the small

differences in cross-sectional areas between samples. This graph was then used to calculate the maximum elongation length for each sample, where the maximum elongation length is the point at which the hydrogel fractured or reached the maximum instrument displacement.

5.3.7 Polarized UV-vis Measurements

Polarized UV-vis measurements were performed to determine if the AuNRs aligned when stretched. For the setup of these measurements a polarizer was inserted between the light source and the sample. The hydrogel sample was then attached to a 5 mm circular aperture by taping it down, either unstretched or stretched a certain degree. In order to isolate the AuNR extinction spectra and eliminate other contributing sources of absorbance, a baseline was first taken with just the aperture inserted and no sample. Polarized measurements were taken with a hydrogel that was not loaded with AuNRs, the spectra obtained from these measurements were then subtracted with the corresponding polarization angle of their hydrogel counterpart that was loaded with AuNRs. Images of the experimental setup are shown in Figure 5.3.

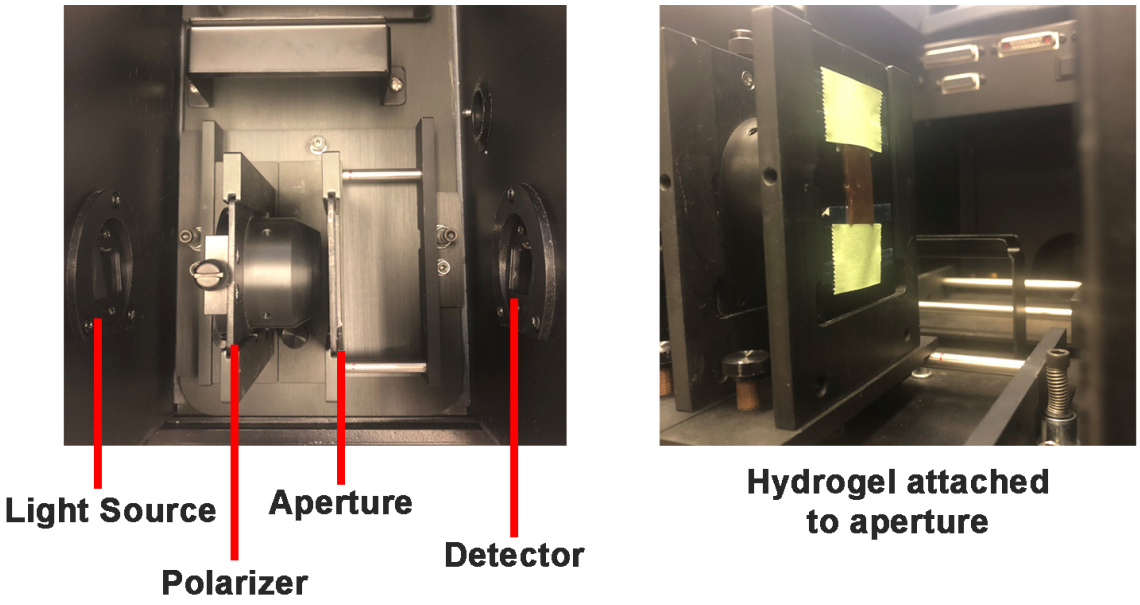

Figure 5.3: Measurement setup for UV-vis polarization measurements. Polarizer was placed between the light source and the aperture; the hydrogel was attached to the aperture plate in a stretched or unstretched position such that the hydrogel samples was completely covering the aperture.

5.3.8 TEM of Hydrogels Containing AuNRs

Small pieces of the hydrogel were cut and placed into a petri dish, either stretched or unstretched. They were then exposed to osmium tetroxide vapors for 1.5 hrs. The samples were dehydrated in 10-minute ethanol dispersions with increasing concentrations (50%, 75%, 95%, and 100%). The 100% ethanol step was lengthened to overnight and then to 2 days at 4 °C. With the hydrogel now harder, it was cut into smaller pieces using a razor blade. The unstretched samples were cubed and the stretched samples were cut into thin slices to maintain the stretch direction. Thee samples were then infiltrated with LR White resin with a short acetonitrile rinse step between the ethanol series and the resin. The resin infiltration was done overnight at room temperature. The

blocks were then hardened at 60 °C for 3 days. The resin does not harden when exposed to air, so a silicon embedding mold was used and an Aclar sheet was placed over hole openings to make the mold air tight. The resulting blocks were trimmed and sectioned into samples with 100-150 nm thickness using a diamond knife. The samples were then imaged with a Hitachi H600 electron microscope using an accelerating voltage of 75 kV.

5.4. Results and Discussion

5.4.1 Preparation of Stretchable Plasmonic Hydrogels

The alginate/PAAm hydrogel matrix was chosen because of its stretchiness and relative ease of synthesis in aqueous solution, making it compatible for the incorporation of water-dispersible nanoparticle fillers, such as AuNRs. The hydrogels were synthesized according to the procedure outline by Yang and co-workers, with only slight modifications to incorporate AuNRs into the matrix.[10,41] Stock solutions were prepared of each reagent: alginate and acrylamide, N,N'-methylenebisacrylamide (MBAA, crosslinker), ammonium persulfate (APS, initiator), and N,N,N',N'-tetramethylethylenediamine (TEMED, accelerator). These stock solutions were all prepared in slightly higher concentrations than desired for the final hydrogel; therefore, additional water was added before curing to yield the desired hydrogel that was 86 wt% water, 2 wt% alginate, and 12 wt% acrylamide. AuNRs were incorporated by replacing the added water with a solution containing AuNRs in the pre-gel solution. An illustration of the synthesis process is shown in Figure 5.4.

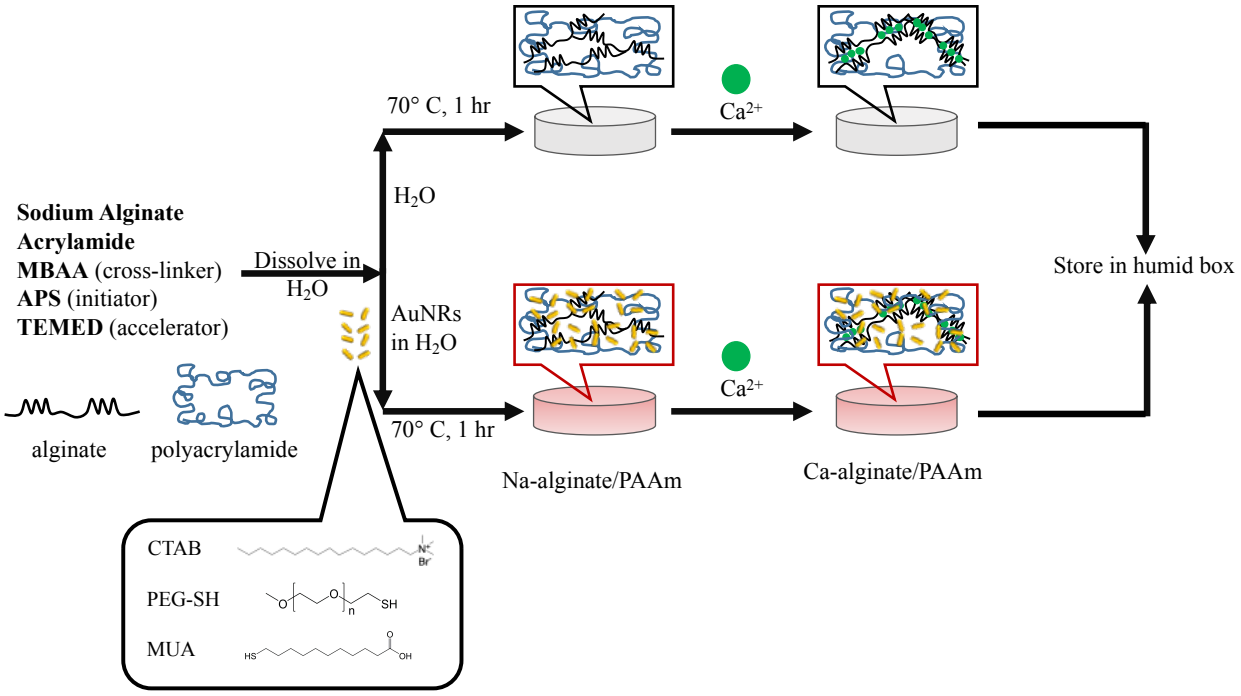

Figure 5.4: Illustration of the synthesis of Na-alginate/PAAm and Ca-alginate/PAAm hydrogels with and without gold nanorods (figure not drawn to scale). The gold nanorods were incorporated into the pre-gel mixture and stay well dispersed throughout the curing and polymerization processes. The chemical structures of the three surface chemistries used are depicted. Hydrogels were stored in a humid box until they were used for testing.

The AuNRs used in these experiments were synthesized by the method developed by Zubarev and co-workers.[42] The AuNRs had a longitudinal plasmon near 800 nm, with an aspect ratio of about 3. These were chosen because the plasmon is in the NIR window, and the length of the AuNRs is around 80 nm. Four different concentrations of AuNRs were studied; the hydrogels were synthesized so the concentration of AuNRs inside each hydrogel was 0.1 nM (about 0.003 wt%), 0.5 nM (about 0.015 wt%), 1.0 nM (about 0.03 wt%), and 2.0 nM (about 0.06 wt%). These

concentrations were chosen because they give the hydrogels an optical density that is suitable for absorbance based spectroscopic measurements.

To strengthen the hydrogels, divalent and trivalent cations can be used to cross-link the alginate chains.[41] As the dispersion of nanomaterials into a polymer matrix is affected by nanomaterial surface chemistry, three different surface chemistries were studied: CTAB, which forms a bilayer on the gold nanorod surface and yields a net positively-charged surface coating in aqueous solution, PEG-SH, which leads to near-neutral surfaces, and MUA, which yields a net negatively-charged surface coating in aqueous solution.[26,44,45] All surface chemistries produced hydrogel composite materials in which the AuNRs were well-dispersed, unlike other pairings of AuNRs in various polymers.[40] A comparison of the AuNR solution UV-vis and the UV-vis spectra of the AuNRs dispersed in hydrogels is shown in Figure 5.5. The spectra of the AuNRs in the hydrogel are slightly red-shifted and broadened compared to the solution spectra of the AuNRs. This indicates a small degree of aggregation, whereas far more significant broadening and red-shifting would be expected for a large amount aggregation.

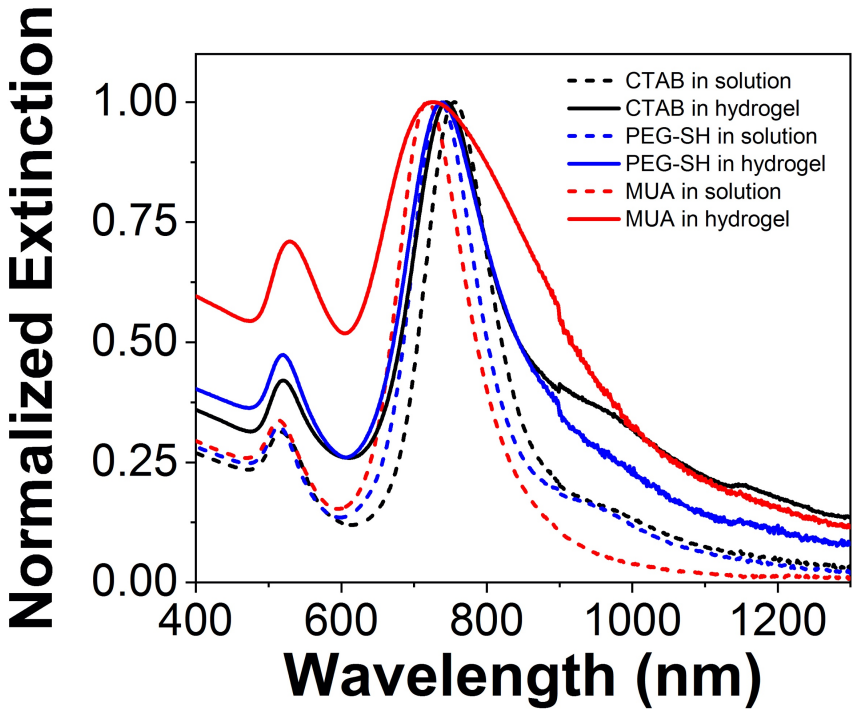

Figure 5.5: Normalized UV-vis spectra of AuNRs with differing surface chemistry in solution (dotted lines) and in a Na-alginate/PAAm hydrogel (solid lines).

5.4.2 Mechanical Properties of Stretchable Plasmonic Hydrogels

For mechanical testing, the synthesized hydrogels were cut into rectangular pieces measuring around 40.0 mm long, 7.0 mm wide, and 2.0 mm thick. Dynamic mechanical analysis (DMA) was used to determine the Young's modulus of each hydrogel. The Young's modulus, or linear tensile modules was determined from the initial slope of the stress versus strain curve in the 0-10% strain region. For the testing, at least 2 replicate hydrogels were tested with a minimum of 4 individual rectangular test samples cut from each hydrogel.

The average Young's modulus obtained for the Na-alginate/PAAm hydrogels is shown in Figure 5.6. The modulus was only dependent on AuNR concentration for the Na-alginate/PAAm

hydrogels; the surface chemistry of the AuNRs did not impact the modulus results as seen in Figure 5.6A. The averaged stress versus strain curves of the Na-alginate/PAAm for the MUA AuNR hydrogels is shown in Figure 5.6B, where the solid lines represent the average curve and the dashed lines are the standard deviation in that average.

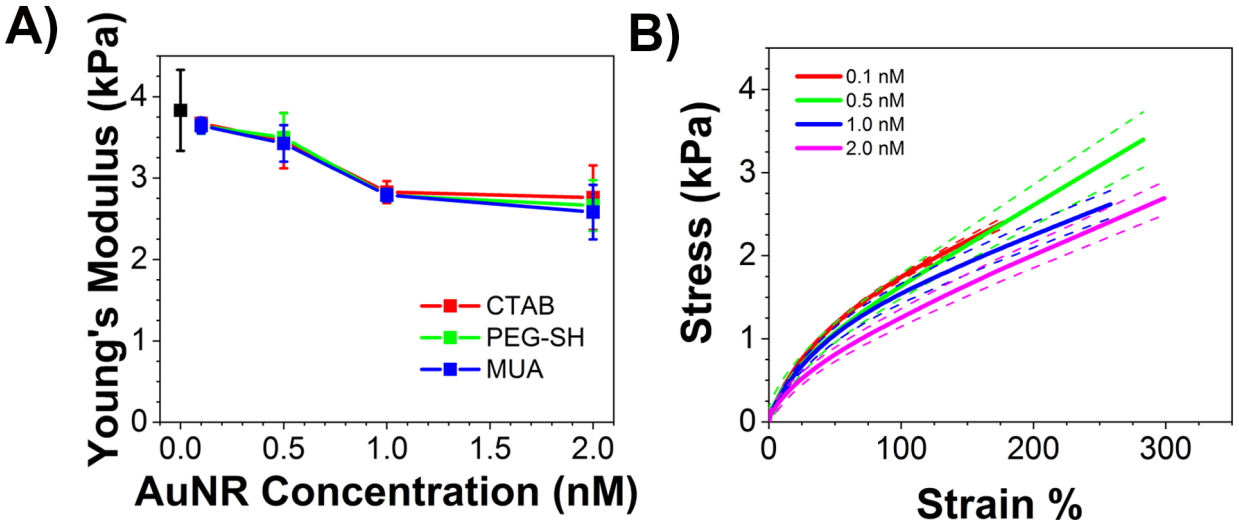

Figure 5.6: DMA results for Na-alginate/PAAm hydrogels with and without AuNRs of varied concentrations and surface chemistries. (A) Average Young's modulus results for each AuNR concentration and surface chemistry. (B) Averaged stress versus strain curves for MUA AuNR Na-alginate/PAAm hydrogels. The solid line is the average of multiple curves and the dotted lines are the standard error in the average curve.

Comparing the concentrations of just one surface chemistry (PEG-SH), at low concentrations (0.1 nM and 0.5 nM) the modulus is 3.64 ± 0.09 kPa and 3.5 ± 0.3 kPa. Compared to the modulus of the hydrogels without AuNRs, 3.8 ± 0.5 kPa the PEG-SH modulus values are not significantly different ($p > 0.05$). However, at higher concentrations of AuNRs (1.0 nM and

2.0 nM), the modulus decreased to 2.79 ± 0.5 kPa and 2.6 ± 0.3 kPa. This decrease in modulus is more than 25% and is statistically significantly lower ($p < 0.05$) than the hydrogels without AuNRs and the hydrogels with low concentrations of AuNRs. This same trend is observed for both CTAB and MUA AuNRs as well. The full tabular results of the Na-alginate/PAAm Young's modulus values, their standard deviations, and their statistical significance can be found in Table 5.1 and Table 5.2.

Table 5.1: Summary of Na-alginate/PAAM hydrogel mechanical testing results for each type of AuNR hydrogel synthesized. The Young's modulus and elongation results for the hydrogel without AuNRs was comparable to what was previously reported.

AuNR Surface Chemistry	AuNR Concentration (nM)	Young's Modulus (kPa)	Maximum Elongation %
N/A	0.0	3.83 ± 0.50	2,040 ± 310
CTAB	0.1	3.67 ± 0.05	2,153 ± 560
CTAB	0.5	3.46 ± 0.34	1,600 ± 620
CTAB	1.0	2.83 ± 0.14	2,130 ± 480
CTAB	2.0	2.76 ± 0.40	2,200 ± 460
PEG-SH	0.1	3.64 ± 0.09	1,950 ± 590
PEG-SH	0.5	3.50 ± 0.30	1,270 ± 240
PEG-SH	1.0	2.79 ± 0.05	2,710 ± 690
PEG-SH	2.0	2.66 ± 0.31	2,130 ± 500
MUA	0.1	3.64 ± 0.10	3,545 ± 350
MUA	0.5	3.43 ± 0.22	3,051 ± 770
MUA	1.0	2.79 ± 0.08	3,567 ± 730
MUA	2.0	2.58 ± 0.33	2,675 ± 210

Table 5.2: Calculated p-values to determine statistical significance between the Young's modulus values of various AuNR concentrations for each surface chemistry tested. The p-values are listed in the table with colors (green) corresponding to a statistically significant difference and (red) corresponding to not statistically different.

CTAB	0.1 nM	0.5 nM	1.0 nM	2.0 nM
0.0 nM	0.4905	0.0718	0.0003	0.0003
0.1 nM		0.2042	0.0001	0.0010
0.5 nM			0.0025	0.0061
1.0 nM				0.7215

PEG-SH	0.1 nM	0.5 nM	1.0 nM	2.0 nM
0.0 nM	0.4660	0.0997	0.0020	0.0010
0.1 nM		0.3924	0.0001	0.0005
0.5 nM			0.0003	0.0005
1.0 nM				0.3817

MUA	0.1 nM	0.5 nM	1.0 nM	2.0 nM
0.0 nM	0.4158	0.0425	0.0002	0.0001
0.1 nM		0.0726	0.0001	0.0001
0.5 nM			0.0001	0.0001
1.0 nM				0.1857

Nanoparticles often show very little impact on Young's modulus in polymer composites, or will even increase the modulus.[46,47] The AuNRs occupy a large amount of space and are incorporated before polymerization, the decrease in modulus is likely a result of the AuNR concentration reaching a point where it starts to impact the crosslinking density of acrylamide.[24,48] As the AuNR are concentrated enough to impede the density of acrylamide crosslinks, the material becomes less stiff, thus the modulus is lowered.

The DMA measurement is limited in its axial displacement, so it is not capable of stretching these hydrogels far enough to fracture them. To determine the maximum elongation length of hydrogels containing AuNRs, a tensile strength instrument (1 kN MTS Insight 2) was used, equipped with a 250 N load cell. With this instrument the hydrogels could be stretched far enough to determine the elongation amount before fracture. Due to the slight differences in sample size, the elongation amount was normalized by the cross-sectional area of each sample to give the most accurate comparison of results, these results are shown in Figure 5.7. The maximum elongation corresponds to how far the hydrogel was stretched before fracture or, in the case of many of the

MUA AuNR hydrogels, because it reached the maximum displacement of the instrument. The values and statistical significance of the maximum elongation can be found in Table 5.1. For these results we observe the maximum elongation length achievable does have some dependence on AuNR surface chemistry. AuNRs with CTAB and PEG-SH and no significant difference in their elongation amount compared to the hydrogels without AuNRs ($p > 0.05$). However, the MUA AuNRs significantly enhanced the hydrogels ability to stretch, even at low AuNR concentration. Hydrogel samples with MUA AuNRs did not fracture before reaching the maximum displacement of the tensile instrument, more than 3,500% their initial length. It is surprising the nanorod surface chemistry makes such a measurable difference in mechanical properties of the nanocomposites. We posit that this is a result of both the hard nature of the nanorods compares to the hydrogel matrix as well as electrostatic interactions between the anionic MUA surface groups and the sodium cation crosslinking groups. Similar impact on mechanical properties have been shown for hydrogels with anionic cellulose nanocrystals.[49] These results indicate the influence surface chemistry of nanoparticle fillers can have on bulk hydrogel properties, such as their mechanical properties. Consideration of nanoparticle shape, size, and surface chemistry are important considerations for future applications.

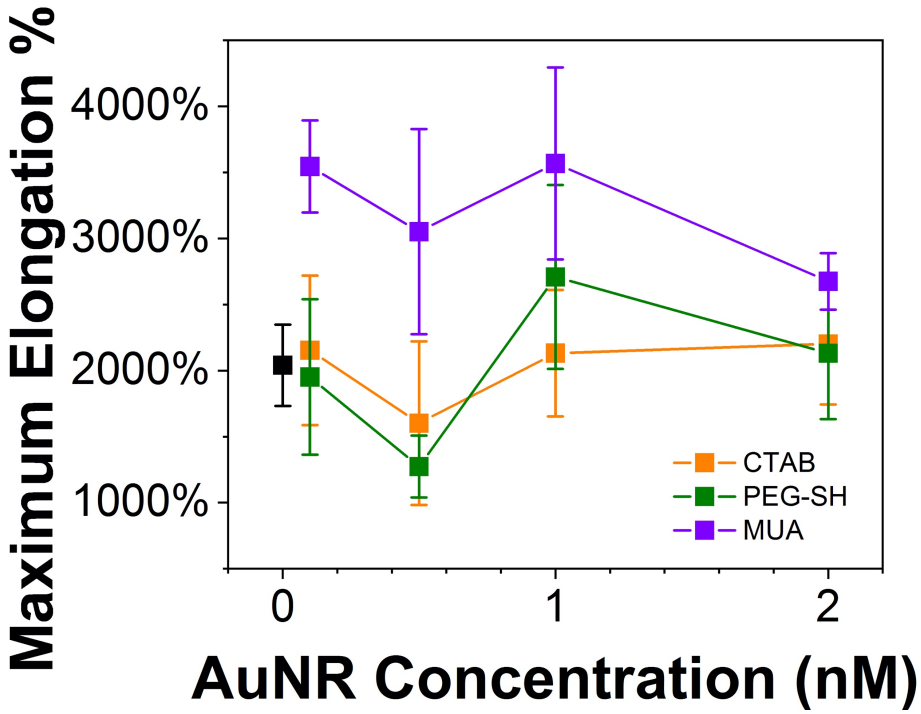

Figure 5.7: Maximum elongation results for each AuNR concentration and surface chemistry. The maximum elongation percentage is the percentage the hydrogel sample was stretched compared to its initial length before the sample fracture or reached the maximum displacement of the instrument (about 4000%).

Interestingly, when the hydrogels were ionically crosslinked with calcium, the AuNR surface chemistry impacts the modulus results as well as the AuNR concentration (Figure 5.8). The surface chemistry of the AuNR does not have a significant impact at low concentrations. For all of the 0.1 nM hydrogel samples there was no significant difference between them and then the hydrogel without AuNRs ($p > 0.05$). When the concentration of AuNRs in the hydrogels is increased to 1.0 nM, the Young's modulus for the CTAB AuNR hydrogel decreases significantly ($p < 0.05$). The average of the MUA AuNR hydrogel changes very slightly, but with much more

sample consistency, the MUA Young's modulus is statistically higher than the hydrogel without AuNRs ($p < 0.05$). The average Young's modulus values and standard deviation can be found in Table 5.3. Elongation studies for the Ca-alginate/PAAm hydrogels with AuNRs were difficult to execute due to substantial necking in the hydrogel while stretching.

This result can be rationalized by considering the crosslinking chemistry: divalent calcium ions crosslink the acid groups in the alginate chains. The addition of an acid-containing AuNR ought to act as another "chain" in the hydrogel that can participate in the crosslinking, thus increasing the Young's modulus. In contrast, a larger dose of cationic CTAB-containing AuNRs to the hydrogel might interfere with the calcium-alginate crosslinks, if the quaternary ammonium group of CTAB ion-pairs with the alginate acid groups. This could explain why the higher loadings of CTAB-AuNRs in the hydrogels decreases the Young's modulus.

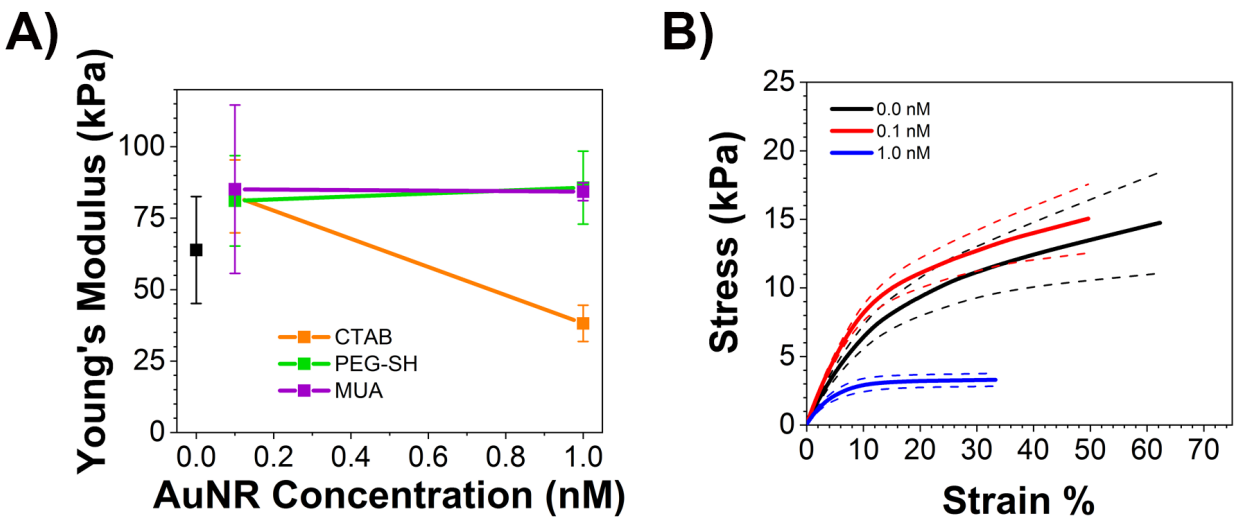

Figure 5.8: DMA results for Ca-alginate/PAAm hydrogels with and without AuNRs of varied concentrations and surface chemistries. (A) Average Young's modulus results for each AuNR concentration and surface chemistry. (B) Averaged stress versus strain curves for CTAB AuNR Ca-alginate/ PAAm hydrogels. The solid line is the average of multiple curves and the dotted lines are the standard error in the average curve.

Table 5.3: Young's modulus values for Ca-alginate/PAAm hydrogels. *Denotes values that are statistically different ($p < 0.05$) than the hydrogel sample without AuNRs.

AuNR Surface Chemistry	AuNR Concentration (nM)	Young's Modulus (kPa)
N/A	0.0	64 ± 19
CTAB	0.1	83 ± 13
CTAB	1.0	38 ± 6 *
PEG-SH	0.1	81 ± 16
PEG-SH	1.0	86 ± 13
MUA	0.1	85 ± 30
MUA	1.0	84 ± 2 *

5.4.3 Reversible Nanorod Alignment

The plasmonic properties of AuNRs become polarization dependent when they are aligned in the same direction.[19,27,50] It has been shown that with stretchable substrates, AuNRs can orient themselves to be aligned along the stretch direction.[17–21] To measure AuNR alignment in hydrogels, a setup was devised. Briefly, a polarizer was inserted between the sample and the light source. The hydrogel was then attached, either stretched or unstretched, to a 5 mm circular aperture plate. Polarized measurements were taken at 0, 45, and 90 degrees, where 0 degrees is parallel to the stretch direction and 90 degrees is perpendicular. To isolate the localized surface plasmon resonance (LSPR) signals of the AuNRs and mitigate the contributing absorbance from the hydrogel, a blank hydrogel without any AuNRs was subtracted from all spectra.

Figure 5.9A illustrates the UV-vis spectra of an unstretched hydrogel at different polarization angles. There is no polarization dependence, indicative of random orientation of the AuNRs. Figure 5.9B shows the same sample at the same polarization angles, but this hydrogel has been stretched 500% of its initial length. The UV-vis spectra in Figure 5.9B of the stretched hydrogel show the plasmon intensity change consistent with AuNR alignment. When light is polarized 0° (red), parallel to the stretch direction, the longitudinal plasmon near 746 nm remains unchanged, but the transverse plasmon intensity near 530 nm is diminished. When light is polarized 90° (blue), perpendicular to the stretch direction, the longitudinal plasmon intensity decreases significantly and the transverse plasmon increases. Figure 5.9C represents the change in intensity of the longitudinal plasmon mode in a radial plot of the maximum extinction at the plasmon for each polarization angle tested. These results indicate the AuNRs are being aligned along the stretch direction when the hydrogel is elongated.

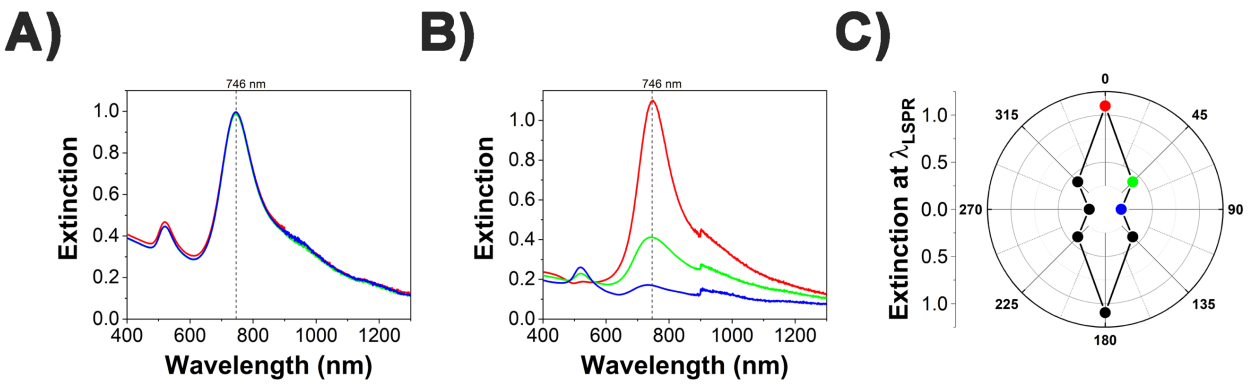

Figure 5.9: Polarized UV-vis on a Na-alginate/PAAm hydrogel with 1.0 nM CTAB AuNRs, where 0° is parallel to the stretch direction and 90° is perpendicular to the stretch direction. (A) Polarized UV-vis spectra at three different angles; 0° (red), 45° (green), and 90° (blue) for an unstretched hydrogel with AuNRs. (B) Polarized UV-vis spectra at three different angles; 0° (red), 45° (green), and 90° (blue) for a hydrogel with AuNRs stretched 500% its initial length. (C) Radial plot of the maximum absorbance at the longitudinal plasmon for each polarization angle for a stretched hydrogel with AuNRs.

The AuNR alignment was further investigated by determining how the elongation amount influenced the AuNR alignment. This was done by continually stretching a single hydrogel sample further and taking polarized UV-vis measurements at each point. We monitored the degree of alignment by measuring the ratio of the maximum extinction at the longitudinal plasmon for the parallel spectrum divided by the maximum extinction at the longitudinal plasmon for perpendicular spectrum. The larger this ratio is, the more aligned the AuNRs are along the stretch direction. As shown in Figure 5.10, once the hydrogel has been stretched roughly 400% of its initial length the extinction ratio begins to level off and the AuNRs are fully aligned along the

stretch direction. The results depicted in Figure 5.10 is a representative example of the 1.0 nM CTAB AuNR hydrogel.

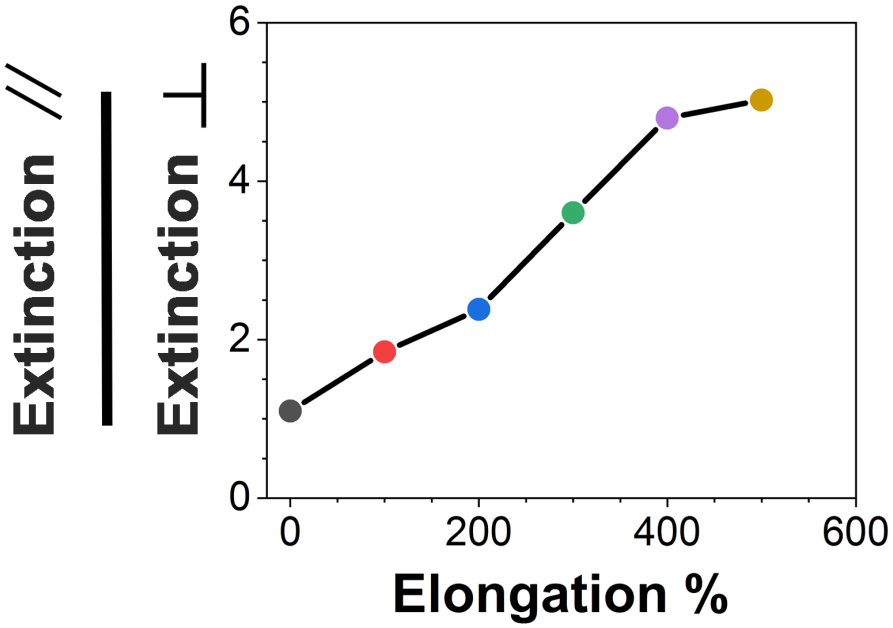

Figure 5.10: Plot of the ratio of the extinction at the longitudinal plasmon for light polarized parallel over light polarized perpendicular as measured by UV-vis versus the stretch % of a Na-alginate/PAAm hydrogel with 1.0 nM CTAB AuNRs. The AuNRs are becoming more aligned along the stretch direction as the hydrogel is stretched further indicated by the increasing ratio of the plasmon extinction. Colors represent different stretch percentages in relation to the initial length of the hydrogel (black: 0%, red: 100%, blue: 200%, green: 300%, purple: 400%, and gold: 500%).

Notably, this AuNR alignment is also reversible. When a stretched hydrogel was returned to its relaxed state, the AuNRs were no longer aligned indicated by the lack of polarization dependence. A hydrogel with AuNRs was stretched (500% its initial length) and relaxed through three cycles, with polarized UV-vis measurements collected at each position (Figure 5.11). The results shown in Figure 5.11 are representative of a single hydrogel's alignment reversibility. The slight discrepancies in the ratios of the stretched samples is mainly due to the manually stretching of the hydrogel sample. When stretched manually, the polarizer may not be exactly perpendicular to the stretch direction, which results in a spectrum where the longitudinal plasmon is not as diminished as when the polarizer is perfectly perpendicular; this leads to a lower extinction ratio. This reversible alignment was demonstrated for different AuNR concentrations and surface chemistries. This result implies that the nanorods must be near the polymer chains of the hydrogel, and not trapped in water pockets.

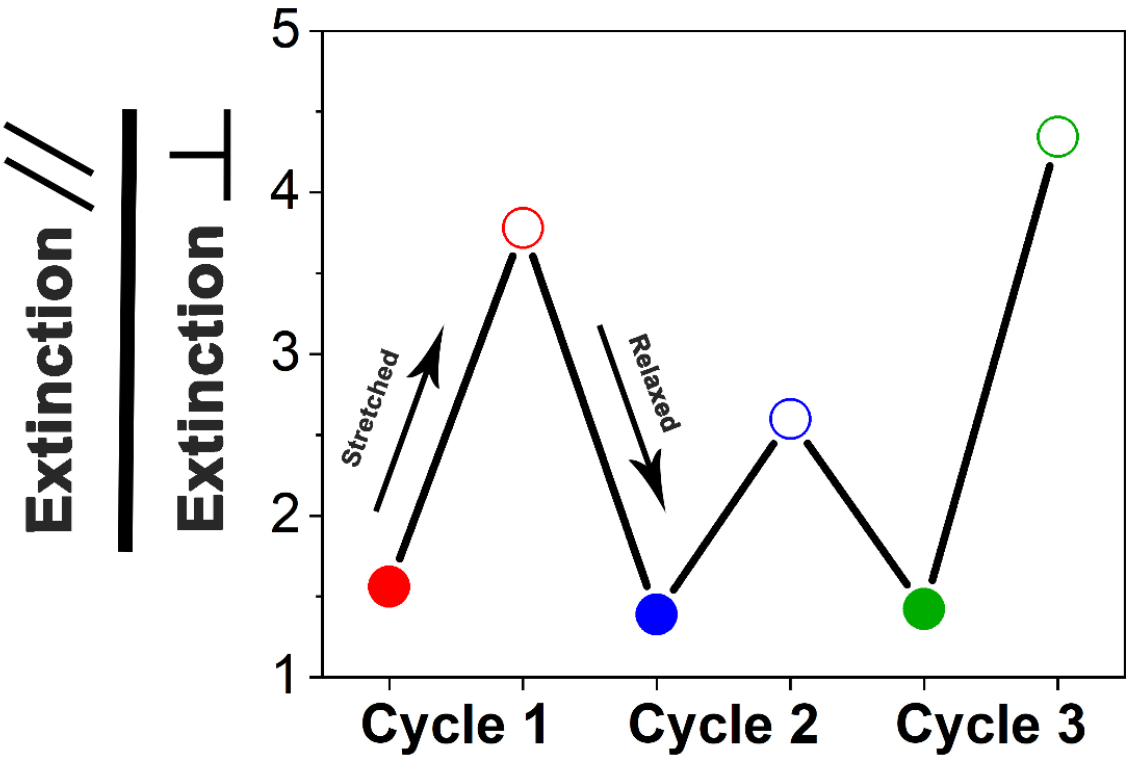

Figure 5.11: Plot of the ratio of the extinction at the longitudinal plasmon for light polarized parallel over light polarized perpendicular as measured by UV-vis versus the stretch/relax cycle of a Na-alginate/PAAm hydrogel with 0.1 nM CTAB AuNRs. The AuNRs are aligned when stretched indicated by the increasing ratio, and then the alignment is reversed when the hydrogel is relaxed. Colors represent different stretch/relax cycles, while filled circles represent the ratio the relaxed hydrogel, and open circles represent the ratio of the stretched hydrogel.

To further confirm the AuNR alignment, transmission electron micrographs were taken of both an unstretched and a stretched hydrogel sample with 2.0 nM PEG-SH AuNRs dispersed in the hydrogel. To image the hydrogel the samples were embedded in an acrylic resin, LR White. Imagining the embedded hydrogel sample with an accelerating voltage of 75 kV, visual evidence of AuNR alignment was obtained as shown by Figure 5.12B. Long range ordering of the AuNRs

orienting their longitudinal axis along the stretch direction of the hydrogel was observed. An image of an unstretched hydrogel is shown in Figure 5.12A, for an unstretched hydrogel no directional orientation of the AuNRs was observed.

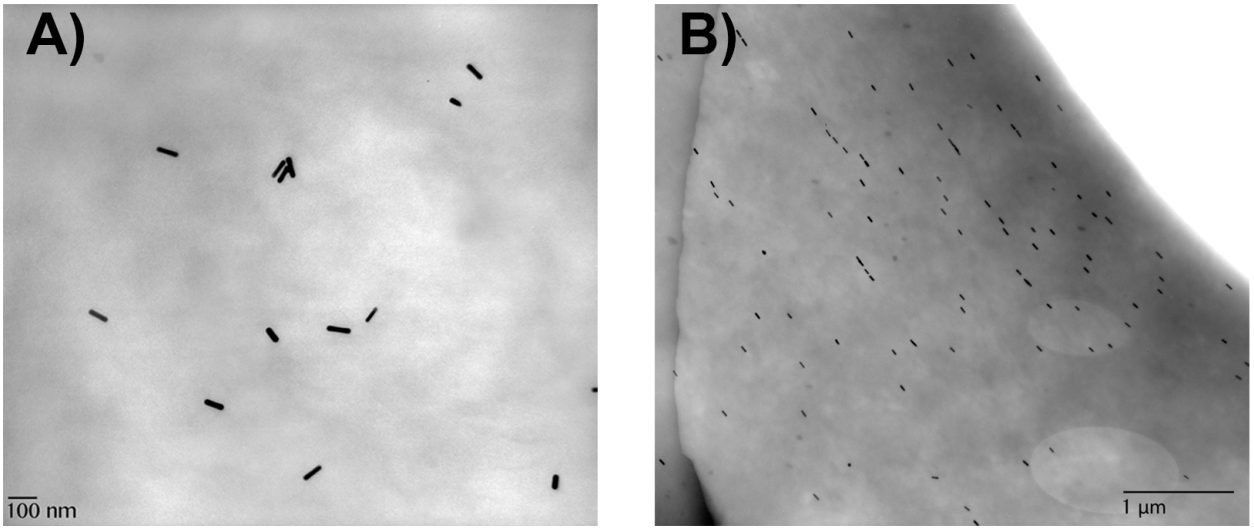

Figure 5.12: Transmission electron microscopy images of 2.0 nM PEG-SH AuNRs in Na-alginate/PAAm hydrogels. (A) Unstretched hydrogel, magnification 40,000 x (scale bar on image). (B) Stretched hydrogel, magnification 15,000 x (scale bar on image).

5.5. Conclusions

In summary, the successful alignment of gold nanorods with stretchable alginate/PAAm hydrogels was achieved. It was found that the modulus remains unchanged for Na-alginate/PAAm hydrogels for low concentration of AuNR as compared to the hydrogel without any AuNRs. However, at higher concentrations of AuNR the modulus decreases more than 25%. For Ca-alginate/PAAm, the surface chemistry also has an effect as the native hydrogel without AuNRs has a modulus of 64 ± 18 kPa and the modulus is decreased to 38 ± 6 kPa for hydrogels containing

CTAB AuNRs. This surface chemistry impact is also observed when determining the maximum elongation of the Na-alginate/PAAm hydrogels, as the hydrogels containing MUA AuNRs had an increased stretchability, more than 3,000% its initial length. Using polarized UV-vis spectroscopy and TEM, AuNR alignment was observed when the hydrogel was stretched for all AuNR concentrations and surface chemistries tested. The AuNRs became more aligned along the stretch direction as the hydrogel was stretched further, with complete alignment along the stretch direction when the hydrogel was stretched around 400% its initial length. This work shows the influence nanoscale level properties can have on bulk mechanical properties of multi-component polymer composites and demonstrates the ability to align AuNRs in a biocompatible hydrogel.

5.6 References

(1) Gong, J. P. Why Are Double Network Hydrogels so Tough? *Soft Matter* **2010**, *6* (12), 2583–2588.

(2) Vedadghavami, A.; Minooei, F.; Mohammadi, M. H.; Khetani, S.; Kolahchi, A. R.; Mashayekhan, S.; Sanati-Nezhad, A. Manufacturing of Hydrogel Biomaterials with Controlled Mechanical Properties for Tissue Engineering Applications. *Acta Biomater.* **2017**, *62*, 42–63.

(3) Chen, Q.; Chen, H.; Zhu, L.; Zheng, J. Fundamentals of Double Network Hydrogels. *J. Mater. Chem. B* **2015**, *3* (18), 3654–3676.

(4) Zhang, X.; Lin, B.; Zhao, K.; Wei, J.; Guo, J.; Cui, W.; Jiang, S.; Liu, D.; Li, J. A Free-Standing Calcium Alginate/Polyacrylamide Hydrogel Nanofiltration Membrane with High Anti-Fouling Performance: Preparation and Characterization. *Desalination* **2015**, *365* (C), 234–241.

(5) Echave, M. C.; Domingues, R. M. A.; Gómez-Florit, M.; Pedraz, J. L.; Reis, R. L.; Orive, G.; Gomes, M. E. Biphasic Hydrogels Integrating Mineralized and Anisotropic Features for Interfacial Tissue Engineering. *ACS Appl. Mater. Interfaces* **2019**, *11* (51), 47771–47784.

(6) Xie, S.; Ren, B.; Gong, G.; Zhang, D.; Chen, Y.; Xu, L.; Zhang, C.; Xu, J.; Zheng, J. Lanthanide-Doped Upconversion Nanoparticle-Cross-Linked Double-Network Hydrogels with Strong Bulk/Interfacial Toughness and Tunable Full-Color Fluorescence for Bioimaging and Biosensing. *ACS Appl. Nano Mater.* **2020**, *3*, 2274–2786.

(7) Liu, H.; Li, M.; Ouyang, C.; Lu, T. J.; Li, F.; Xu, F. Biofriendly, Stretchable, and Reusable Hydrogel Electronics as Wearable Force Sensors. *Small* **2018**, *14* (36), 1801711–1801719.

(8) Chen, J.; Peng, Q.; Thundat, T.; Zeng, H. Stretchable, Injectable, and Self-Healing Conductive Hydrogel Enabled by Multiple Hydrogen Bonding toward Wearable Electronics. *Chem. Mater.* **2019**, *31* (12), 4553–4563.

(9) Haider, H.; Yang, C. H.; Zheng, W. J.; Yang, J. H.; Wang, M. X.; Yang, S.; Zrínyi, M.; Osada, Y.; Suo, Z.; Zhang, Q.; Zhou, J.; Chen, Y. M. Exceptionally Tough and Notch-Insensitive Magnetic Hydrogels. *Soft Matter* **2015**, *11* (42), 8253–8261.

(10) Sun, J.-Y.; Zhao, X.; Illeperuma, W. R. K.; Chaudhuri, O.; Oh, K. H.; Mooney, D. J.; Vlassak, J. J.; Suo, Z. Highly Stretchable and Tough Hydrogels. *Nature* **2012**, *489* (7414), 133–136.

(11) Rong, Q.; Lei, W.; Liu, M. Conductive Hydrogels as Smart Materials for Flexible Electronic Devices. *Chem. Eur. J.* **2018**, *24* (64), 16930–16943.

(12) Talebian, S.; Mehrali, M.; Taebnia, N.; Pennisi, C. P.; Kadumudi, F. B.; Foroughi, J.; Hasany, M.; Nikkhah, M.; Akbari, M.; Orive, G.; Dolatshahi-Pirouz, A. Self-Healing Hydrogels: The Next Paradigm Shift in Tissue Engineering? *Adv. Sci.* **2019**, *6*, 1801664.

(13) Hore, M. J. A.; Composto, R. J. Functional Polymer Nanocomposites Enhanced by Nanorods. *Macromolecules* **2014**, *47*, 875–867.

(14) Koerner, H.; Kelley, J.; George, J.; Drummy, L.; Mirau, P.; Bell, N. S.; Hsu, J. W. P.; Vaia, R. A. ZnO Nanorod-Thermoplastic Polyurethane Nanocomposites: Morphology and Shape Memory Performance. *Macromolecules* **2009**, *42*, 8933–8942.

(15) Moniruzzaman, M.; Winey, K. I. Polymer Nanocomposites Containing Carbon Nanotubes. *Macromolecules* **2006**, *39*, 5194–5205.

(16) Ward, C. J.; Tonndorf, R.; Eustes, A.; Auad, M. L.; Davis, E. W. Efficacy of Gold Photothermal-Activated Shape Memory Polyurethane. *J. Nanomater.* **2020**, *2020*, 5189434.

(17) Murphy, C. J.; Orendorff, C. J. Alignment of Gold Nanorods in Polymer Composites and on Polymer Surfaces. *Adv. Mater.* **2005**, *17* (18), 2173–2177.

(18) Dai, L.; Lu, X.; Song, L.; Huang, Y.; Liu, B.; Zhang, L.; Zhang, J.; Wu, S.; Chen, T. Macroscopic-Oriented Gold Nanorods in Polyvinyl Alcohol Films for Polarization-Dependent Multicolor Displays. *Adv. Mater. Interfaces* **2018**, *5* (11), 1800026.

(19) Pérez-Juste, J.; Rodríguez-González, B.; Mulvaney, P.; Liz-Marzán, L. M. Optical Control and Patterning of Gold-Nanorod-Poly(Vinyl Alcohol) Nanocomposite Films. *Adv. Funct. Mater.* **2005**, *15* (7), 1065–1071.

(20) Zande, B. M. I. van der; Pagès, L.; Hikmet, R. A. M.; Blaaderen, A. van. Optical Properties of Aligned Rod-Shaped Gold Particles Dispersed in Poly(Vinyl Alcohol) Films. *J. Phys. Chem. B* **1999**, *103* (28), 5761–5767.

(21) Pletsch, H.; Tebbe, M.; Dulle, M.; Förster, B.; Fery, A.; Förster, S.; Greiner, A.; Agarwal, S. Reversible Gold Nanorod Alignment in Mechano-Responsive Elastomers. *Polymer* **2015**, *66* (C), 167–172.

(22) Yang, K.; Han, Q.; Chen, B.; Zheng, Y.; Zhang, K.; Li, Q.; Wang, J. Antimicrobial Hydrogels: Promising Materials for Medical Application. *Int. J. Nanomed.* **2018**, *13*, 2217–2263.

(23) Arno, M. C.; Inam, M.; Weems, A. C.; Li, Z.; Binch, A. L. A.; Platt, C. I.; Richardson, S. M.; Hoyland, J. A.; Dove, A. P.; O'Reilly, R. K. Exploiting the Role of Nanoparticle Shape in Enhancing Hydrogel Adhesive and Mechanical Properties. *Nat. Commun.* **2020**, *11*, 1420.

(24) Gaharwar, A. K.; Peppas, N. A.; Khademhosseini, A. Nanocomposite Hydrogels for Biomedical Applications. *Biotechnol. Bioeng.* **2013**, *111* (3), 441–453.

(25) Thoniyot, P.; Tan, M. J.; Karim, A. A.; Young, D. J.; Loh, X. J. Nanoparticle-Hydrogel Composites: Concept, Design, and Applications of These Promising, Multi-Functional Materials. *Adv. Sci.* **2015**, *2*, 1400010.

(26) Burrows, N. D.; Lin, W.; Hinman, J. G.; Dennison, J. M.; Vartanian, A. M.; Abadeer, N. S.; Grzincic, E. M.; Jacob, L. M.; Li, J.; Murphy, C. J. Surface Chemistry of Gold Nanorods. *Langmuir* **2016**, *32* (39), 9905–9921.

(27) Chen, H.; Shao, L.; Li, Q.; Wang, J. Gold Nanorods and Their Plasmonic Properties. *Chem. Soc. Rev.* **2013**, *42* (7), 2679–2724.

(28) Keshavarz, M.; Moloudi, K.; Paydar, R.; Abed, Z.; Beik, J.; Ghaznavi, H.; Shakeri-Zadeh, A. Alginate Hydrogel Co-Loaded with Cisplatin and Gold Nanoparticles for Computed Tomography Image-Guided Chemotherapy. *J. Biomater. Appl.* **2018**, *33* (2), 161–169.

(29) Roth, A.; Murschel, F.; Latreille, P.-L.; Martinez, V. A.; Liberelle, B.; Banquy, X.; Crescenzo, G. D. Coiled Coil Affinity-Based Systems for the Controlled Release of Biofunctionalized Gold Nanoparticles from Alginate Hydrogels. *Biomacromolecules* **2019**, *20* (5), 1926–1936.

(30) Baei, P.; Jalili-Firoozinezhad, S.; Rajabi-Zeleti, S.; Tafazzoli-Shadpour, M.; Baharvand, H.; Aghdami, N. Electrically Conductive Gold Nanoparticle-Chitosan Thermosensitive Hydrogels for Cardiac Tissue Engineering. *Mater. Sci. Eng. C* **2016**, *63*, 131–141.

(31) Shevach, M.; Fleischer, S.; Shapira, A.; Dvir, T. Gold Nanoparticle-Decellularized Matrix Hybrids for Cardiac Tissue Engineering. *Nano Lett.* **2014**, *14* (10), 5792–5796.

(32) Grzincic, E. M.; Murphy, C. J. Gold Nanorods Indirectly Promote Migration of Metastatic Human Breast Cancer Cells in Three-Dimensional Cultures. *ACS Nano* **2015**, *9* (7), 6801–6816.

(33) Zhang, C.-L.; Cao, F.-H.; Wang, J.-L.; Yu, Z.-L.; Ge, J.; Lu, Y.; Wang, Z.-H.; Yu, S.-H. Highly Stimuli-Responsive Au Nanorods/Poly(N-Isopropylacrylamide) (PNIPAM) Composite Hydrogel for Smart Switch. *ACS Appl. Mater. Interfaces* **2017**, *9* (29), 24857–24863.

(34) Sershen, S. R.; Mensing, G. A.; Ng, M.; Halas, N. J.; Beebe, D. J.; West, J. L. Independent Optical Control of Microfluidic Valves Formed from Optomechanically Responsive Nanocomposite Hydrogels. *Adv. Mater.* **2005**, *17* (11), 1366–1368.

(35) Pastoriza-Santos, I.; Kinnear, C.; Perez-Juste, J.; Mulvaney, P.; Liz-Marzan, L. Plasmonic Polymer Nanocomposites. *Nat. Rev. Mater.* **2018**, *3*, 375–391.

(36) Arafa, M. G.; El-Kased, R. F.; Elmazar, M. M. Thermoresponsive Gels Containing Gold Nanoparticles as Smart Antibacterial and Wound Healing Agents. *Sci. Rep.* **2018**, *8*, 13674.

(37) Ghisleri, C.; Siano, M.; Ravagnan, L.; Potenza, M. A. C.; Milani, P. Nanocomposite-Based Stretchable Optics. *Laser & Photonics Rev.* **2013**, *7* (6), 1020–1026.

(38) Wen, J.; Zhang, H.; Chen, H.; Zhang, W.; Chen, J. Stretchable Plasmonic Substrate with Tunable Resonances for Surface-Enhanced Raman Spectroscopy. *J. Opt.* **2015**, *17* (11), 114015.

(39) Lee, J.-E.; Park, C.; Chung, K.; Lim, J. W.; Mota, F. M.; Jeong, U.; Kim, D. H. Viable Stretchable Plasmonics Based on Unidirectional Nanoprisms. *Nanoscale* **2018**, *10* (8), 4105–4112.

(40) Alkilany, A. M.; Thompson, L. B.; Murphy, C. J. Polyelectrolyte Coating Provides a Facile Route to Suspend Gold Nanorods in Polar Organic Solvents and Hydrophobic Polymers. *ACS Appl. Mater. Interfaces* **2010**, *2* (12), 3417–3421.

(41) Yang, C. H.; Wang, M. X.; Haider, H.; Yang, J. H.; Sun, J.-Y.; Chen, Y. M.; Zhou, J.; Suo, Z. Strengthening Alginate/Polyacrylamide Hydrogels Using Various Multivalent Cations. *ACS Appl. Mater. Interfaces* **2013**, *5* (21), 10418–10422.

(42) Vigderman, L.; Zubarev, E. R. High-Yield Synthesis of Gold Nanorods with Longitudinal SPR Peak Greater than 1200 Nm Using Hydroquinone as a Reducing Agent. *Chem. Mater.* **2013**, *25* (8), 1450–1457.

(43) Hinman, J. G.; Turner, J. G.; Hofmann, D. M.; Murphy, C. J. Layer-by-Layer Synthesis of Conformal Metal–Organic Framework Shells on Gold Nanorods. *Chem. Mater.* **2018**, *30* (20), 7255–7261.

(44) Indrasekara, A. S. D. S.; Wadams, R. C.; Fabris, L. Ligand Exchange on Gold Nanorods: Going Back to the Future. *Part. Part. Syst. Character.* **2014**, *31* (8), 819–838.

(45) Hore, M. J.; Composto, R. J. Strategies for Dispersing, Assembling, and Orienting Nanorods in Polymers. *Curr. Opin. Chem. Eng.* **2013**, *2* (1), 94–101.

(46) Islam, M. S.; Masoodi, R.; Rostami, H. The Effect of Nanoparticles Percentage on Mechanical Behavior of Silica-Epoxy Nanocomposites. *J. Nanosci.* **2013**, *2013* (2), 275037.

(47) Pol, M. H.; Liaghat, G. H. Studies on the Mechanical Properties of Composites Reinforced with Nanoparticles. *Polym. Compos.* **2015**, *38* (1), 205–212.

(48) Demianenko, P.; Minisini, B. Stiff IPN Hydrogels of Poly(Acrylamide) and Alginate: Influence of the Crosslinking Ion's Valence on Hydrogel's Final Properties. *Chem. Eng. Process* **2016**, *7* (4), 1000304.

(49) Yang, J.; Han, C.; Xu, F.; Sun, R. Simple Approach to Reinforce Hydrogels with Cellulose Nanocrystals. *Nanoscale* **2014**, *6* (11), 5934–10.

(50) Jain, P. K.; El-Sayed, M. A. Plasmonic Coupling in Noble Metal Nanostructures. *Chem. Phys. Lett.* **2010**, *487* (4), 153–164.